

# **Failure mechanisms and mobilization processes of coastal landslides in sensitive soils**

**Kumulative Dissertationsarbeit**



**Max Oke Kluger**

MARUM - Center for Marine Environmental Sciences  
Universität Bremen

zur Erlangung des Grades  
*- Doctor rer. nat. -*

**Gutachter:** Prof. Dr. Tobias Mörz (Universität Bremen)  
Dr. Vicki G. Moon (University of Waikato)

**Advisors:** Dr. Stefan Kreiter (Universität Bremen)  
Dr. Willem de Lange (University of Waikato)  
Dr. Gerhard Bartzke (Universität Bremen)

**Erste Version eingereicht am:** 31. März 2017

**Überarbeitete Version eingereicht am:** 11. Oktober 2017

**Kolloquium gehalten am:** 11. August 2017

**Versicherung an Eides Statt**  
gem. §5 Abs. 5 der Promotionsordnung vom 15.07.2015

Ich, Max Oke Kluger, wohnhaft in der Langeooger Str. 31, 28219, Bremen

versichere an Eides Statt durch meine Unterschrift, dass ich die vorstehende Arbeit selbständig und ohne fremde Hilfe angefertigt und alle Stellen, die ich wörtlich dem Sinne nach aus Veröffentlichungen entnommen habe, als solche kenntlich gemacht habe, mich auch keiner anderen als der angegebenen Literatur oder sonstiger Hilfsmittel bedient habe, und die zu Prüfungszwecken beigelegte elektronische Version der Dissertation mit der abgegebenen gedruckten Version identisch ist.

Ich versichere an Eides Statt, dass ich die vorgenannten Angaben nach bestem Wissen und Gewissen gemacht habe und dass die Angaben der Wahrheit entsprechen und ich nichts verschwiegen habe.

Die Strafbarkeit einer falschen eidesstattlichen Versicherung ist mir bekannt, namentlich die Strafandrohung gemäß §156 StGB bis zu drei Jahren Freiheitsstrafe oder Geldstrafe bei vorsätzlicher Begehung der Tat bzw. gemäß §161 Abs. 1 StGB bis zu einem Jahr Freiheitsstrafe oder Geldstrafe bei fahrlässiger Begehung.

---

Bremen, 11. October, 2017



## Acknowledgements

I acknowledge the Deutsche Forschungsgemeinschaft (DFG) research center / Cluster of Excellence "The Ocean in the Earth System" via the Integrated Coastal Zone and Shelf Sea Research Training Group INTERCOAST and the MARUM Center for Marine Environmental Science at the University of Bremen for funding this Ph.D. program. The University of Waikato is thanked for providing workspace and infrastructure during my stay in New Zealand.

I want to thank my supervisors Tobias Mörz and Vicki Moon as well as my advisors Stefan Kreiter, David Lowe, Willem de Lange, and Gerhard Bartzke for never ending support during my Ph.D. project. Your guidance during experimental work and your knowledge and patience during countless discussions provided the basis for a successful completion of my thesis.

Furthermore, I want to acknowledge my co-authors Jock Churchman, Daniel Hepp, Jean-Sebastien L'Heureux, Ehsan Jorat, Stefan Kreiter, David Lowe, Philippa Mills, Vicki Moon, Tobias Mörz, Rolando Orense, David Seibel, and Sylvia Stegmann who provided invaluable contributions to the chapters of this thesis.

I thank Wolfgang Schunn, Marc Huhndorf, Mathias Lange, Daniel Otto, and Renat Radosinsky for their help and assistance in engineering issues.

I acknowledge Nicole Baeten, Stefanie Buchheister, David Culliford, Volker Diekamp, Tobias Goetz, Anne Hübner, Ehsan Jorat, Nele Lamping, Willem de Lange, Tyler Manderson, Christopher Morcom, Jonno Rau, Alexander Rösner, Robert Roskoden, Christiane Schott, Connor Schulze, David Seibel, Bastian Steinborn, Benjamin Steward, Christoph Vogt, and Petra Witte for help during field and/or laboratory work.

I am grateful to Knut Andersen, Daniel Hepp, Matt Ikari, Lotta Kluger, Joseph Lane, Pooria Pasbakhsh, Florian Sense, and Torsten Wichtmann for helpful discussions on the papers. I thank Fernanda Cravero, Sebastien Garziglia, Tom Lunne, Mauri McSaveney, Fabio Terrible, Kenneth Torrance, and an anonymous reviewer for helpful reviews. I acknowledge Matt Ikari and Stefan Kreiter who gave comments on the introduction of this thesis.

Last but not least, I would like to thank my family and friends for supporting me during this Ph.D. project.



## Abstract

Landslides are globally widespread along coasts, posing a major natural threat to population and infrastructure. Understanding initiation, type, and areas affected by such landslides, is thus one of the primary concerns for coastal communities and infrastructure projects, like harbor constructions and residential settlements. Some of the most damaging landslides in the past occurred in soil with high sensitivity, a measure of the post-failure strength loss in the failure zone during landsliding. Such soil exhibits very low shear strength after failure, predisposing progressive landslides with long runout distance and dimensions difficult to predict. High sensitivities have been described in post-glacial clayey sediments in Norway, as well as in weathered tephra in New Zealand. In both regions, it is of common interest to better understand the effect of cyclic loading, such as earthquake shaking or machine vibrations, on the shear strength of post-glacial clayey sediments and weathered tephra, respectively. Furthermore, the processes that lead to high sensitivities in weathered tephra are still poorly understood.

This doctoral thesis aims to broaden the understanding of pre- and post-failure mechanisms of coastal landslides in sensitive soil. Two landslides were investigated, that occurred in sensitive soil and affected society, economy, and natural environment in coastal regions: (1) The coastal submarine Orkdalsfjord landslide in post-glacial silt, Norway, and (2) the coastal subaerial Omokoroa flow slide in weathered tephra, New Zealand.

The vulnerability of the Orkdalsfjord landslide to cyclic loading was studied by in situ vibratory cone penetration tests and laboratory cyclic triaxial testing. Very coarse silt layers, interbedded in the post-glacial silt unit overlying the failure surface, are more vulnerable to cyclic loading compared to surrounding finer silts. Accordingly, the very coarse silt layers may have contributed to the weakening of the Orkdalsfjord landslide in the presence of cyclic loading. The cyclic loading behavior of weathered tephra from the Omokoroa flow slide was analyzed by monotonic and cyclic triaxial testing. The weathered tephra experiences brittle failure and has higher friction coefficients than normally consolidated clay, being similar to granular soil. Comparing the cyclic shear strength of weathered tephra with that of sensitive post-glacial clays shows that for weathered tephra the number of loading cycles to shear

failure depends more strongly on the level of shear stress applied and that altered tephra is more resistant to small cyclic loading but fails within a narrower range of shear stresses.

The development of high sensitivities in weathered tephra was analyzed by scanning electron microscopy and laboratory vane shear measurements along a drill core comprising the intact tephra succession of the Omokoroa flow slide. The secondary clay mineral halloysite dominates the Pahoia Tephra, a sequence that was involved in the Omokoroa flow slide. The halloysite particle morphologies are highly variable with depth. While tubular morphologies are prevalent in the upper tephra successions, the lower Pahoia Tephra sequence is dominated by spheroidal halloysite. This change in halloysite morphology coincides with an increase in sensitivity with depth. Therefore, spheroidal halloysite is likely the key in the development of sensitivity in weathered tephra from New Zealand and potentially elsewhere in regions of similar volcanic origin. In the failure surface of the Omokoroa flow slide, a new open-sided spheroidal halloysite particle shape in the form of 'mushroom caps' is recognized for the first time that governs the development of high mobility in the failure surface during landsliding. Based on a new 'attraction-detachment' model, it is suggested that the rearrangement in the halloysite texture during the failure process reduces the attractions between the particles at nanoscale dimensions and thus predisposes flow sliding.

Various aspects of the cyclic loading behavior of sensitive post-glacial silts and weathered tephra were studied, contributing to a better understanding of pre-failure and shear failure behavior during cyclic loading scenarios such as earthquakes. Both soil types are vulnerable to cyclic loading, which therefore needs to be considered when planning civil engineering projects on or close to slopes comprised of post-glacial silt or altered tephra. A new conceptual model explains the high sensitivities in halloysite-rich tephra, which provides a potential key for the identification of sensitive weathered tephra that are predisposed to flow sliding.

## Zusammenfassung

Hangrutschungen in Küstenregionen sind weltweit verbreitet und Studien, die zum Verständnis der Initiierung, Ausmaße und Gefährdung von Rutschungen beitragen sind von großer Bedeutung für küstennahe Wohngebiete und Infrastrukturprojekte. Einige der verheerendsten Hangrutschungen in der Vergangenheit ereigneten sich in Böden mit hoher Sensitivität, ein Parameter, der in der Geotechnik für die Quantifizierung des Scherfestigkeitsverlusts in der Versagensfläche Verwendung findet. Solch hoch sensitive Böden weisen meist eine sehr geringe Restscherfestigkeit nach dem Versagen auf, was schwer vorhersagbare, verflüssigte Hangrutschungen mit großen Auslaufbereichen begünstigt. Hohe Sensitivitäten wurden sowohl für postglaziale tonige Sedimente aus Norwegen als auch für verwitterte Tephra aus Neuseeland beschrieben. In beiden Regionen ist es von gesellschaftlichem Interesse, die Schwächung von sensitiven Hangsedimenten unter zyklischer Belastung, wie zum Beispiel während Erdbeben oder Maschinenvibrationen, besser zu verstehen. Darüber hinaus sind die Prozesse, die zu hoher Sensitivität in verwitterter Tephra führen, weitgehend unbekannt.

Diese Doktorarbeit hat das Ziel, die Pre- und Post-Versagensmechanismen von Hangrutschungen in sensitiven Böden am Übergangsbereich zwischen Land und Wasser besser zu verstehen. Dafür wurden zwei Rutschungen untersucht, die in sensitiven Böden auftraten und dabei sowohl die sozioökonomische als auch die natürliche Umwelt beeinflussten: (1) Die submarine Orkdalsfjord Hangrutschung in postglazialen Silten, Norwegen und (2) die subaerische Omokoroa Hangrutschung in verwitterter Tephra, Neuseeland.

Die Anfälligkeit der Orkdalsfjord Hangrutschung gegenüber zyklischer Belastung wurde mittels vibrierter Drucksondierung und zyklischen Triaxialversuchen untersucht. Die postglaziale Siltabfolge, die die Versagensfläche überlagert, beinhaltet zwischengelagerte Grobsiltlagen, welche anfälliger gegenüber zyklischer Belastung sind. Folglich könnten die Grobsiltlagen zu einer Schwächung der Orkdalsfjord Hangrutschung beigetragen haben, wenn während der Rutschung zyklische Belastungen vorherrschten. Das zyklische Belastungsverhalten von verwitterter Tephra aus der Omokoroa Hangrutschung wurde mit Hilfe von monotonen und zyklischen Triaxialversuchen untersucht. Die verwitterte Tephra hat ein sprödes Versagensverhalten mit höherem kritischen Reibungswinkel als postglaziale Tone und ist eher vergleichbar mit granularen Böden. Der Vergleich der zyklischen Scherfestigkeit

von verwitterter Tephra mit postglazialen Tonen zeigt, dass im Falle der verwitterten Tephra die Anzahl an Belastungszyklen bis zum Versagen stärker von der mittleren Scherspannung im Boden abhängt, und sie gegenüber kleinen Belastungszyklen beständiger ist, jedoch innerhalb eines kleineren Scherspannungsintervalls versagt.

Die Entstehung der hohen Sensitivität in verwitterter Tephra wurde anhand von Rasterelektronenmikroskopie und Laborscherflügelversuchen entlang eines Bohrkerns untersucht, welcher die vollständige ungestörte Tephraabfolge der Omokoroa Hangrutschung beinhaltet. Das sekundäre Tonmineral Halloysit dominiert die Pahoia Tephra, eine Abfolge von verwitterter Tephra, die an der Omokoroa Hangrutschung beteiligt war. Die Morphologie der Halloysitpartikel variiert mit der Tiefe: Während in den oberen Tephraabfolgen eine röhrenförmige Morphologie vorherrscht, wird die untere Pahoia Tephra von spheroidalem Halloysit dominiert. Dieser Wechsel in der Tonmorphologie geht mit einem Anstieg der Sensitivität mit der Tiefe einher. Deshalb ist spheroidaler Halloysit wahrscheinlich maßgeblich an der Entstehung hoher Sensitivität in verwitterter Tephra beteiligt. Die Versagensfläche der Omokoroa Hangrutschung wird von einer zuvor unbekanntem spheroidalem Halloysitmorphologie dominiert, die mit ihrer markanten offenen Seite an „Pilzköpfe“ erinnert. Anhand eines neuen „Anziehungs-Abstoßungs“-Modells wird postuliert, dass die Umlagerung der Halloysitmatrix während des Versagens die auf nanoskopischen Größenordnungen wirkenden Anziehungskräfte zwischen den Pilzköpfen reduziert, was zu einer starken Verflüssigung der Hangrutschung führt.

In dieser Arbeit wurden unterschiedliche Aspekte von zyklischem Belastungsverhalten sensitiver postglazialer Silte und verwitterter Tephra analysiert, was zu einem verbesserten Verständnis der Pre- und Post-Versagensmechanismen von Hangrutschungen beiträgt. Da beide Bodentypen anfällig gegenüber zyklischer Belastung sind, ist es notwendig, dies in zukünftigen Baugrundvorhaben zu berücksichtigen. Ein neues konzeptionelles Modell erklärt die hohe Sensitivität verwitterter halloysitreicher Tephra und kann zukünftig dazu verwendet werden, Regionen mit hohem Potenzial für mobile Hangrutschungen zu identifizieren.

# Table of contents

<b>List of figures</b>	<b>xv</b>
<b>List of tables</b>	<b>xxi</b>
<b>Nomenclature</b>	<b>xxiii</b>
<b>1 Introduction</b>	<b>1</b>
1.1 Landslides . . . . .	1
1.2 Role of sensitivity in landsliding . . . . .	3
1.3 Cyclic shear strength of soil . . . . .	5
1.4 Development of sensitive soil . . . . .	8
1.4.1 Post-glacial clay . . . . .	8
1.4.2 Weathered tephra . . . . .	9
1.5 Motivation and research hypotheses . . . . .	12
1.6 Study areas . . . . .	12
1.6.1 Submarine Orkdalsfjord landslide, Norway . . . . .	13
1.6.2 Subaerial Omokoroa flow slide, New Zealand . . . . .	16
1.7 Organization of this thesis and contribution to scientific journals . . . . .	17
<b>2 Methods</b>	<b>19</b>
2.1 Field methods . . . . .	19
2.1.1 Bathymetry and topography . . . . .	19
2.1.2 Static and vibratory cone penetration testing . . . . .	19
2.1.3 Coring and sampling . . . . .	20
2.1.4 Bore hole logging . . . . .	20
2.2 Laboratory methods . . . . .	21
2.2.1 Physical properties . . . . .	21
2.2.2 Mineralogy . . . . .	21
2.2.3 Shear strength . . . . .	21

<b>3</b>	<b>In situ cyclic softening of marine silts</b>	<b>23</b>
3.1	Introduction . . . . .	24
3.2	Geological setting . . . . .	25
3.3	Materials and Methods . . . . .	25
3.3.1	CPTU . . . . .	26
3.3.2	Triaxial Laboratory Testing . . . . .	26
3.4	Results . . . . .	27
3.4.1	Geotechnical Characterization of Silt Layers . . . . .	27
3.4.2	Cyclic Triaxial Response of Silt Layers . . . . .	29
3.5	Discussion and Conclusion . . . . .	29
<b>4</b>	<b>Undrained cyclic shear behaviour of altered tephra</b>	<b>33</b>
4.1	Introduction . . . . .	34
4.2	Sample material and testing procedure . . . . .	35
4.2.1	Pahoia Tephra . . . . .	35
4.2.2	Triaxial testing . . . . .	37
4.3	Static undrained shear strength of altered tephra . . . . .	40
4.4	Cyclic undrained shear behaviour of altered tephra . . . . .	42
4.5	Cyclic shear strength of altered tephra . . . . .	45
4.6	Conclusions . . . . .	49
<b>5</b>	<b>A new attraction-detachment model for explaining flow sliding in clay-rich tephtras</b>	<b>51</b>
5.1	Introduction . . . . .	52
5.2	Geological setting . . . . .	54
5.3	Methods . . . . .	54
5.4	Highly sensitive slide-prone layer dominated by spheroidal halloysite . . . . .	55
5.5	New Halloysite morphology . . . . .	57
5.6	Attraction-detachment model for flow sliding in altered tephtras . . . . .	57
5.7	Conclusions . . . . .	59
<b>6</b>	<b>Conclusions</b>	<b>61</b>
	<b>References</b>	<b>65</b>
	<b>Appendix A Conferences</b>	<b>79</b>

---

<b>Appendix B Abstracts</b>	<b>81</b>
B.1 A new attraction-disseverance model for explaining landsliding in clay-rich tephras . . . . .	81
B.2 A new attraction-detachment model for explaining landsliding in clay-rich Quaternary tephras, eastern North Island, New Zealand	82
B.3 Tale of the unexpected: How halloysite predisposes flow sliding . . . . .	83
<b>Appendix C Manuscript</b>	<b>85</b>
C.1 Introduction . . . . .	86
C.2 Hypoplasticity . . . . .	89
C.3 Materials & Methods . . . . .	91
C.3.1 Cuxhaven-Sand . . . . .	91
C.3.2 Oedometric compression test . . . . .	92
C.3.3 Triaxial compression test . . . . .	94
C.4 Hypoplastic constants . . . . .	94
C.5 Results . . . . .	98
C.5.1 Quality of sample reconstitution . . . . .	98
C.5.2 Simulations of element tests . . . . .	99
C.5.3 Sensitivity analysis of triaxial element tests . . . . .	100
C.6 Discussion . . . . .	102
C.6.1 Influence of sample reconstitution on hypoplastic soil behavior . . .	102
C.6.2 Hypoplastic model prediction for North Sea sand . . . . .	103
C.7 Conclusions . . . . .	106



# List of figures

1.1	Failure stages of landslides. $s_u$ - Undrained shear strength; $s_r$ - Remolded shear strength; $F$ - Factor of safety. . . . .	2
1.2	Progressive failure along a circular failure surface. $s_u$ - Undrained shear strength; $s_r$ - Remolded shear strength (after Locat et al., 2011). . . . .	4
1.3	Global distribution of sensitive post-glacial clays and sensitive weathered tephra. See text for references. . . . .	5
1.4	Measurement of the in situ liquefaction potential by static and vibratory cone penetration testing. <b>A:</b> Schematic cone, commonly used for cone penetration testing (after Lunne et al., 1997). <b>B:</b> Comparison of static cone resistance $q_{cs}$ with vibratory cone resistance $q_{cv}$ in order to identify sediment layers with low cyclic resistance. <b>C:</b> Sediment layers with low cyclic resistance exhibit a peak in the cone reduction diagram (A and B after Sasaki et al., 1984). . . . .	6
1.5	<b>A:</b> Monotonic and cyclic torsional shear tests on Fontainebleau sand (after Georgiannou et al., 2008). $SSL$ - Stead state line; $FLS$ - Flow liquefaction surface; $p' = (\sigma'_a + 2\sigma'_r)/3$ , with $\sigma'_a$ and $\sigma'_r$ being the axial and radial effective stresses. <b>B:</b> Monotonic and cyclic triaxial shear tests on Cloverdale clay (after Zergoun and Vaid, 1994). $q = \sigma'_a - \sigma'_r$ ; $s' = (\sigma'_a + \sigma'_r)/2$ ; $p'_c = (\sigma'_{ac} + 2\sigma'_{rc})/3$ , with $\sigma'_{ac}$ and $\sigma'_{rc}$ being the axial and radial effective consolidation stresses. . . . .	7
1.6	Cyclic deviator stress ratios - number of cycles to failure relationship for different sands, sand with fines content, coal ash, unaltered tephra (pumice), and clay (after Yoshimoto et al., 2013; Orense and Pender, 2015). $\sigma_{cy}$ - Single axial stress amplitude; $\sigma'_c$ - Effective isotropic consolidation stress. . . . .	8
1.7	Schematic view of the two case studies investigated in this doctoral thesis. Note that vertical dimensions are not to scale. <b>A:</b> Submarine Orkdalsfjord landslide in post-glacial sensitive silts, Norways. <b>B:</b> Subaerial Omokoroa flow slide in altered sensitive tephra deposits, New Zealand. . . . .	13

1.8	Swath bathymetry over the Orkdalsfjord landslide, Norway (after L’Heureux et al., 2014b). The white X marks the location of the initial failure. Data courtesy of NGU. UTM coordinates in m. . . . .	14
1.9	Distribution of earthquakes with a moment magnitude larger than 4 that occurred in the Bay of Plenty region between 1838 and 2016. The blue star marks the position of the Omokoroa flow slide. Earthquake data: <a href="http://www.geonet.org.nz">www.geonet.org.nz</a> . . . . .	15
3.1	Orkdalsfjord study area (Bathymetry from L’Heureux et al. (2014b) used with courtesy from the Geological survey of Norway, NGU). . . . .	25
3.2	Cyclic signal of VCPTU using GOST. . . . .	27
3.3	Sediment properties and in situ CPTU at study site GeoB18623. Lithology includes core photos and qualitative grain size description. <i>C</i> : Clay, <i>sC</i> : Clayey silt, <i>S</i> : Silt, <i>vf</i> : very fine sand, <i>f</i> : fine sand, <i>m</i> : medium sand. <i>I</i> <sub>1</sub> – <i>I</i> <sub>3</sub> : samples for cyclic triaxial tests, Blue: (Very) coarse silt intervals, Pink: medium-coarse silt interval. . . . .	28
3.4	Grain size distribution of samples <i>I</i> <sub>1</sub> , <i>I</i> <sub>2</sub> and <i>I</i> <sub>3</sub> tested in DTTD. . . . .	28
3.5	Undrained cyclic triaxial tests on samples <i>I</i> <sub>1</sub> and <i>I</i> <sub>2</sub> with limits for cyclic softening after Kramer (1996) and Boulanger and Idriss (2006). Test conditions: $\sigma'_c = 100 \text{ kPa}$ , $CSR = 0.1$ , $0.98 \leq B \leq 0.99$ . . . . .	30
4.1	(a-b) Sediment description and cumulative clay mineral content of core Omok-1 (Kluger et al., 2017); (c-d) Results from bore hole logging of Omok-1; (e) Grain size distribution of Pahoia Tephra, sampling depth 19 m. . . . .	36
4.2	Definition of shear stress, shear strain, and shear modulus (Modified from Andersen, 2009). . . . .	40
4.3	(a) Shear stress – shear strain and (b) shear stress – mean effective stress relationships for the Pahoia Tephra, compiled from monotonic undrained compression and extension tests from the present study and from Mills and Moon (2016). . . . .	41
4.4	Shear strain response of Pahoia Tephra to undrained loading cycles. Average and cyclic shear strain components are represented by lines and grey shaded areas, respectively. . . . .	43
4.5	Shear stress – shear strain relationship for the Pahoia Tephra under different average shear stress. . . . .	43
4.6	Cyclic shear stress ratios to reach failure in a specific number of loading cycles for different average shear stress ratios. . . . .	45

4.7	(a) Cyclic shear stress contours for different number of cycles to failure (calculated using Eq. 1 and Fig. 6) as a function of average shear stress. (b) Maximal cyclic shear strength as a function of average shear stress. (c – d) Cyclic shear stress contours compared to Norwegian clays with different plasticity indices and sensitivity. I – Wichtmann et al. (2013), II – Lunne et al. (2003), III – Andersen (2009), IV – Lunne and Lacasse (1999). . . . .	46
4.8	Progressive and abrupt shear strain development during the last loading cycles of test CY-9 and CY-22, respectively. . . . .	47
5.1	A: Map of Tauranga Harbour, New Zealand, with Taupo Volcanic Zone (TVZ) as main source for Quaternary tephras at study site. B: Three-dimensional view of the flow slide at Omokoroa; red line marks position of profile in C. I.—Ignimbrite. C: Profile through flow slide with simplified stratigraphy and associated paleosols (P1–P4) of drill core Omok-1 and ages (in Ma) after Moon et al. (2015b). . . . .	53
5.2	A: Stratigraphy of drill core Omok-1 after Moon et al. (2015b) showing main lithological units as defined in Figure 5.1, three paleosols (P1-P3), and highly sensitive white layer at 23 m depth (hatched area). I.-Ignimbrite; T.-Tephras. B: Undisturbed ( $s_u$ , blue) and remolded ( $s_r$ , orange) shear strength, and sensitivity ( $S = s_u/s_r$ ). C: Halloysite bulk concentration. D: Cumulative volume percent (c. vol %) of halloysite morphologies with bars indicating average standard deviations. E: Average spheroid sizes with standard deviations depicted by fill patterns. F: Three-dimensional line plot illustrating relationship between spheroid content, sensitivity, spheroid size, and halloysite concentration; gray graded areas enable trends in sensitivity to be visualized. G: Dependency between sensitivity and shear strength. . . . .	56

5.3	A–D: Scanning electron microscopy (SEM) images of spheroids (A), polyhedrons (B), tubes (C), and plates (D) representing the main halloysite morphologies in Pahoia Tephra sequence (New Zealand). E–H: SEM images from the highly sensitive layer of undisturbed and multiply-connected halloysite spheroids (E,F) and remolded spheroids (G,H) showing smaller clusters or detached spheroids within much looser particle network. 1-exposed layers in spheroid openings; 2-partially separated halloysite spheroids; 3-detached mushroom cap-shaped halloysite spheroid. I: Electrostatic field proximal to halloysite nanotubes with colored equipotential surfaces (ES), modified with permission from Guimarães et al. (2010), copyright 2010 American Chemical Society. J: Conceptual mushroom cap-shaped spheroid cross-section and weak electrostatic and/or van der Waals attractions arising between exposed silanol-aluminol sheets in spheroid openings and negatively charged convex exterior surfaces; enlargement is adapted from Berthonneau et al. (2015). Circles with + and – relate to positive and negative electrostatic field proximal to spheroid’s exterior surface. K,L: Mushroom cap-shaped spheroids connect with one another between concave openings and convex outer spheroid surfaces, forming aggregates (K) which are partly detached because of remolding (L). . . . .	58
C.1	a) General stress-strain relationship of granular materials. b) Schematic deviator stress and c) Volumetric strain curves for dense granular materials. . . . .	87
C.2	Sketch of hypoplastic parameter determination. . . . .	89
C.3	a) Typical sedimentary structures in the sand pit Altenwalde (May, 2013). <i>I</i> – subparallel layering, <i>II</i> – cross-bedding, <i>IIIa</i> – clay layer, <i>IIIb</i> – erosive channel with graded sand bedding. b) Tentative stratigraphy and high resolution CPTU profile of the sand pit Altenwalde. References: <i>1</i> – Mörz (2015, internal report), <i>2</i> – after Ehlers et al. (2004). . . . .	91
C.4	Grain size distribution of Cuxhaven-Sand. . . . .	92
C.5	Schematic diagrams of: a) oedometer and b) triaxial devices. . . . .	93
C.6	Schematic illustration of the applied sample reconstitutions. a) Dry pluviation, b) Moist tamping and c) Lateral tapping. . . . .	93
C.7	a) Peak shear stresses in the $p - q$ -plane for samples with different initial void ratios. b) Peak friction angle as a function of the void ratio at peak state. The error bars indicate the standard deviation of each individual series of measurements. . . . .	96
C.8	Oedometer compression curves with different initial void ratios. Laboratory and simulation results are denoted by symbols and thick lines, respectively. The range between critical and densest void ratios is shaded in gray. . . . .	96

---

C.9	Comparison between data and modeled curves in triaxial compression tests for: a) deviator stress and b) volumetric strain. c) Photographs taken during triaxial shearing at 0, -10 and -20 % axial strain. . . . .	97
C.10	Initial void ratios of dry pluviated triaxial samples with shutters containing grid openings of 3 or 4 mm. . . . .	99
C.11	Influence of hypoplastic parameter variation on modeled deviatoric stress and volumetric strain of initial dense triaxial tests ( $e_0 = 0.52$ , $T_3 = -200 \text{ kPa}$ ). Lines denote simulations with original $e_0$ and dashed lines indicate a single parameter variation of $\pm 20\%$ . a) Variation of expression exponent $n$ b) Variation of limit void ratio $e_{d0}$ at stress free state c) Variation of exponent $\alpha$ . 100	100
C.12	Multiparameter analysis of triaxial element tests for deviatoric stress and volumetric strain curves ( $e_0 = 0.52$ , $T_3 = -200 \text{ kPa}$ ). The effect of varying $n$ , $e_{d0}$ and $a$ by 20 % on a) initial tangent modulus $E_i$ b) peak strength $q_{Peak}$ c) range of contraction $\epsilon_c$ c) angle of dilatancy at peak state $v_{Peak}$ . . . . .	101
C.13	Comparison of peak and critical deviator stress ratio for different reconstitution methods and initial relative density. Relative density ranges after DIN EN ISO 14688-2:2004 (2004). . . . .	103
C.14	Comparison between model simulations and laboratory data for triaxial compression tests in different sands for a) Peak shear strength b) Peak angle of dilatancy c) Initial tangent modulus d) Range of contraction. . . . .	104



# List of tables

1.1	General model of sensitivity development in post-glacial clays and weathered tephra (after Torrance, 1983, 1992). . . . .	10
4.1	Physical and mechanical properties of the Pahoia Tephra. . . . .	36
4.2	Specifications of monotonic triaxial tests. . . . .	39
4.3	Specifications of cyclic triaxial tests. . . . .	39
C.1	Grain size moments of the Cuxhaven-Sand. . . . .	92
C.2	Comparison between different proctor test procedures. . . . .	93
C.3	Comparison of $\alpha$ regarding different sample preparation methods. <i>SD</i> - Standard deviation. In <i>bold</i> - picked hypoplastic constant. . . . .	98
C.4	Hypoplastic constants for the Cuxhaven-Sand. . . . .	98
C.5	Initial void ratios $e_0$ for different reconstituting techniques. <i>SD</i> - Standard deviation. . . . .	98
C.6	Sensitivity of hypoplastic parameter variations on deviatoric stress and volumetric strain. Influence: - <i>neglectable</i> , + <i>noticeable</i> , ++ <i>considerable</i> . . .	99



# Nomenclature

## Roman Symbols

$F$	Factor of safety
$s$	Shear strength
$a$	Regression parameter of Eq. 4.1
$b$	Regression parameter of Eq. 4.1
$B$	Skempton's B-value
$c'$	Effective cohesion
$CSR$	Cyclic stress ratio
$d_{50}$	Median grain size
$e_0$	Initial void ratio before consolidation
$\Delta e$	Difference in void ratios measured before and after consolidation
$f$	Frequency
$I_p$	Plasticity index
$K_0$	Earth pressure coefficient at rest
$N$	Number of loading cycles
$N_f$	Number of loading cycles required to reach failure
$p'$	Mean effective stress, $p' = (\sigma'_a + 2\sigma'_r)/3$
$p'_c$	Mean effective consolidation stress, $p'_c = (\sigma'_{ac} + 2\sigma'_{rc})/3$

---

$q_{cs}$	Static cone resistance
$q_{cv}$	Vibratory cone resistance
$RR$	Reduction ratio
$\dot{s}$	Shear rate
$S$	Sensitivity, $S = s_u/s_r$
$s'$	Mean effective stress, $s' = (\sigma'_a + \sigma'_r)/2$
$s_r$	Remolded shear strength
$s_u$	Undrained or undisturbed shear strength
$s_u$	Undrained shear strength
$s_u^C$	Undrained shear strength obtained from monotonic compression tests
$s_u^E$	Undrained shear strength obtained from monotonic extension tests
$s_u^E/s_u^C$	Anisotropy ratio
$u$	Pore water pressure
$u_2$	Pore pressure measured during cone penetration testing at cone position 2
$\Delta u$	Saturation pressure
$u_n$	Normalized pore water pressure
$w$	Natural water content
$w_L$	Liquid limit
$w_P$	Plastic limit

### Greek Symbols

$\dot{\epsilon}_a$	Axial strain rate
$\epsilon_1$	Axial strain
$\epsilon_a$	Axial strain
$\epsilon_r$	Radial strain

---

$\gamma$	Shear strain
$\gamma_i$	Initial shear strain in case undrained shear stress is applied before cyclic loading
$\gamma_{av}$	Average shear strain
$\gamma_{cy}$	Cyclic shear strain
$\phi'_{crit}$	Critical friction angle
$\sigma_{cy}$	Cyclic axial stress
$\sigma_{cy}$	Cyclic axial stress
$\sigma'_c$	Effective isotropic consolidation stress
$\sigma'_r$	Effective radial stress
$\sigma'_{ac}$	Effective axial consolidation stress; effective overburden pressure
$\sigma_a$	Total axial stress
$\tau$	Shear stress
$\tau_c$	Consolidation shear stress
$\tau_{av}$	Average shear stress
$\tau_{av}/s_u^C$	Average shear stress ratio
$\tau_{cy}$	Cyclic shear stress
$\tau_{cy}/s_u^C$	Cyclic shear stress ratio
$\tau_{f,cy}$	Maximal cyclic shear strength
$\tau_{max}$	Maximal shear stress
$\phi'$	Effective stress angle of internal friction
$\sigma'$	Effective stress
$\sigma_n$	Total normal stress
$\sigma'_{rc}$	Effective radial consolidation stress

### Acronyms / Abbreviations

CPTU Cone penetration testing with pore pressure measurement

DTTD Dynamic Triaxial Testing Device

GOST Geotechnical Offshore Seabed Tool

VCPTU Vibratory cone penetration testing with pore pressure measurement

SCPTU Static cone penetration test

# Chapter 1

## Introduction

### 1.1 Landslides

Landslides are “downward and outward movements of slope-forming materials, wherein shear failure occurs along one or several surfaces” (Eckel, 1958; Hampton et al., 1996). They are globally widespread in all types of environments, posing a major natural hazard to population and infrastructure. Areas close to the shoreline have always been the preferential location for settlements, because of the easy accessibility, trade and the wealth of natural resources. With the rapidly growing global population during the last few decades, this results in around 1.2 billion people living within 100 km from the shoreline (Small and Nicholls, 2003). As a consequence, a large percentage of coastal communities are exposed to landslides. Notable examples of coastal landslides in Finneidfjord, Norway, and in Nice, France have caused fatalities as well as partial destructions of harbor constructions (Assier-Rzadkiewicz et al., 2000; Longva et al., 2003), highlighting the need to better understand the causes of landslides in coastal areas.

The causes of landslides are often complex and arise from a combination of geologic, topographic, and climatic factors (Varnes, 1978). However, they are always the result of slope failure, which is initiated when the factor of safety  $F$

$$F = s/\tau, \tag{1.1}$$

drops below 1 (Morgenstern and Price, 1965). Where  $\tau$  is the shear stress acting in the slope. The shear strength  $s$  is defined as the maximum shear stress  $\tau_{max}$  that the soil can withstand and is controlled by effective stress. The relationship between shear strength and effective stress can be represented by the Mohr-Coulomb strength envelope as

$$s = \tau_{max} = c' + \sigma' \tan \phi', \quad (1.2)$$

where  $c'$  is the effective stress cohesion,  $\sigma'$  is the effective stress on the failure plane at failure, and  $\phi'$  is the effective stress angle of internal friction (Muir Wood, 1990; Duncan et al., 2014). For undrained loading conditions, excess pore water pressure  $u$  decreases the normal stress  $\sigma_n$  according to Terzaghi's effective stress principle (Terzaghi, 1944):

$$\sigma' = \sigma_n - u, \quad (1.3)$$

which leads to a decrease in effective stress. As a consequence, the undrained shear strength  $s_u$  is lower than the shear strength of the soil for drained loading conditions.

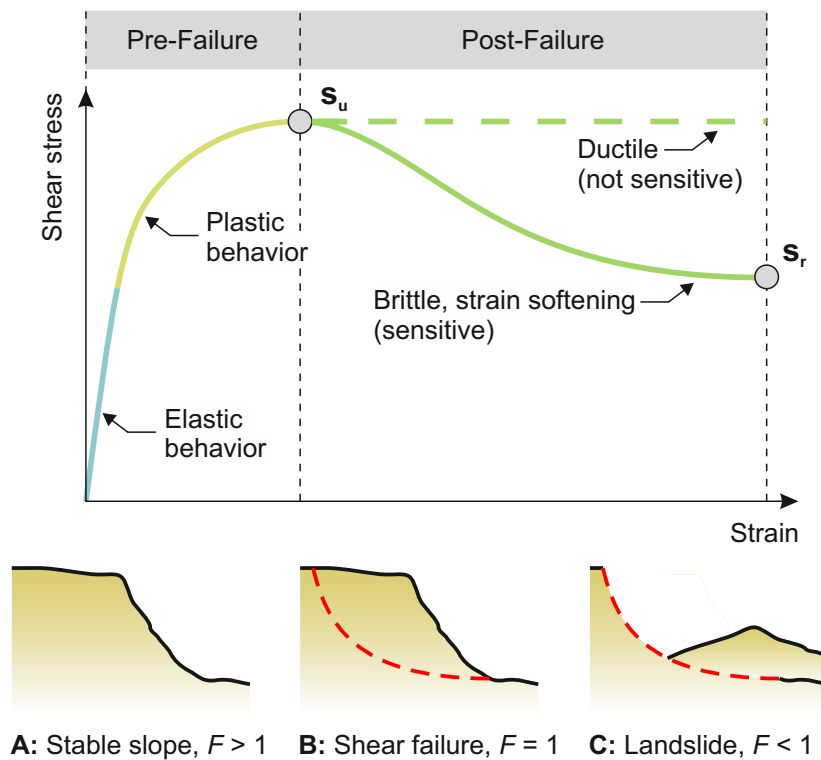


Fig. 1.1 Failure stages of landslides.  $s_u$  - Undrained shear strength;  $s_r$  - Remolded shear strength;  $F$  - Factor of safety.

A soil element that is involved in a landslide commonly passes through a pre-failure, a shear failure, and a post-failure stage (Terzaghi et al., 1996; Locat and Leroueil, 1997). In the pre-failure stage, the shear stress acting in the slope is below the shear strength of the soil – the slope is stable with a factor of safety being greater than 1 (Fig. 1.1A). With increasing shear stress, the soil passes from linear elastic to nonlinear plastic stress-strain behavior until the shear stress eventually reaches the shear strength, at a factor of safety  $\sim 1$  (Fig. 1.1B). It

further marks the initiation of a failure surface along which the failed soil mass slides during the post-failure stage (Fig. 1.1C). In ductile soil, the post-failure strength is more or less equal to the shear strength. However, brittle soil softens, leading to a decrease in stress after failure, until a level of constant stress is reached at large strains, which is called the remolded or residual strength  $s_r$ .

The factors that contribute to shear failure and thus to landslide initiation are diverse and may vary from slow geological processes operating on timescales of thousands of years to sudden short-term impacts operating on timescales of minutes to days. According to Eq. 1.1, they may be either (a) factors that increase the shear stress on the slope or (b) factors that decrease the shear strength of the slope material (Varnes, 1978; Duncan et al., 2014). Factors that increase the shear stress include (i) additional surcharge due to rain, infrastructure, fill, seepage, talus, and vegetation, (ii) the removal of lateral support caused by trenches, toe erosion, cuts, and quarries, (iii) an increase in lateral pressure due to water and ice in cracks and caverns or due to swelling of clay minerals, and (iv) cyclic loading by earthquakes, storms, explosions, traffic and machinery. Factors that decrease the shear strength include (i) geological factors like faults, discontinuities, inclined strata, and weak layers, (ii) weathering of primary deposits, including the physical disintegration of rock, removal of cement, drying of clays, and the clay neof ormation and transformation, and (iii) excess pore water pressure induced by increased water level or internal reorganization of the soil fabric.

## 1.2 Role of sensitivity in landsliding

Weathering of primary deposits has been recognized as important factor contributing not only to the pre-failure stage and landslide initiation, but also to softening during the post-failure landsliding (Kvalstad et al., 2005). This post-failure strength loss in the shear zone, which is typical for brittle soil (Fig. 1.1), is quantified by the sensitivity  $S$  (Terzaghi, 1944; Skempton and Northey, 1952):

$$S = s_u/s_r, \quad (1.4)$$

where the undrained and remolded shear strengths are measured at the same water content. Following the commonly accepted classification from Norsk Geoteknisk Forening (1974), soils are divided into categories of low sensitivity ( $S < 8$ ), medium high sensitivity ( $8 \leq S \leq 30$ ), high sensitivity ( $S < 30$ ), and quick clay ( $S > 30$  and  $s_r < 0.5kPa$ ).

Undisturbed soil with high sensitivity can exhibit a relatively large initial shear strength and, thus, a sharp decrease in strength during shear. The failure surface exhibits low remolded strength, resulting in landslides with long runout distance and dimensions that are difficult

to predict (Demers et al., 2014; L'Heureux et al., 2014a). Many progressive landslides have been recognized in sensitive soils of Canada and Scandinavia (Tavenas, 1984). During progressive failure, the post-failure softening behavior of the sensitive soil causes the failure surface to propagate from a local failure, often close to the toe of the slope, further in the slope (Locat et al., 2011) (Fig. 1.2). Following Bjerrum (1967) and Bishop (1971), the shear stresses and strains that develop in the slope during progressive failure do not mobilize a constant shear strength, but a strength that varies between undrained and remolded shear strength along the potential failure surface. Consequently, the sensitivity of the soil may determine the intensity and severity of progressive landslides.

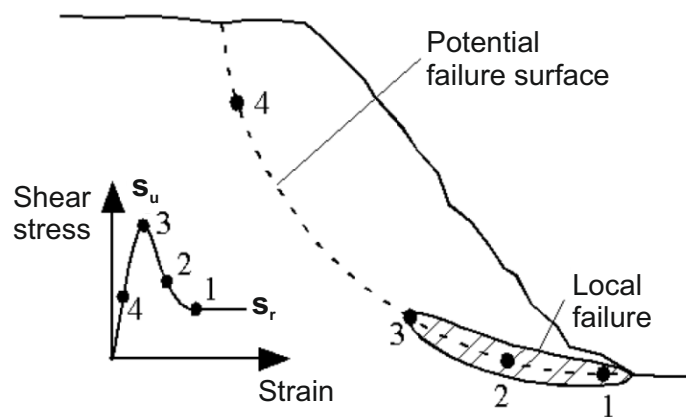


Fig. 1.2 Progressive failure along a circular failure surface.  $s_u$  - Undrained shear strength;  $s_r$  - Remolded shear strength (after Locat et al., 2011).

High sensitivities have been reported for post-glacial, brackish and marine clayey sediments from Scandinavia (Gregersen, 1981; Torrance, 1983; Rankka et al., 2004; Andersson-Sköld et al., 2005; Solberg et al., 2008), Canada (Lo and Becker, 1979; Leroueil et al., 1983; Torrance, 1983), Alaska (Kerr and Drew, 1968; Updike and Carpenter, 1986), and Japan (Egashira and Ohtsubo, 1982), as well as for weathered tephra from New Zealand (Smalley et al., 1980; Jacquet, 1990; Moon et al., 2015b), Indonesia (Wesley, 1977), Hawaii (Wieczorek et al., 1982), and Japan (Sasaki et al., 1974). The term tephra encompasses all unlithified volcanic airfall materials of any grain size and composition (Lowe, 2011). Sensitive soils, either of post-glacial or volcanic origin, occur globally (Fig. 1.3) and are considered to be an important subsoil for geotechnical design. Therefore, the pre- and post-failure behavior of sensitive soil has to be properly understood.

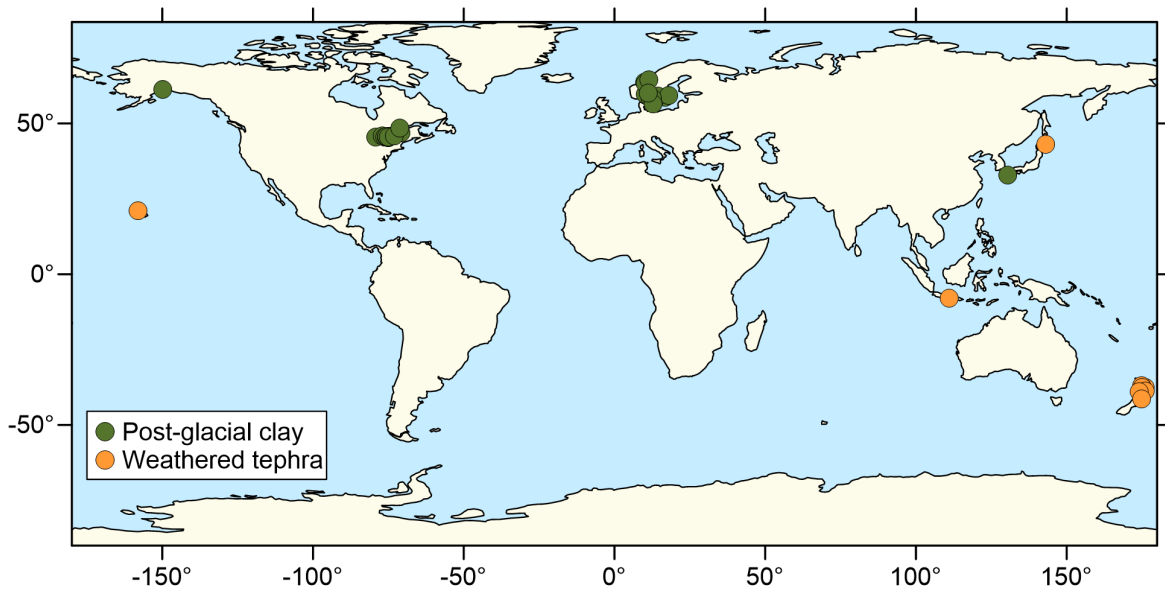


Fig. 1.3 Global distribution of sensitive post-glacial clays and sensitive weathered tephra. See text for references.

### 1.3 Cyclic shear strength of soil

In the pre-failure stage, one of the most extensively studied factors contributing to landslide initiation is the effect of cyclic loading on shear strength (Idriss and Boulanger, 2008). This is because cyclic loading not only increases shear stress on the slope due to ground shaking, but may also decrease shear strength by disruption of the soil.

In saturated non-cohesive soil, such as sands and unaltered tephra, cyclic loading disrupts the grain-to-grain contacts, causing the soil to compact. This results in excess pore pressure, which decreases the effective stress carried by the soil (Eq. 1.3). When the effective stress equals zero, the grain contacts are no longer under normal force and the soil changes into a liquefied state with no or very little shear strength. The 2011 Christchurch earthquake on the South Island of New Zealand is a notable example where liquefaction is considered to be an important cause of a large number of landslides in coastal non-cohesive sediments (Kaiser et al., 2012).

In cohesive silts and clays, the reduction in shear strength due to cyclic loading is considered to be a result of the mechanical disruption of bonds between clay particles (Idriss and Boulanger, 2008). The 1964 Prince William Sound, Alaska earthquake and the 1999 Chi-Chi, Taiwan earthquake are examples where cyclic softening, as introduced by Boulanger and Idriss (2006), caused considerable settlement and ground failures in cohesive soil (Idriss, 1985; Chu et al., 2004).

The liquefaction potential of non-cohesive sediments is commonly evaluated by field methods, such as standard penetration tests (SPT) or static cone penetration tests (SCPTU), using empirical correlations between data and field observations (Seed et al., 1983; Robertson and Wride, 1998; Youd et al., 2001). Alternatively, vibratory cone penetration tests (VCPTU) have been used to directly measure the liquefaction potential in situ by mechanically inducing cyclic loads into the sediment (Sasaki et al., 1984; Tokimatsu, 1988; Wise et al., 1999). Based on the concept of effective stress, the cyclic loading during VCPTU will both decrease cone resistance and increase induced pore water pressure in sediment layers with high liquefaction potential (Fig. 1.4). VCPT has also been successively applied to sensitive weathered tephra in New Zealand, showing depth intervals with increased vulnerability to cyclic loading (Jorat et al., 2014a, 2015; Moon et al., 2015a). However, no other in situ tests have been performed in order to assess the cyclic softening potential in cohesive soils like sensitive post-glacial clayey sediments.

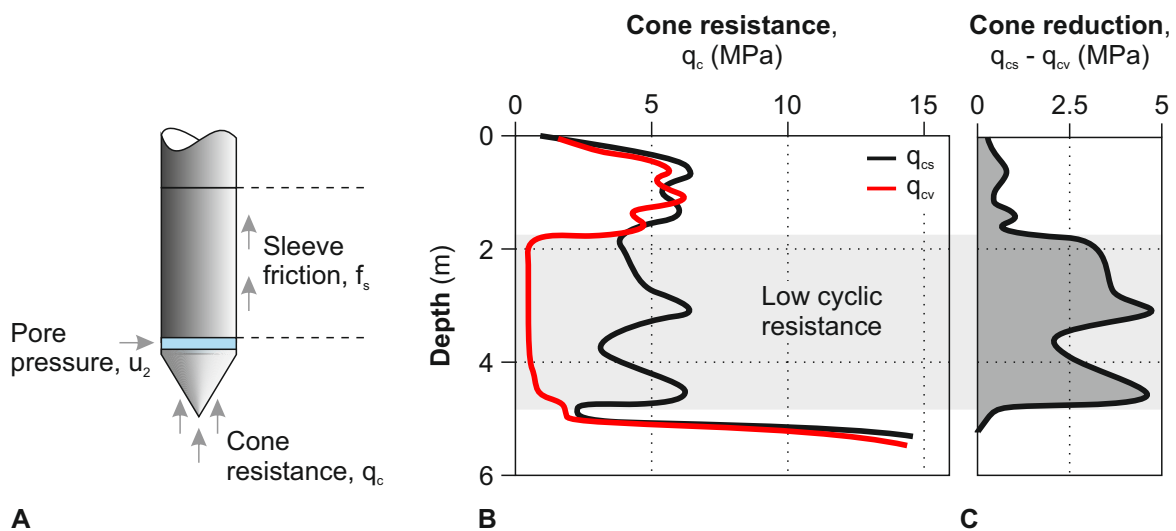


Fig. 1.4 Measurement of the in situ liquefaction potential by static and vibratory cone penetration testing. **A:** Schematic cone, commonly used for cone penetration testing (after Lunne et al., 1997). **B:** Comparison of static cone resistance  $q_{cs}$  with vibratory cone resistance  $q_{cv}$  in order to identify sediment layers with low cyclic resistance. **C:** Sediment layers with low cyclic resistance exhibit a peak in the cone reduction diagram (A and B after Sasaki et al., 1984).

The general understanding of soil response under cyclic loading requires additional laboratory methods under controlled stress and strain conditions, such as cyclic triaxial, cyclic simple shear, and torsional shear tests. Most previous laboratory-based studies on cyclic undrained behavior have focused on naturally deposited sand (Mohamad and Dobry, 1986; Alarcon-Guzman et al., 1988; Hyodo et al., 1994a; Georgiannou et al., 2008), clay

(Sangrey et al., 1969; Ansal and Erken, 1989; Yasuhara et al., 1992; Zergoun and Vaid, 1994), or silt-clay mixtures (Hyde and Brown, 1976; Guo and Prakash, 1999). Georgiannou et al. (2008) and Zergoun and Vaid (1994) performed a monotonic and a cyclic shear test on Fontainebleau sand and Cloverdale clay, respectively, and displayed the curves for each soil in a shear stress – mean effective stress diagram (Fig. 1.5). Consequently, the sand and clay samples have a lower shear strength when subjected to cyclic loading than compared to monotonic loading. This observation highlights the need to consider cyclic loading in shear strength and slope stability assessments in regions with frequent earthquake shaking or other types of cyclic loading.

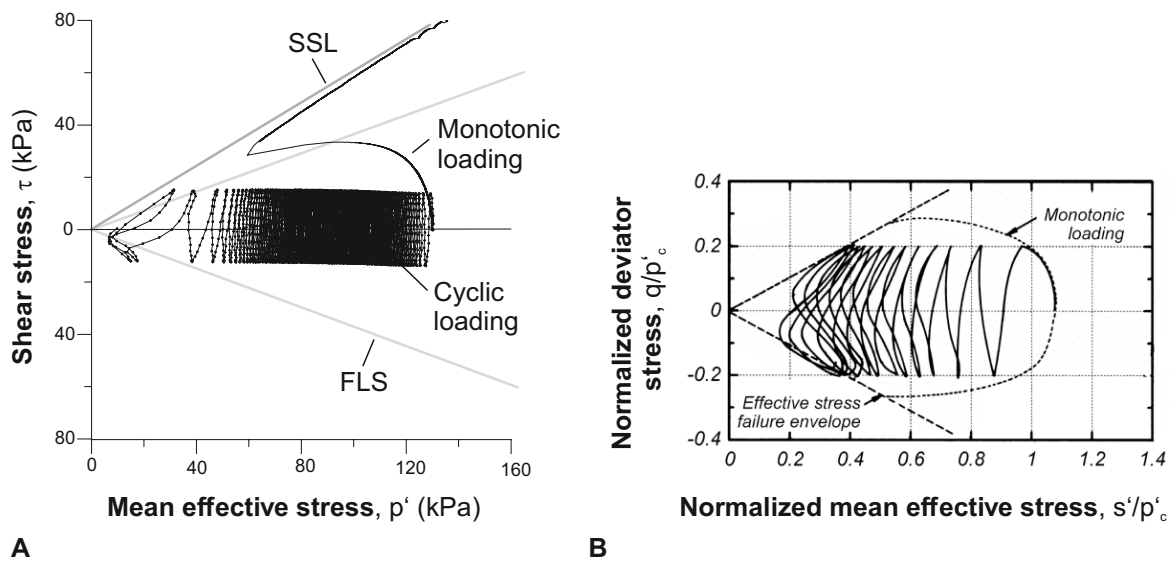


Fig. 1.5 **A:** Monotonic and cyclic torsional shear tests on Fontainebleau sand (after Georgiannou et al., 2008). *SSL* - Stead state line; *FLS* - Flow liquefaction surface;  $p' = (\sigma'_a + 2\sigma'_r)/3$ , with  $\sigma'_a$  and  $\sigma'_r$  being the axial and radial effective stresses. **B:** Monotonic and cyclic triaxial shear tests on Cloverdale clay (after Zergoun and Vaid, 1994).  $q = \sigma'_a - \sigma'_r$ ;  $s' = (\sigma'_a + \sigma'_r)/2$ ;  $p'_c = (\sigma'_{ac} + 2\sigma'_{rc})/3$ , with  $\sigma'_{ac}$  and  $\sigma'_{rc}$  being the axial and radial effective consolidation stresses.

The cyclic loading behaviour of sensitive post-glacial clays has been investigated in the past through laboratory studies, and is relevant for civil engineering (Lo, 1969; Lefebvre and Leboeuf, 1987; Wichtmann et al., 2013). Although tephra is a relevant subsoil in many tectonically active areas such as New Zealand and Japan (Briggs et al., 2005; Chigira, 2014), knowledge about the cyclic shear strength of tephra is limited to crushable unaltered tephra (Miura et al., 2003; Orense and Pender, 2015; Wiemer and Kopf, 2016). Yoshimoto et al. (2013) and Orense and Pender (2015) performed undrained cyclic triaxial tests on various

soils and concluded that the resistance to undrained cyclic loading is low for sand, high for clay, and intermediate for unaltered tephra (Fig. 1.6).

Volcanic glass is a major constituent of tephra, which weathers to secondary clay minerals within several thousands of years (Lowe, 1986). Subsequently, this alteration increases the proportion of clay minerals, likely changing the geotechnical behavior of the tephra such as its cyclic shear strength. However, the cyclic loading behavior of weathered sensitive tephra has not been analyzed and therefore it remains unknown if sensitive tephra exhibits undrained cyclic shear strength properties similar to granular soils, e.g. sand and unaltered tephra, or cohesive soil, e.g. clay and silt.

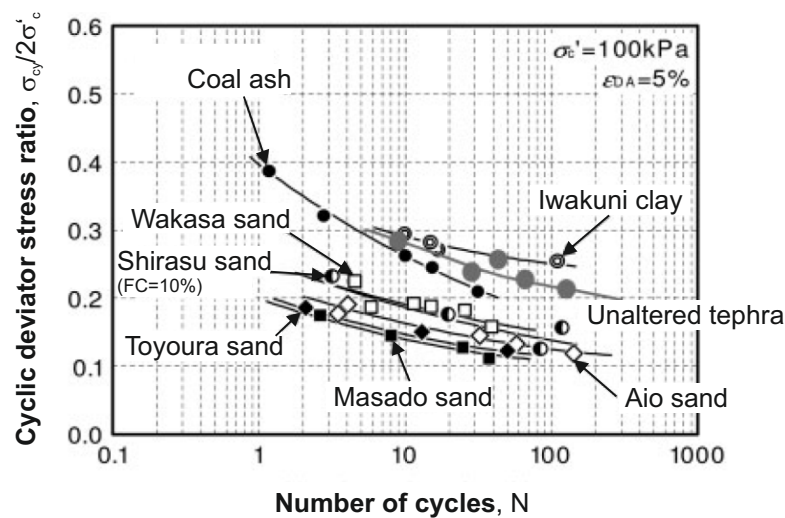


Fig. 1.6 Cyclic deviator stress ratios - number of cycles to failure relationship for different sands, sand with fines content, coal ash, unaltered tephra (pumice), and clay (after Yoshimoto et al., 2013; Orense and Pender, 2015).  $\sigma_{cy}$  - Single axial stress amplitude;  $\sigma'_c$  - Effective isotropic consolidation stress.

## 1.4 Development of sensitive soil

High sensitivities have been reported in post-glacial clayey sediments as well as in weathered tephra. Aspects that are considered relevant for the sensitivity development are discussed and gaps in knowledge are pointed out for both soil types separately.

### 1.4.1 Post-glacial clay

High sensitivities have first been recognized in post-glacial clayey sediments from the Northern Hemisphere (Skempton and Northey, 1952) and many researchers have investigated

the processes that caused the development of sensitivity in such soils (Rosenqvist, 1953, 1966; Smalley, 1971; Quigley, 1980). Torrance (1983) presented a first comprehensive idea about sensitivity development in post-glacial clays that includes factors contributing to a high undrained shear strength and/or a low remolded shear strength (Tab. 1.1). According to Torrance (1983), highly sensitive soil from the Northern Hemisphere originates from the sedimentation of fine-grained glacial materials in the marine environment that have been leached after subaerial exposure.

The high cation concentration of seawater leads to the formation of thin diffuse electric double layers at the interface between water and the low-activity illitic clay minerals, which dominate the clay fraction of the sediment. The thin electric double layers decrease the repelling forces between the clay particles, which, together with a high suspension concentration and a low settling rate, favor a flocculated soil structure with a high void ratio and thus a high natural water content.

The flocculated soil structure is essential for the development of high sensitivity, because it (a) limits the consolidation of the soil when overburden pressure increases, leading to a constantly high natural water content. It further (b) maintains a relatively high undrained shear strength due to van der Waals bonding forces and electrostatic Coulomb attractions while the cations are subsequently leached from the pore water under fresh water conditions (Israelachvili, 2011). The rapid development of cementation bonds between clay particles may play a role in some carbonate soils (Sangrey, 1972), but is considered not to be the primary factor for the development of high undrained shear strength in most soils (Torrance, 1983). The post-depositional leaching of cations from the pore water increases the thickness of the diffuse double layer, which results in a decrease in net attractive forces when the contacts between clay particles are disrupted (Israelachvili, 2011). This results in an overall decrease of cohesion in the soil, which, together with a natural water content close to the liquid limit, results in a low remolded shear strength.

### **1.4.2 Weathered tephra**

In contrast to post-glacial clay, the sensitivity development in weathered tephra is still not well understood. This may be due to the the complex interrelation between the chemical composition of the primary tephra, which can be highly variable, and the weathering process, which depends on rainfall, temperature, and drainage (Lowe, 1986; Moon et al., 2015b). The clay minerals of the kaolin group, allophane, imogolite, kaolinite, and halloysite, are preferential weathering products of rhyolitic tephra (Churchman and Lowe, 2012) and are considered to increase the risk of landslides (Kirk et al., 1997). However, the role of the different kaolin clay minerals on the sensitivity development is controversial.

Table 1.1 General model of sensitivity development in post-glacial clays and weathered tephra (after Torrance, 1983, 1992).

Factors producing a high undisturbed strength		
	Depositional	Post-depositional
Post-glacial clays	<ul style="list-style-type: none"> <li>• Flocculation</li> <li>• Salinity</li> <li>• High suspension concentration</li> </ul>	<ul style="list-style-type: none"> <li>• Cementation bonds rapidly developed</li> <li>• Slow load increase</li> </ul>
Weathered tephra	<ul style="list-style-type: none"> <li>• Allophanic mineralogy</li> </ul>	<ul style="list-style-type: none"> <li>• Diagenesis and weathering to produce halloysite, imogolite, and ferrihydrite</li> </ul>
Factors producing a low remolded strength		
	Depositional	Post-depositional
Post-glacial clay	<ul style="list-style-type: none"> <li>• Low-activity illitic minerals dominate</li> </ul>	<ul style="list-style-type: none"> <li>• Leaching</li> <li>• Decrease in <math>w_L &gt;</math> Decrease in <math>w</math></li> <li>• Reducing conditions</li> <li>• Inhibition of high-swelling smectite formation</li> <li>• Minimal consolidation</li> </ul>
Weathered tephra	<ul style="list-style-type: none"> <li>• Airfall origin</li> <li>• High void ratio</li> <li>• Allophanic mineralogy</li> </ul>	<ul style="list-style-type: none"> <li>• Void ratio increase by dissolution and removal of soluble material during weathering and diagenesis</li> <li>• Dispersing agents</li> </ul>

Jacquet (1990) analyzed various weathered tephra from the North Island of New Zealand and concluded, together with a discussion by Torrance (1992), that a high undrained shear strength arises from (a) a primary allophanic mineralogy and from (b) electrostatic attractions and/or grain-to-grain contacts between neoformed allophane, imogolite, and halloysite agglomerates (Tab. 1.1). A low remolded shear strength is favored by (a) the airfall origin of the tephra, (b) a high void ratio, and (c) the mechanical disruption of attractive forces between the agglomerates during shear. Wesley (1973, 1977) analyzed weathered tephra from Indonesia and concluded that halloysite, rather than allophane, correlates with high sensitivity. This observation is consistent with high sensitivities found in a weathered halloysite-rich tephra from Japan (Sasaki et al., 1974). Moon et al. (2015b) suggested that airfall deposition of rhyolitic tephra from distal volcanic centers produces fine grained soil with high void ratio, low permeability, and high natural water content. This condition accelerates the dissolution of primary tephra, mostly volcanic glass and feldspar, and the precipitation of halloysite clays in the pore spaces (Churchman and Lowe, 2012). The weathering provides cations that promotes the formation of thin diffuse electric double layers around the neoformed halloysite particles. As a consequence, the halloysite particles are attracted by van der Waals bonding forces and electrostatic Coulomb attraction forces and form agglomerates with high cohesion, maintaining a high natural water content in the soil while weathering continues (Moon et al., 2015b). Progressive weathering and inflow of fresh water may decrease the cation concentration in the pore water, which leads to thicker diffuse electric double layers, a decrease in net attractive forces, and thus to a decrease in cohesion. Moon et al. (2015b) concluded that the low cohesion and high natural water content in the weathered tephra are the main reasons for a low remolded shear strength, leading to a high sensitivity.

Halloysite exhibits various morphologies with tubes, spheroids, polyhedrons, and plates, being the most common (Joussein et al., 2005) and some research aimed to link a specific halloysite morphology with the sensitivity. Jacquet (1990) discussed possible influences of kaolin morphologies on sensitivity, but did not correlate specific halloysite morphologies with sensitivity. Smalley et al. (1980) measured sensitivities of  $S = 140$  on samples taken from the slide-prone weathered tephra layer of the Omokoroa flow slide, Tauranga Harbour, North Island of New Zealand, which consisted almost entirely of spheroidal halloysite. The spheroids had only few interparticle contacts, which, together with low plasticity, high natural water content, and low activity of the weathered tephra layer, led Smalley et al. (1980) to conclude that the high sensitivity could be explained by the inactive-particle, short-range-bond theory (Smalley, 1971). Accordingly, short range bonds exist between uncharged particles, e.g. quartz, and depend mainly on particle contacts, which become ineffective when the contact is disturbed. Moon et al. (2015b) summarized recent research on sensitivity

in weathered tephra from the Tauranga Harbour region and reported the coexistence of spheroidal, tubular, and platy halloysite morphologies in soil samples from the Omokoroa flow slide. The authors further suggested that, analogous to the post-glacial illitic clays from the Northern Hemisphere, platy halloysite may play a role in the sensitivity development in rhyolitic tephra.

So far, the occurrence of halloysite and the effect of different morphologies on the sensitivity development of weathered tephra have only been studied on single outcrop samples. In order to gain a comprehensible understanding of sensitivity development in weathered tephra, a systematic correlation between halloysite and sensitivity has to be conducted over a complete depositional sequence.

## 1.5 Motivation and research hypotheses

Three major knowledge gaps about the pre- and post-failure behavior of sensitive soil have been identified, which form the basis motivation for this doctoral thesis: In the pre-failure stage, (1) the in situ cyclic softening behavior of sensitive post-glacial sediments and (2) the cyclic shear strength of weathered sensitive tephra are unknown. In the post-failure stage, (2) the development of high sensitivity in weathered tephra has only been studied on single outcrop samples and no systematic correlation between halloysite and sensitivity has been conducted over a complete depositional sequence.

Based on the knowledge gaps, the following three research hypotheses are formulated. They are studied in chapters 3 - 5 and addressed in the concluding chapter 6 of this doctoral thesis:

1. Cyclic loading affects the in situ shear strength of sensitive glacio-marine soil.
2. Cyclic shear strength of sensitive weathered tephra differs from post-glacial sensitive clay.
3. High sensitivity in weathered tephra is caused by specific halloysite morphologies.

## 1.6 Study areas

The research hypotheses are investigated through two case studies: A coastal retrogressive submarine landslide in glacio-marine fjord sediments, Norway (Fig. 1.7A); and a coastal subaerial flow slide in weathered tephra, New Zealand (Fig. 1.7B). These landslides were selected for the following reasons:

- (i) They occurred in the coastal zone and affected society, economy, and the natural environment on land as well as under water.
- (ii) They occurred in sensitive post-glacial sediments and sensitive weathered tephra, respectively.
- (iii) Some aspects of their failure mechanism and post-failure mobilization processes are not well understood.

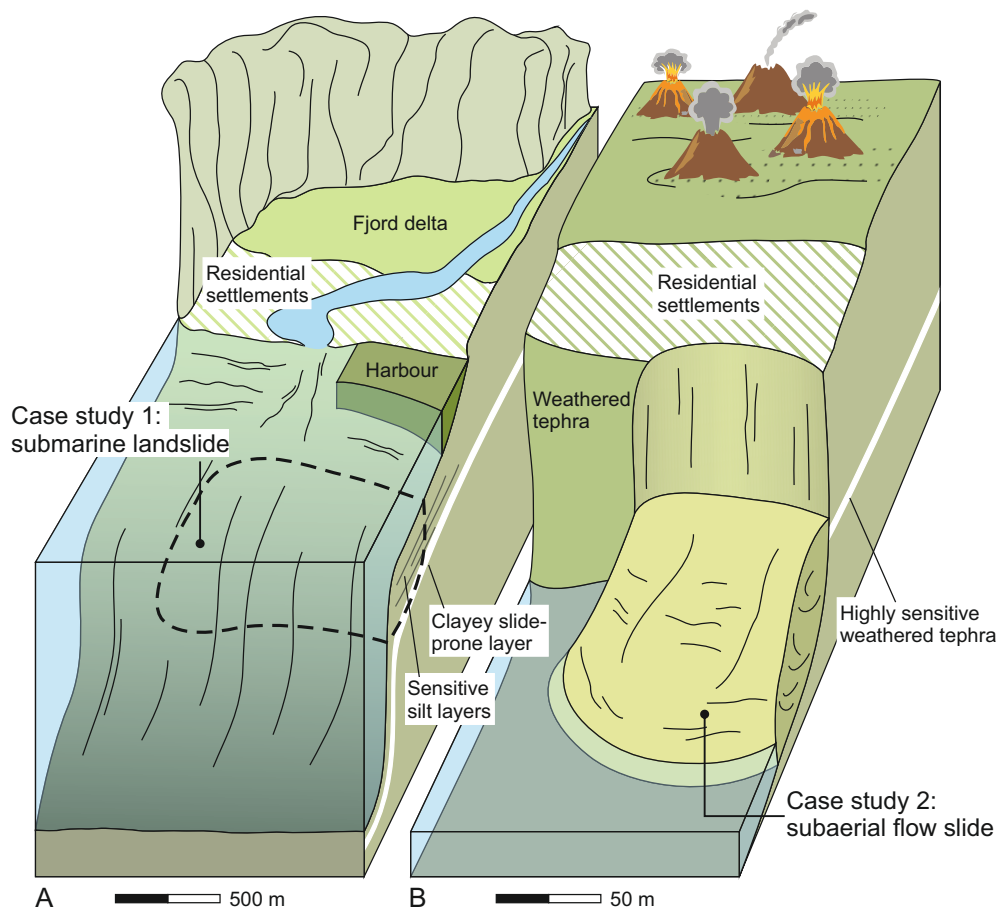


Fig. 1.7 Schematic view of the two case studies investigated in this doctoral thesis. Note that vertical dimensions are not to scale. **A:** Submarine Orkdalsfjord landslide in post-glacial sensitive silts, Norway. **B:** Subaerial Omokoroa flow slide in altered sensitive tephra deposits, New Zealand.

### 1.6.1 Submarine Orkdalsfjord landslide, Norway

The first case study is the submarine Orkdalsfjord landslide, which failed in 1930 in sensitive glacio-marine fjord sediments near the city Orkanger, mid Norway (Fig. 1.8). A volume of

$18.5 \cdot 10^6 m^3$  was evacuated downslope initiating an up to 15-m high tsunami (L'Heureux et al., 2014b). During this event, one person was killed, port facilities were damaged, and submarine cables at a distance of up to 18 kilometers from the landslide were broken (L'Heureux et al., 2014b). The first failure happened near the harbor and was most likely initiated in stratified clayey to sandy fjord sediments with moderately high sensitivity (Norsk Geoteknisk Forening, 1974; Stegmann et al., 2017). After failure occurred, the sensitive sediments became mobilized and progressed along an underlying clay layer, which acted as sliding surface (L'Heureux et al., 2014b). It was assumed that the submarine landslide was the result of a combination of human activity along the shoreline, unfavorable groundwater conditions, and steep shoreline slopes (L'Heureux et al., 2014b).

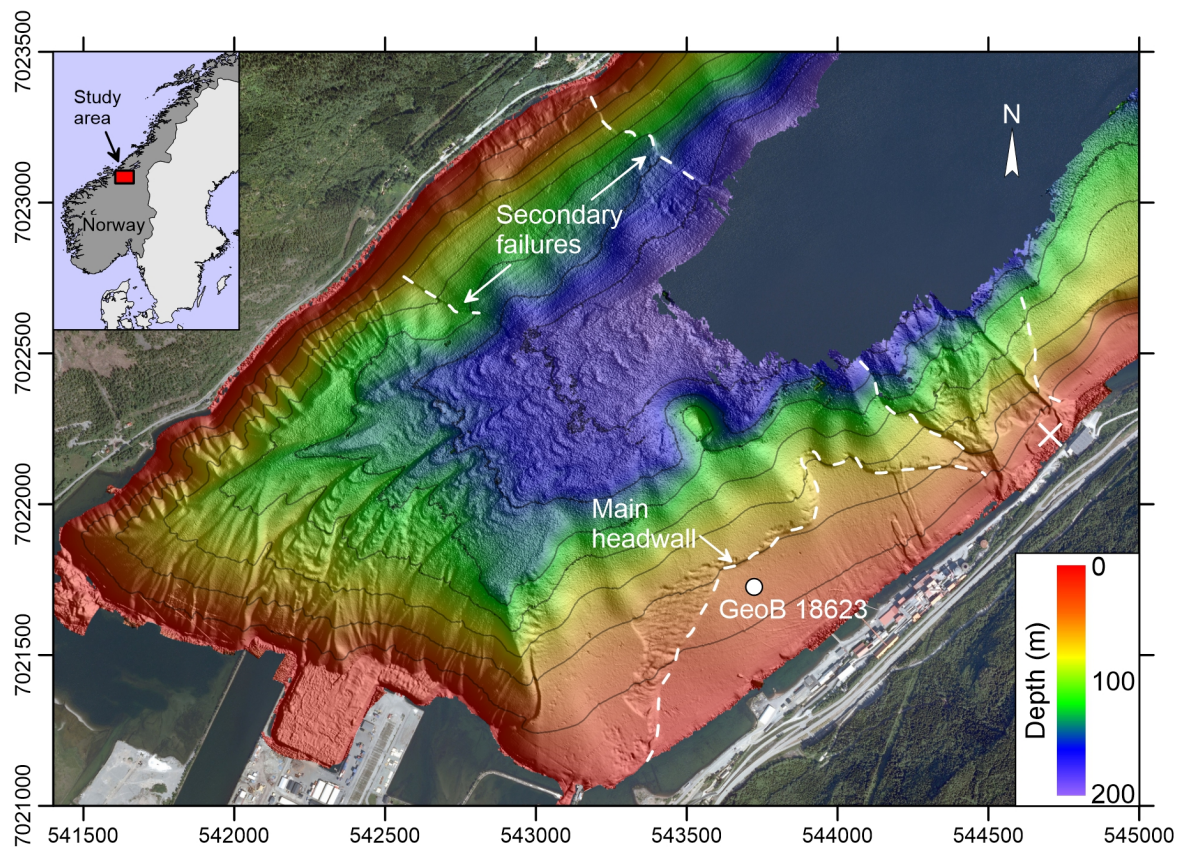


Fig. 1.8 Swath bathymetry over the Orkdalsfjord landslide, Norway (after L'Heureux et al., 2014b). The white X marks the location of the initial failure. Data courtesy of NGU. UTM coordinates in m.

Cyclic loading, manifested by earthquakes in this region (Fjeldskaar et al., 2000), blasts, or machine vibrations, may also have contributed to the initiation of the Orkdalsfjord landslide. Understanding the role of cyclic loading in landslide initiation, requires the precise knowledge of the soil response under cyclic loading. Geotechnical in situ tests are the preferred option

for such soil response analyses, because sampling causes the sediment to become disturbed during coring, transport, and sample preparation. However, the in situ soil response to cyclic loading has only been investigated for sand or weathered tephra (Sasaki et al., 1984; Tokimatsu, 1988; Jorat et al., 2015; Moon et al., 2015b). The in situ behavior of sensitive clays and silts under cyclic loading has not been tested. Therefore, the submarine Orkdalsfjord landslide is chosen in order to address the research hypothesis:

(1) *Cyclic loading affects the in situ shear strength of sensitive glacio-marine soil.*

The effect of cyclic loading on the in situ shear strength of fine-grained glacio-marine fjord sediments was investigated during the expedition POS472 in 2014 (Stegmann et al., 2017), by comparing a static and a vibratory CPTU depth profile, both obtained from the intact slope close to the Orkdalsfjord landslide headwall. The results are validated by laboratory cyclic triaxial tests on gravity core samples from the upper 4.6 m of the intact fjord sediments.

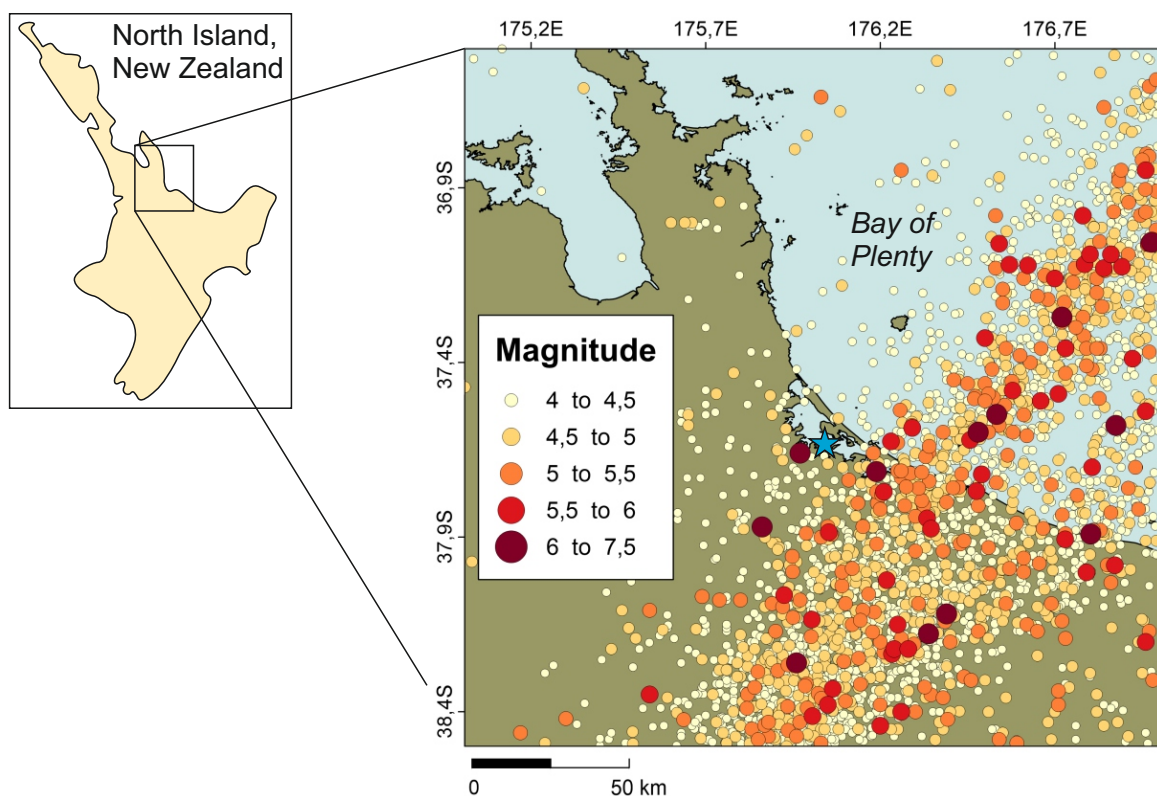


Fig. 1.9 Distribution of earthquakes with a moment magnitude larger than 4 that occurred in the Bay of Plenty region between 1838 and 2016. The blue star marks the position of the Omokoroa flow slide. Earthquake data: [www.geonet.org.nz](http://www.geonet.org.nz).

### 1.6.2 Subaerial Omokoroa flow slide, New Zealand

The second case study is the subaerial coastal flow slide at Omokoroa, Bay of Plenty, North Island of New Zealand, where  $\sim 10,000 m^2$  of sensitive weathered tephra was transported downslope over a distance of 150 m into a lagoon in 1979 (Gulliver et al., 1980), as well as during two minor reactivations in 2011 and 2012 (Moon et al., 2015b). The term flow slide refers to a flow-like behavior of the failed soil mass as defined by (Varnes, 1978). The flow slide occurred after a period of prolonged heavy rainfall in an adjacent residential district and caused five houses to be relocated (Gulliver et al., 1980). The weathered tephra succession at the Omokoroa flow slide is rich in halloysite, having morphologies that vary between tubes, spheroids, polyhedrons, plates, and books (Moon et al., 2015b; Cunningham et al., 2016). The 1979 event was likely initiated in a white, highly sensitive layer with high spheroidal halloysite concentration (Smalley et al., 1980).

Earthquake shaking is a frequent cause of cyclic loading on the North Island of New Zealand (Fig. 1.9). However, thus far the cyclic loading behavior of weathered sensitive tephra has not been studied. Therefore, the research hypothesis:

*(2) Cyclic shear strength of sensitive weathered tephra differs from post-glacial sensitive clay,*

is addressed by a program of monotonic and cyclic triaxial tests on samples recovered from an intact soil unit of the Omokoroa flow slide. The main objectives are to study: (a) the static undrained shear strength and angle of internal friction, (b) the effect of cyclic shear stress on shear strain development, and (c) the cyclic shear strength of the weathered tephra using cyclic contour diagrams, initially developed to analyze the comprehensive cyclic undrained behavior of Norwegian post-glacial marine clay (Andersen and Lauritzen, 1988).

In addition, the role of halloysite and its various morphologies in the development of sensitivity in weathered tephra, and thus in flow sliding with long runout distance, is poorly understood. Therefore, the hypothesis:

*(3) High sensitivity in weathered tephra is caused by specific halloysite morphologies*

is tested. The stratigraphic build up, secondary clay mineralogy, and geotechnical properties of the weathered tephra succession of the Omokoroa flow slide are analyzed along a drill core, which was bored in 2013 in unfailed material near the headwall (Moon et al., 2015b). This delivers precise information about changes in halloysite concentration, halloysite morphology, and sensitivity with depth. Weak zones with high concentrations of

spheroidal halloysite may be identified that coincide with high sensitivities, as observations of the Omokoroa flow slide by Smalley et al. (1980) indicated. From Eq. 1.4, the sensitivity is controlled by the ratio of undrained and remolded shear strengths of the soil. Therefore, samples are taken from undisturbed sediment, and from the remolded failure surface, respectively, to study the effect of remolding on the spheroidal halloysite particle arrangement at nanoscale dimensions. This procedure may provide insight into the development of high sensitivity in altered halloysite-rich tephra.

## 1.7 Organization of this thesis and contribution to scientific journals

The 'Integrated Coastal Zone and Shelf-Sea Research' Training Group (INTERCOAST) is an interdisciplinary graduate program between Germany and New Zealand, which focuses on environmental change, development impacts, and societal aspects of the coastal zone. This doctoral thesis is part of the research theme 'Pulses of coastal sediment mobilization - Causes, consequences and mitigation' and aims to broaden our understanding of failure mechanisms and post-failure softening processes of coastal landslides in sensitive soil.

This chapter gives an outline of this thesis and briefly summarizes the scientific publications which I produced in the scope of this PhD project. The three publications are reprinted in fulltext as chapters 3 - 5 and focus on different aspects of cyclic loading behavior of sensitive soil and the development of sensitivity in weathered tephra. My contribution and the individual contributions of all co-authors are described in detail at the end of each publication.

*Chapter 1* provides an overview of cyclic loading behavior of soil and the development of sensitivity in post-glacial clay and weathered tephra. It then introduces the overall motivation and research hypotheses of this doctoral thesis that will be presented in the three publications.

*Chapter 2* provides a short overview of all methods that were used to collect data for the three publications.

*Chapter 3* presents in situ and laboratory cyclic loading experiments conducted on the Orkdalsfjord submarine landslide, Mid Norway, in order to address how cyclic loading affects the shear strength of sensitive glacio-marine soil (Hypothesis 1). This research was published in 2016 in the peer-reviewed conference proceedings *Submarine Mass Movements*

*and their Consequences.*

*Chapter 4* presents monotonic and cyclic triaxial loading experiments on a weathered, sensitive tephra from the Omokoroa flow slide, North Island of New Zealand to address how shear strength of sensitive weathered tephra is affected by cyclic loading (Hypothesis 2). This research was submitted to *Géotechnique* on March 31th, 2017 and is currently in revision.

*Chapter 5* presents shear strength and mineralogical results along a vertical profile close to the Omokoroa flow slide, in order to study the causes of high sensitivity development in weathered tephra (Hypothesis 3). This research was published in 2017 in *Geology*.

*Chapter 6* recapitulates the main conclusions of this doctoral thesis with respect to the research hypotheses.

*Appendixes A* and *B* list conferences and abstracts from the last three years.

*Appendix C* presents a manuscript about geotechnical laboratory results and constitutive modeling of a high-density sand from the North Sea, Germany. This research is in preparation for submission to International Journal of Geomechanics.

# Chapter 2

## Methods

This chapter briefly summarizes the field and laboratory methods that were performed or which provided data for this PhD project.

### 2.1 Field methods

#### 2.1.1 Bathymetry and topography

Bathymetric data from Orkdalsfjord were collected in 2003 and 2009 by the Geological Survey of Norway (NGU) using a 250  $kHz$  interferometric sidescan sonar system (GeoAcoustics), which was mounted onboard the R/V Seisma (L'Heureux et al., 2014b). The bathymetric grids have 1  $m$  by 1  $m$  cell size and were used with courtesy of NGU to create the map in Fig. 3.1.

Topography data from the Omokoroa flow slide were measured in 2012 by V. G. Moon, W. de Lange, and colleagues, using a Trimble VX LIDAR scanner (Moon et al., 2015a). Multiple scans of the headwall and remnant landslide deposits were combined into a single topographic grid, which was used to create the perspective map and the cross-profile of the Omokoroa flow slide in Fig. 5.1.

#### 2.1.2 Static and vibratory cone penetration testing

The static (SCPTU) and vibratory cone penetration tests (VCPTU) were conducted at study site *GeoB18623* during R/V Poseidon expedition POS472 in 2014 by W. Schunn, M. Lange, S. Kreiter, and myself, using the Geotechnical Offshore Seabed Tool (GOST) (Jorat et al., 2014b). The system uses a 5  $cm^2$  high resolution piezovibrocone, which measures cone resistance  $q_c$ , sleeve friction  $f_s$ , and pore water pressure  $u_2$ , along a continuous vertical profile

while pushed at constant speed into the seafloor. The VCPTU imposes additional cyclic loading with an amplitude of  $0.38\text{ mm}$  at a frequency of  $4.9\text{ Hz}$ . The static and vibratory cone resistance and induced pore water pressure profiles were used in the first publication (Chapter 3).

### 2.1.3 Coring and sampling

Two gravity cores, *GeoB18623-1* and *GeoB18623-2*, were retrieved during R/V Poseidon expedition POS472 in 2014. The sediment description and sampling for subsequent analyses were performed on core *GeoB-18623-1* by, N. Baeten, A. Rösner, R. Roskoden, W. Li, and myself and formed the basis for the sedimentological and geotechnical analyses presented in the first publication (Chapter 3).

18 thin-walled push tube samples were recovered from the Pahoia Tephra of the Omokoroa flow slide headwall, forming the basis for the triaxial testing program presented in the second publication (Chapter 4). The sampling campaign was performed by T. Goetz, T. Manderson, C. Morcom, J. Rau, B. Stewart, P. Mills, and myself.

A 40-m-long core, *Omok-1*, was bored via rotary flush drilling in unfailed material near the headwall of the Omokoroa flow slide in 2013. The drilling was performed by the companies Perry Geotech and Brown Bros under supervision of E. Jorat, T. Mörz, S. Kreiter, V. G. Moon, and W. de Lange. The sediment description was performed by E. Jorat and myself and forms the basis for the stratigraphic profiles in Figs. 4.1, 5.1, and 5.2. The drill core is the basis for subsequent mineralogical analyses and geotechnical testing presented in the third publication (Chapter 5).

### 2.1.4 Bore hole logging

In a second borehole, *Omok-2*, drilled in 2013 close to *Omok-1*, the bulk density and borehole diameter were measured using a 9239 Series Compensated Density Tool from the RDCL company, which included a LS gamma density and a caliper log. In the *Omok-1* borehole, three pore pressure sensors from GLÖTZL Baumesstechnik were installed in 2013 in order to measure the piezometric pressure at 12, 21, and 27.5 m depth. The bulk density, borehole diameter, and piezometric pressure are presented in Fig. 4.1 and were used to calculate the consolidation stress for triaxial testing in the second publication (Chapter 4).

## 2.2 Laboratory methods

### 2.2.1 Physical properties

Grain size distribution was determined on core *GeoB-18623-1* and on *Pahoia Tephra* samples used in the first and second publication, respectively, using a Beckman Coulter Laser diffraction particle size analyzer LS 13320 (McGregor et al., 2009). Water content, Atterberg limits, and activity were obtained following NZS 4402.4.1.1:1986 (1986); ASTM D 4318-10 (2010).

### 2.2.2 Mineralogy

The mineralogy of core *Omok-1* was measured by X-ray diffraction using a Philips PW analytical diffractometer, and quantification was performed using QUAX software (Vogt et al., 2002). The halloysite clay morphologies were further analyzed via scanning electron microscopy using a Zeiss Supra40 microscope (Reed, 2005). The relative abundance of halloysite particles having distinct morphologies were quantified by D. Seibel using a point-counting approach (Frolov and Maling, 1969; Seibel, 2015). These data were used in publications 2 and 3 (Chapter 4 and 5).

### 2.2.3 Shear strength

Undrained and remolded shear strength was measured via vane shear tests along cores *GeoB18623-1* and *Omok-1* (DIN 4094-4:2002-01, 2002). Monotonic and cyclic triaxial tests were performed following DIN 18137-2:2011-04 (2011) using the Dynamic Triaxial Testing Device Kreiter et al. (2010b).



## Chapter 3

# In situ cyclic softening of marine silts by vibratory CPTU at Orkdalsfjord test site, Mid Norway

Max O. Kluger<sup>1</sup>, Stefan Kreiter<sup>1</sup>, Jean-Sebastien L'Heureux<sup>2</sup>, Sylvia Stegmann<sup>1</sup>, Vicki G. Moon<sup>3</sup>, and Tobias Mörz<sup>1</sup>

<sup>1</sup>MARUM–Center for Marine Environmental Sciences, University of Bremen, Leobener Straße, 28359 Bremen, Germany

<sup>2</sup>Norwegian Geotechnical Institute, 7034 Trondheim, Norway

<sup>3</sup>School of Science, University of Waikato, Private Bag 3105, Hamilton 3240, New Zealand

Published in *Submarine Mass Movements and their Consequences*, Advances in Natural and Technological Hazards Research 41, 2016; p 201-209

doi:10.1007/978-3-319-20979-1\_20; ©2016 Springer International Publishing Switzerland

### Abstract

Earthquake induced cyclic loading has the potential to destabilize submarine slopes either by liquefaction in coarse-grained deposits or by cyclic softening in cohesive sediments. Vibratory cone penetration tests (VCPTU) represent a new approach for the evaluation of cyclic softening in fine grained sediments. In the past, VPCTU were utilized to evaluate liquefaction potential of sands, but cyclic softening of fine-grained marine sediments has not yet been tested with VCPTU in situ. At the study site in Orkdalsfjord, mid Norway marine

clayey silt deposits are interbedded with coarse silt and clay layers. Static and vibratory CPTU were performed down to 19 m penetration depth using the Geotechnical Offshore Seabed Tool (GOST) and in addition, two gravity cores were taken for cyclic triaxial testing and geotechnical index tests. From static and vibratory CPTU a number of coarse silt layers with a distinct drop in cyclic cone resistance were identified. Compared to surrounding finer sediments the coarse silt layers exhibited a higher potential for cyclic softening. This assumption is supported by cyclic triaxial tests on very coarse and surrounding medium-coarse silts, respectively, revealing a strong loss of cyclic shear strength in a controlled and documented stress-strain regime. This study highlights the potential for VCPTU as a promising tool to qualitatively evaluate the vulnerability of marine silts to cyclic softening. In combination with advanced laboratory tests these results are envisioned to help better identifying submarine slopes subjected to failure during earthquakes.

**Keywords** Cyclic softening · Vibratory CPTU · Marine silt · In situ

### 3.1 Introduction

Submarine and near-shore slope failures often result from earthquakes or other forms of cyclic loading such as waves, tides or from human activities like blasting or machine vibrations. In order to assess the liquefaction potential in sands (Ishihara, 1985; Youd et al., 2001) or the cyclic softening behaviour in cohesive soils (Boulanger and Idriss, 2006, 2007), cone penetrometer (CPTU) data and empirical methods are commonly used in practice (Seed et al., 1983; Robertson and Wride, 1998). Alternatively, vibratory cone penetration tests (VCPTU) may have potential to directly determine the cyclic behaviour of in situ soils as they mechanically induce cyclic loads into the sediment (Sasaki et al., 1984; Tokimatsu, 1988; Wise et al., 1999; Jorat et al., 2014a). When pushing a vibratory CPTU tip in a liquefiable soil, the cone resistance ( $q_{cv}$ ) is substantially reduced compared to that from a static test ( $q_{cs}$ ). In order to relate  $q_{cs}$  and  $q_{cv}$ , Sasaki et al. (1984) proposed the reduction ratio ( $RR$ ):

$$RR = 1 - q_{cv}/q_{cs} \quad (3.1)$$

Following Tokimatsu (1988), sediments with  $RR$  values of more than 0.8 exhibit high liquefaction potential. In addition to high  $RR$  values, liquefiable sediment layers often show an increase in the induced pore pressure (e.g. Mitchell, 1988; Bonita, 2000). To our knowledge, most VCPTU studies found in the literature have evaluated the liquefaction potential of terrestrial and marine sands only. Here we evaluate the cyclic behaviour of fine-grained marine soils from Orkdalsfjord, mid Norway, based on both CPTU and VCPTU

profiles obtained with the Geotechnical Offshore Seabed Tool (GOST). The in situ data set is combined with soil index properties and compared to the results of cyclic undrained triaxial tests.

## 3.2 Geological setting

Orkdalsfjord is a 25–30 km long branch of the Trondheimsfjord located 25 km southwest of Trondheim, mid Norway. The sediment strata consists of layered loose fine sand, silt and silty clay deposits originating from the Orkla river (Bjerrum, 1971). In May 1930 a submarine retrogressive landslide occurred along the fjord initiating a 15 m high tsunami wave that caused damage to harbour installations and killed one person (L'Heureux et al., 2014b). The volume of sediment that evacuated downslope of the 8–12 m high and 3 km long headwall is estimated to  $18.5 \cdot 10^6 \text{ m}^3$  (Fig. 3.1, L'Heureux et al. (2014b)).

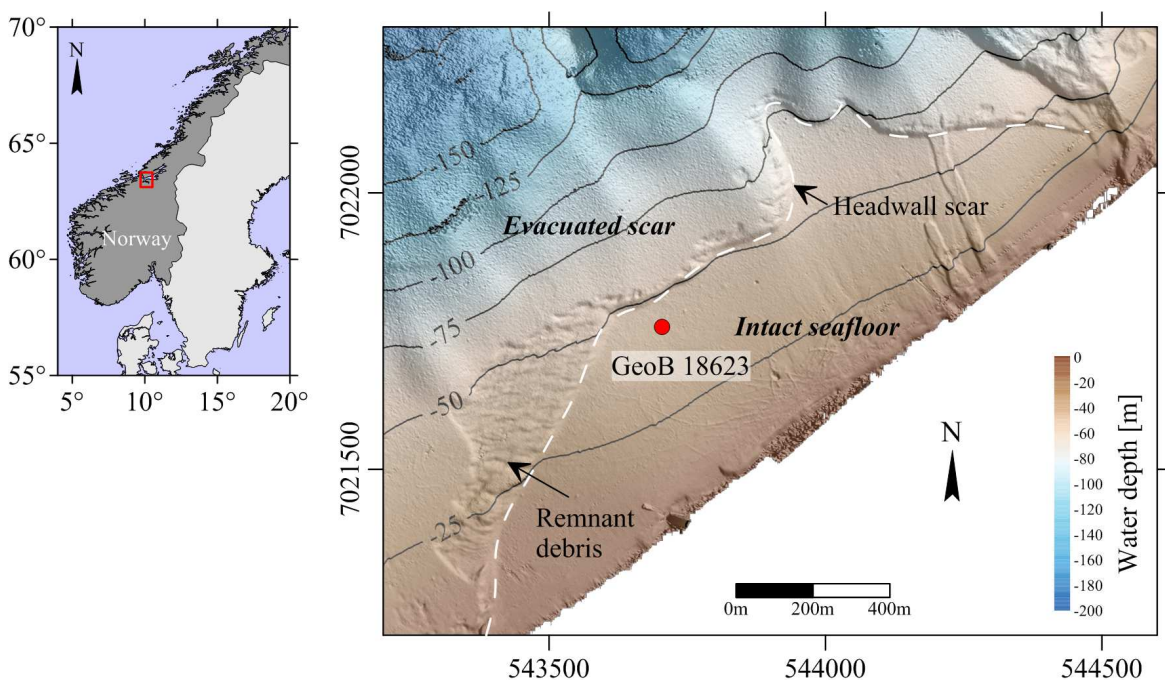


Fig. 3.1 Orkdalsfjord study area (Bathymetry from L'Heureux et al. (2014b) used with courtesy from the Geological survey of Norway, NGU).

## 3.3 Materials and Methods

The study site GeoB18623 is located in 38 m water depth at the intact seafloor above the headwall scar of the 1930 landslide (Fig. 3.1). A static and a vibratory CPTU profile as

well as two up to 4.6 m long gravity cores were retrieved during R/V Poseidon expedition POS472 in 2014. For better comparability the VCPTU depth was correlated with the CPTU profile resulting in maximal vertical offsets of 20 cm. The core GeoB18623-1 was split for sediment description and geotechnical index tests, while GeoB18623-2 was kept closed for subsequent triaxial testing. Undrained shear strength  $s_u$  was determined directly after splitting using vane shear and fall cone test DIN 4094-4:2002-01 (2002). Atterberg limits were measured in every lithology following ASTM D 4318-10 (2010). Grain size distribution was determined every 20 cm with a Beckman Coulter laser diffraction particle size analyser (LS 13320) adopting Udden (1914) and Wentworth (1922) classification.

### 3.3.1 CPTU

The static and vibratory CPTU were conducted using the GOST system (Moon et al., 2013; Steiner et al., 2013; Jorat et al., 2014a). The system uses a 5  $cm^2$  high-resolution piezovibrocone, which measures cone resistance  $q_c$ , sleeve friction  $f_s$  and pore pressure  $u_2$ , which, in static mode, is pushed at a rate of 2  $cm/s$  down to maximal 40  $mbsf$ . As originally developed for static deep sea operations, GOST has a limited hydraulic energy supply restricting penetration speed of vibratory mode to 1.35  $cm/s$ . The CPTU results from cohesive sediments are generally strain-rate dependent and correction procedures for different penetration speeds exist that are also validated for Norwegian fjord sediments (Steiner et al., 2013). The resulting correction for the used setup in  $q_c$  is approximately 3% and was therefore neglected. Vertical laser displacement measurements of the vibratory mode show a steady sinus-shaped cyclic amplitude of 0.38  $mm$  at 4.9  $Hz$  during penetration (Fig. 3.2). Note that the movement of the rod is hydraulically driven from the seafloor and regulated by external displacement sensors. Therefore the actual cyclic movement of the cone may vary with depth.

### 3.3.2 Triaxial Laboratory Testing

Cyclic laboratory experiments were conducted using the MARUM dynamic triaxial testing device (DTTD) (Kreiter et al., 2010b,a). The axial stress is measured inside the cell directly below the soil specimen, whereas the stress control is using an external force sensor. The test specimens have an area of 10  $cm^2$  and a length of 7  $cm$ , following the test procedure of DIN 18137-2:2011-04 (2011). Bulk specimens are tested with undrained isotropically consolidated cyclic single-stress level experiments (e.g. Ishihara, 1985; Singh, 1996). The applied confining pressure of  $\sigma_c = 100$   $kPa$  was higher than the in situ stress conditions to

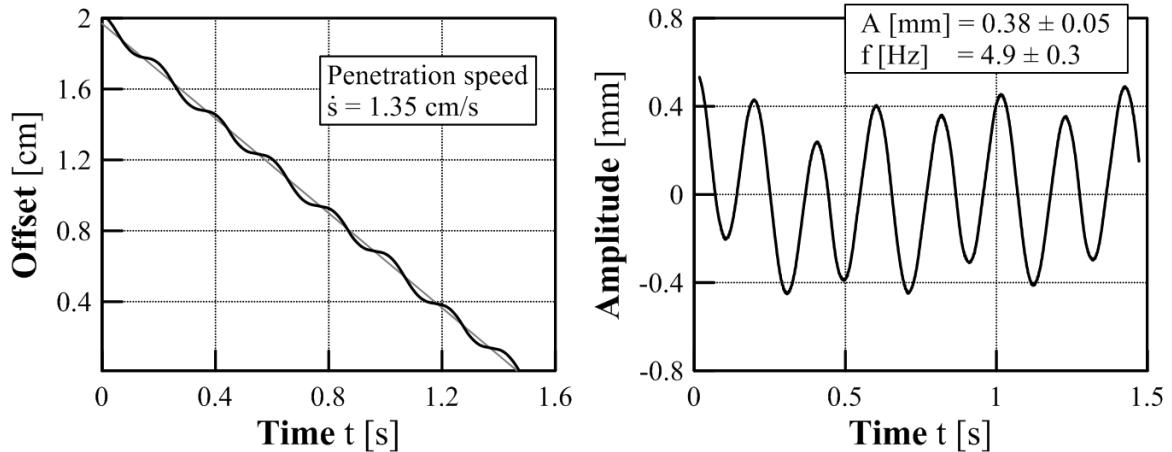


Fig. 3.2 Cyclic signal of VCPTU using GOST.

overcome friction loss at low stress cycles with the external force control. A medium cyclic stress ratio of  $CSR = (\sigma'_1 - \sigma'_3)/2\sigma'_c = 0.1$  at a frequency  $f = 0.5 \text{ Hz}$  was applied.

## 3.4 Results

### 3.4.1 Geotechnical Characterization of Silt Layers

The sediments of gravity core GeoB18623-1 are layered fine to very coarse silt deposits with water contents near the liquid limit  $w_L$  (Fig. 3.3). The sediments have plasticity indices between 12 and 16% and are therefore expected to show clay-like behaviour upon cyclic loading (Boulangier and Idriss, 2006, 2007). Gas escape fractures are common throughout the core indicating a considerable amount of free gas in the in situ fjord sediments. The undrained shear strength from lab vane and fall cone is more or less constant and varies between  $15 \leq s_u \leq 25 \text{ kPa}$ .

Two layers,  $I_1$  and  $I_3$ , consisting of very coarse and coarse silt ( $25 \leq d_{50} \leq 36 \mu\text{m}$ , Fig. 3.4) with high static cone resistances and distinctly lower cyclic cone resistance are detected at depths of 0.55 and 5.5 m, respectively (Fig. 3.3). The decrease in cone resistances is 540 and 340 kPa for layers  $I_1$  and  $I_3$ , respectively. Both silt layers have  $RR$ -values (Eq. 3.1) between 0.5 and 0.7 and are therefore classified to exhibit medium liquefaction potential (Tokimatsu, 1988). This corresponds to cone resistance reductions of 68% and 45%, respectively, which is quite dramatic. In the pore pressure profile intervals with negative  $u$ -values are identified. This extreme pore pressure drop is especially well pronounced in the (very) coarse silt layers  $I_1$  and  $I_3$  during static CPTU, while the pore pressure drop is less for vibratory CPTU.

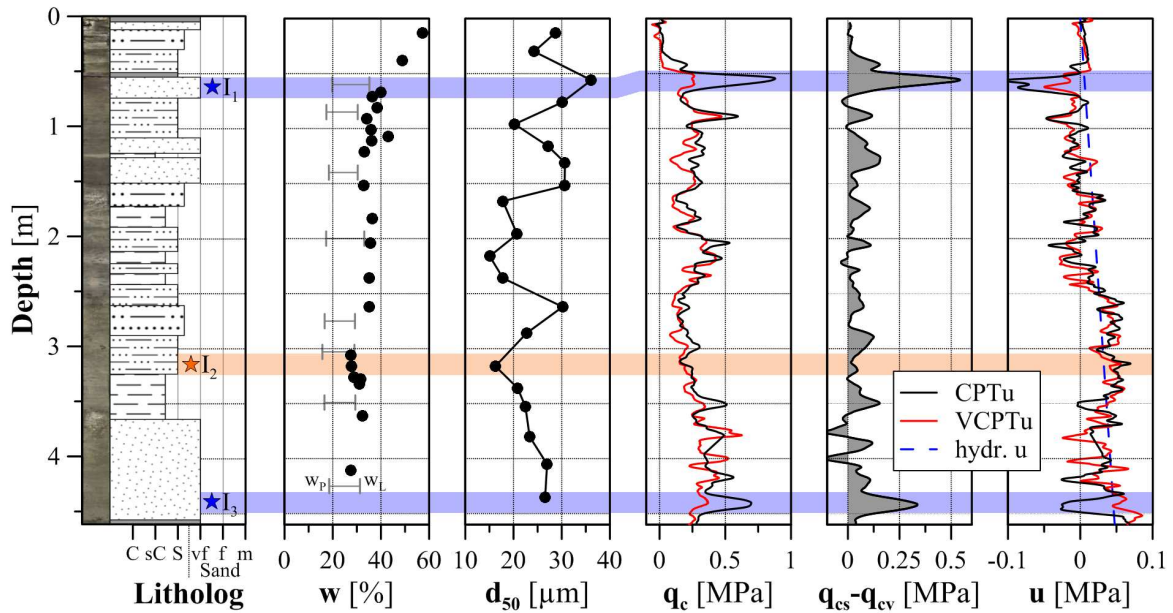


Fig. 3.3 Sediment properties and in situ CPTU at study site GeoB18623. Lithology includes core photos and qualitative grain size description. C: Clay, sC: Clayey silt, S: Silt, vf: very fine sand, f: fine sand, m: medium sand.  $I_1$ – $I_3$ : samples for cyclic triaxial tests, Blue: (Very) coarse silt intervals, Pink: medium-coarse silt interval.

To differentiate the cyclic softening behaviour of the very coarse silt layers with surrounding finer sediments a reference interval  $I_2$  was selected consisting of medium-coarse silt with  $d_{50} = 16 \mu\text{m}$  (Fig. 3.4). In contrast to  $I_1$  and  $I_3$  the reference interval is characterized by low static cone resistance and low  $RR$ -values.

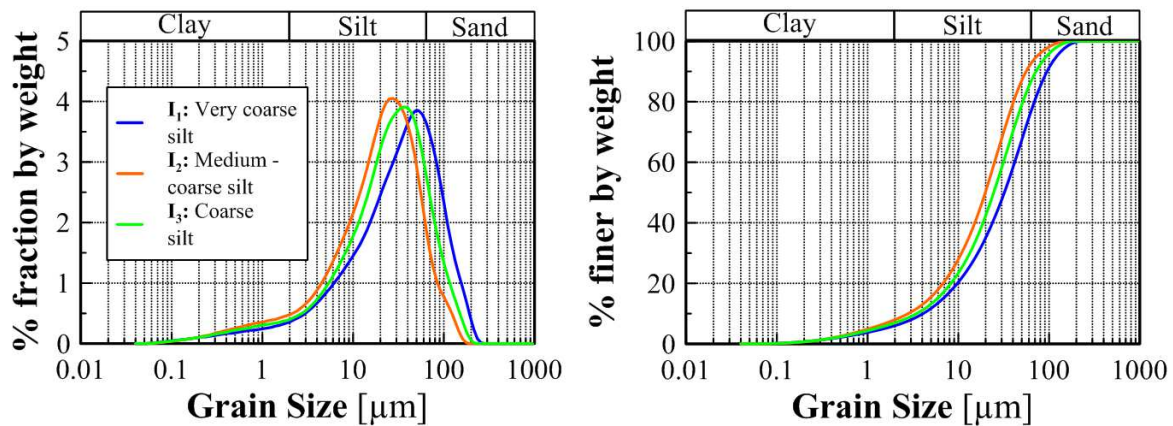


Fig. 3.4 Grain size distribution of samples  $I_1$ ,  $I_2$  and  $I_3$  tested in DTTD.

### 3.4.2 Cyclic Triaxial Response of Silt Layers

In order to evaluate the in situ VCPTU observations, cyclic triaxial tests were conducted on silt layers  $I_1$  and  $I_2$  as their difference in grain size is higher compared to  $I_3$  (Fig. 3.5). The cyclic softening is derived from axial strain  $\epsilon_1$  and normalized excess pore pressure  $u_n = u/\sigma'_c$  at the same number of cycles (Fig. 3.5a, b). The very coarse silt  $I_1$  softens five times faster than the medium coarse silt  $I_2$ . The effective mean pressure  $p'$  is decreasing in both samples with each cycle due to excess pore pressure build-up, however, the initial incremental loss in  $p'$  is larger in  $I_1$  (Fig. 3.5c). In total: The very coarse silt appears to be more vulnerable to cyclic softening than the medium-coarse silt.

## 3.5 Discussion and Conclusion

In this pilot study cyclic geotechnical tests were conducted in situ and under laboratory conditions allowing insight into the cyclic softening behaviour of marine silts from Orkdalsfjord. The very coarse silt layers lose up to 68% cone resistance during VCPTU and exhibit moderate  $RR$ -values of maximal 0.7 making it more vulnerable against cyclic softening compared to surrounding finer silts with  $RR$ -values around zero. This assumption is supported by DTTD tests stating that cyclic softening potential of very coarse silt is significantly higher than the softening potential of the medium coarse silt. The in situ silts generate negative excess pore pressures during CPTU. However, this phenomenon was also observed near Finneidfjord with GOST (Steiner et al., 2013), in the Norwegian Sea and offshore Africa (Lunne, 2012) and in the North Sea (Bayne and Tjelta, 1987) with different CPTU tools. Negative excess pore pressure seems to be characteristic for some cohesive materials with thin interbedded coarser layers. During VCPTU the very coarse silt seems to be less dilative as a response to the cyclically-induced pore water pressures, however the effect may partly be influenced by the difference in penetration speed.

The comparison of VCPTU results with DTTD data is considered with caution as both analyses differ in terms of stress state. VCPTU was conducted in unconsolidated silts subjected to natural anisotropic stress conditions. In DTTD experiments a higher isotropic stress of 100 kPa was used in order to overcome friction loss at low stress cycles. In addition, material properties such as relative density, stress strain history, cementation and the fabric of the soil directly affect the cyclic softening potential (Kramer, 1996). The latter likely varies between the in situ and lab as the lab specimens may have been disturbed through coring, gas escape, transport and preparation. Therefore only a qualitative comparison is possible. A general problem comparing static and vibratory CPTU is the mandatory perfect correlation of the two test sites, in this case the lateral offset is around 3 – 5 m. Imperfect correlation or

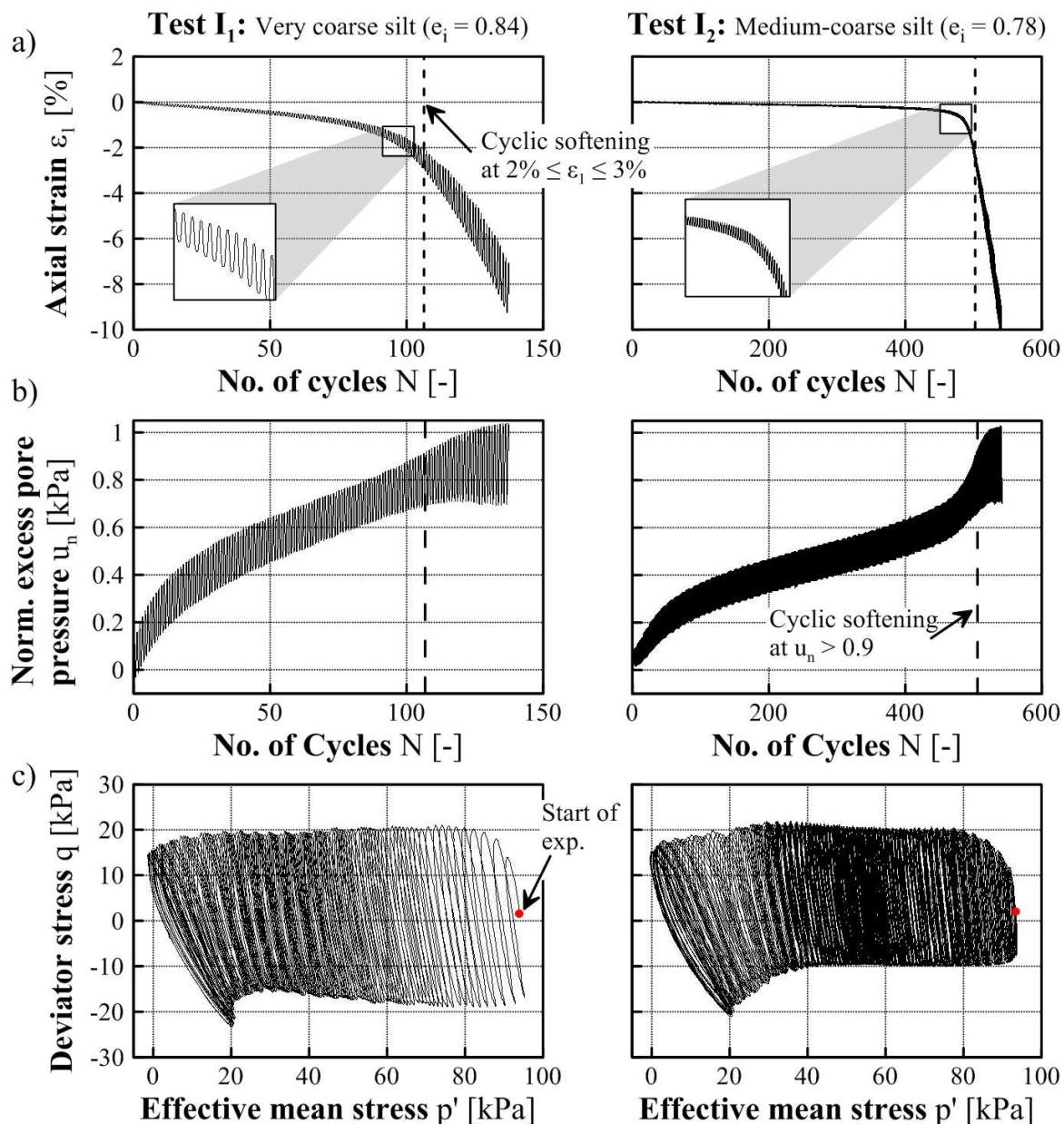


Fig. 3.5 Undrained cyclic triaxial tests on samples  $I_1$  and  $I_2$  with limits for cyclic softening after Kramer (1996) and Boulanger and Idriss (2006). Test conditions:  $\sigma'_c = 100$  kPa,  $CSR = 0.1$ ,  $0.98 \leq B \leq 0.99$ .

lateral variations of the sediment would cause artifacts in the difference of cone resistances and the reduction ratio  $RR$ , however the correlation at GeoB18623 is convincing.

The failure mechanism leading to the 1930 submarine landslide in Orkdalsfjord was comprehensively investigated by L'Heureux et al. (2014b). The authors showed that the slide plane most likely involved a clay-rich layer at 8 – 10 *m* below the original seabed. Results presented in the actual study show that the silt deposits overlying the slide prone layer are vulnerable against cyclic softening and that only small vibrations are necessary to considerably reduce their shear strength. This softening process might have been important in the retrogressive landslide process in order for the landslide debris to completely evacuate the landslide scar.

The present study showed that cyclic softening is a considerable phenomenon in marine silts from Orkdalsfjord and that it might be under certain circumstances an important factor facilitating failure of submarine landslides. We further showed that VCPTU may be a helpful tool to qualitatively characterize in situ cyclic softening potential of marine silts. However, to comprehensively understand the effect of cyclic loading on the soil strength cyclic laboratory tests are indispensable.

## Acknowledgments

The authors acknowledge funding by the Integrated Coastal Zone and Shelf Sea Research Training Group INTERCOAST and the MARUM Centre for Marine Environmental Science at the University of Bremen. The Geological Survey of Norway is gratefully acknowledged for the access to the bathymetric data. We thank Wolfgang Schunn from the University of Bremen who operated GOST and improved data acquisition on board the R/V Poseidon. We thank Nicole Baeten, Alexander Rösner and Robert Roskoden for invaluable assistance during data acquisition and discussion. Marc Huhndorf from the University of Bremen is acknowledged for his efforts regarding laser measurements of the cyclic signal of GOST. We thank both research students David Seibel and Nele Lamping for their sophisticated geotechnical laboratory work. Daniel A. Hepp and Lotta C. Kluger are acknowledged for helpful discussions on the paper. We thank Tom Lunne and Sebastien Garziglia for helpful reviews.

## Author Contributions

M.O. Kluger and S. Kreiter conceived the project. S. Stegmann and T. Mörz acquired funding for ship time and in situ and laboratory experiments. M.O. Kluger designed and led the

experimental program and carried out parts of the in situ and laboratory experiments. S. Kreiter carried out parts of the in situ experiments. T. Mörz, S. Stegmann, and V.G. Moon supervised this project. M.O. Kluger did the data evaluation, created figures, wrote the first manuscript version, and led the revision process. S. Kreiter and J.-S. L'Heureux contributed to discussion and revised the manuscript. T. Mörz, S. Stegmann, and V.G. Moon commented on the final manuscript. All authors approved the final manuscript.

# Chapter 4

## Undrained cyclic shear behaviour of altered tephra

**Max O. Kluger<sup>1</sup>, Stefan Kreiter<sup>1</sup>, Vicki G. Moon<sup>2</sup>, Rolando P. Orense<sup>3</sup>  
Philippa Mills<sup>4</sup>, and Tobias Mörz<sup>1</sup>**

<sup>1</sup>MARUM–Center for Marine Environmental Sciences, University of Bremen, Leobener Straße, 28359 Bremen, Germany

<sup>2</sup>School of Science, University of Waikato, Private Bag 3105, Hamilton 3240, New Zealand

<sup>3</sup>Department of Civil & Environmental Engineering, University of Auckland, Auckland, New Zealand

<sup>4</sup>Coffey Geotechnics, Level 11, 7 City Road, Auckland 1010, New Zealand

Submitted to *Géotechnique*, 31th of March, 2017, Since July 25th under revision with major revisions required

### Abstract

Altered tephra are volcanic airfall materials that have been subjected to various soil processes and are prevalent across volcanic islands like the North Island of New Zealand. Understanding their undrained response to cyclic loading is essential for geotechnical engineering applications in these regions because of frequently occurring local earthquakes. We describe for the first time the cyclic undrained behaviour of an altered, clay-rich and highly sensitive tephra through triaxial tests. The altered tephra experiences brittle failure and has higher friction coefficients than normally consolidated clay, being comparable to sand or unaltered

tephra. Comparison of cyclic contour diagrams covering the whole compressional and extensional range of testing conditions with those previously developed for marine clays shows that for altered tephra: (1) the number of loading cycles to failure depends more strongly on the average shear stress; (2) the material is more resistant to small cyclic loading but fails within a narrower range of shear stresses; and (3) cyclic shear strength peaks at zero average shear stress, in contrast to marine clays where cyclic shear strength peaks at small compressive average stress.

**Keywords** Shear strength · Clays · Residual soil · Laboratory tests · Deformation · Earthquakes · Friction

## 4.1 Introduction

Subsoils along the coast are often exposed to cyclic loading from earthquakes, wind, waves and traffic, affecting serviceability and ultimate capacity of engineering structures. During cyclic loading, soils may experience a variety of stress conditions, which can lead to shear deformation, pore fluid pressure increase, and eventually shear failure. The effects of cyclic loading are strongest in undrained conditions. Therefore, geotechnical design relies on precise knowledge of the soil's undrained response to different average and cyclic shear stresses. Most previous studies on cyclic undrained behaviour of soils have focussed on sand (Mohamad and Dobry, 1986; Alarcon-Guzman et al., 1988; Hyodo et al., 1994a), clay (Sangrey et al., 1969; Ansal and Erken, 1989; Yasuhara et al., 1992), or silt-clay mixtures (Hyde and Brown, 1976; Guo and Prakash, 1999), while knowledge of the cyclic shear strength of volcanic soils is limited to crushable unaltered tephra (Miura et al., 2003; Orense and Pender, 2015; Wiemer and Kopf, 2016).

Tephra is unlithified volcanic airfall material of any grain size and composition (Lowe, 2011) and is widely deposited in tectonically active areas such as New Zealand and Japan (Briggs et al., 2005; Chigira, 2014), where it is a relevant subsoil for geotechnical design. Volcanic glass is a major constituent of tephra, which alters to secondary clay minerals within several thousands of years (Lowe, 1986). This alteration changes the shear strength and deformation characteristics of the tephra. Although the alteration process will most likely affect the bearing capacity of foundations and the stability of natural slopes under cyclic loading, no attention has yet been paid to the cyclic loading behaviour of altered tephra. Granular soil is known to liquefy as a consequence of excess pore water pressure, while clays commonly exhibit cyclic softening (Boulanger and Idriss, 2006; Idriss and Boulanger,

2008). It remains unknown whether altered tephra exhibits undrained cyclic shear strength properties similar to granular soil such as sand and unaltered tephra or clay.

This paper describes the cyclic undrained behaviour of the *Pahoia Tephra*, widely deposited during the Quaternary on the North Island of New Zealand (Briggs et al., 2005), and which has since been subsequently altered to secondary clay minerals (Moon et al., 2015b; Kluger et al., 2017). Thin-walled push tube samples were recovered from a highly sensitive Pahoia Tephra interval above the assumed failure surface of the well-studied Omokoroa flow slide (Smalley et al., 1980; Kluger et al., 2017). The samples were analysed in a program of monotonic and cyclic triaxial tests to quantify the effect of cyclic and average shear stresses on shear strain development and cyclic shear strength. Using our data, we constructed contour diagrams of cyclic loading failure, initially developed to analyse the cyclic undrained behaviour of marine Norwegian clay, for altered tephra (Andersen and Lauritzen, 1988; Wichtmann et al., 2013; Andersen, 2015).

## 4.2 Sample material and testing procedure

### 4.2.1 Pahoia Tephra

#### Sampling

The Omokoroa flow slide is located in the Tauranga Harbour, at the eastern coast of the North Island of New Zealand (37.63°S, 176.05°E). The subsoil in this region between around 10 *m* and 25 *m* depth is the Pahoia Tephra, which is therefore of engineering significance. The main failure surface of the Omokoroa flow slide is assumed to be located at approximately 23 *m* depth within this unit (Kluger et al., 2017).

In the present study, 18 thin-walled push tube samples with 36 *mm* internal diameter were recovered from a horizontal trench that we have dug into the Omokoroa flow slide headwall 19 *m* below the pre-slide ground level. This sampling location was chosen because it was possible to correlate this unit using a distinctive iron-manganese layer, 0.5 *m* above the trench, with a nearby drill core, *Omok-1* (Fig. 4.1(a)). The trench was dug approximately 1.5 *m* behind the currently exposed face to avoid seasonal drying effects. The sampled material is an altered tephra with intact texture and no macroscopic cracks visible. The sampling tubes were subsequently pushed vertically into the trench at a horizontal spacing of at least 10 *cm*. After sampling, the push tube samples were sealed in air tight containers, wrapped in foam, and shipped for triaxial testing.

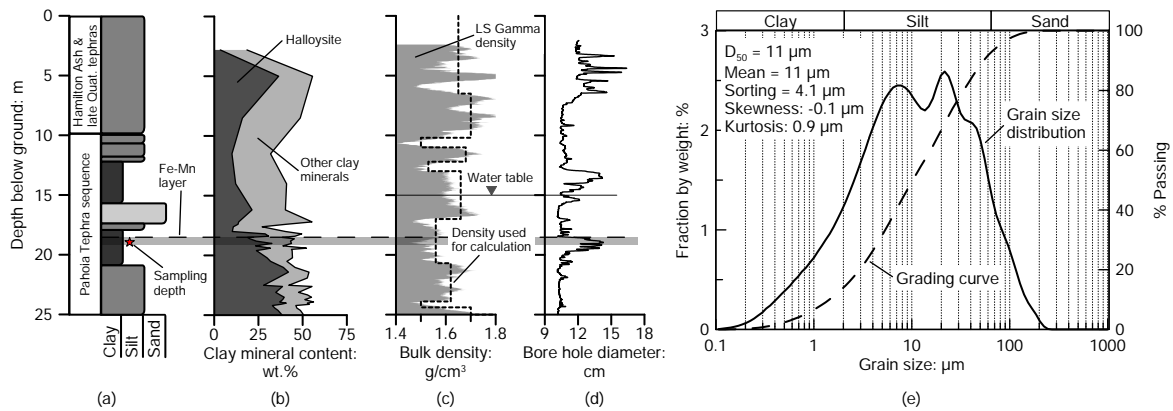


Fig. 4.1 (a-b) Sediment description and cumulative clay mineral content of core Omok-1 (Kluger et al., 2017); (c-d) Results from bore hole logging of Omok-1; (e) Grain size distribution of Pahoia Tephra, sampling depth 19 m.

Table 4.1 Physical and mechanical properties of the Pahoia Tephra.

Clay mineral content	46 wt. %
- Halloysite *	34 wt. %
- Kaolinite	7 wt. %
- Illite, Mica	3 wt. %
- Montmorillonite	2 wt. %
Amorphous constituents	28 wt. %
Mean grain size	11 μm
Fines content (< 63 μm)	92 wt. %
Natural water content, $w$	81% ± 3%
Liquid limit, $w_L$	66%
Plasticity index, $I_P$	25
Activity	0.4
Sensitivity (field vane)	11
Sensitivity (laboratory vane) *	10
Coefficient of earth pressure at rest, $K_0$ * <sup>1</sup>	0.57
Effective overburden pressure, $\sigma'_{ac}$	257 kPa

\* Kluger et al. (2017)

\*<sup>1</sup> Brooker and Ireland (1965)

### Sample properties

The Pahoia Tephra sequence has a clay mineral concentration of 30 % to 60 % (Fig. 4.1(b)), based on X-ray diffraction measurements of bulk samples along core Omok-1 following procedures outlined in Kluger et al. (2017). The Pahoia Tephra sample at 19 m depth (Tab. 4.1) has a clay mineral content of 46 %, with halloysite being the dominant mineral (Kluger et al., 2017). Minor phyllosilicate mineral phases include kaolinite, illite, mica, and montmorillonite. The high amount of amorphous constituents, mostly volcanic glass, indicates that parts of the primary constituents have not yet been altered and are still present in the residual soil.

Grain size distribution was determined with a Beckman Coulter Laser diffraction particle size analyser LS 13320 following McGregor et al. (2009). The Pahoia Tephra has a high fines content of 92 %, and is classified as a bimodal, very poorly sorted medium silt according to Folk and Ward (1957) (Tab. 4.1, Fig. 4.1(e)). Moisture content and Atterberg limits were obtained following NZS 4402.4.1.1:1986 (1986). The Pahoia Tephra sample plots well below the A-line of the Casagrande plasticity chart and is therefore classified as inactive, medium plastic, inorganic silt of high compressibility (Casagrande, 1932; Skempton, 1953). The Pahoia Tephra is highly sensitive based on field and laboratory vane shear experiments (NZGS, 2001; DIN 4094-4:2002-01, 2002; Norsk Geoteknisk Forening, 1974).

### 4.2.2 Triaxial testing

The cyclic undrained behaviour of the Pahoia Tephra was analysed through two monotonic and 16 cyclic undrained shear tests controlled with an internal stress sensor, using the MARUM Dynamic Triaxial Testing Device (DTTD) (Kreiter et al., 2010b). Our samples were 36 mm in diameter and approximately 80 mm in height, which were carefully extracted from the push tubes, mounted into the triaxial apparatus, and vacuum saturated with deionized and deaerated water.

### Consolidation

For constructing cyclic contour plots, Andersen and Lauritzen (1988) recommend to consolidate the sample to in situ stress and to use a stress path that avoids swelling of the sample as discussed by Hight et al. (1992). The in situ effective vertical stress before failure at 19 m depth was derived from in situ LS gamma density logging and piezometric measurements in borehole Omok-1 (Fig. 4.1(c-d)). The earth pressure at rest  $K_0$  was estimated using the plasticity index correlation of Brooker and Ireland (1965), which is commonly used for cohesive soils (Wichtmann et al., 2013). This yields an axial consolidation stress of

$\sigma'_{ac} = 267 \text{ kPa}$ , a  $K_0 = 0.57$  and an effective radial stress of  $\sigma'_r = 152 \text{ kPa}$  as initial condition for all tests.

The sample was first isotropically re-consolidated to the radial stress and rested for 2 h. Afterwards the axial stress was increased until the in situ axial consolidation stress was established. The maximum consolidation shear stress at a  $45^\circ$  plane is  $\tau_c = (\sigma'_{ac} - \sigma'_r)/2 = 57.5 \text{ kPa}$ . A saturation pressure of  $\Delta u = 400 \text{ kPa}$  was sufficient to attain a Skempton' B-value of  $\geq 0.95$ . All samples were held under constant anisotropic consolidation stresses for at least 12 h. The disturbance of the samples was quantified by the change in void ratio  $\Delta e/e_0$  during consolidation, where  $e_0$  is the initial void ratio before consolidation and  $\Delta e$  is the difference in void ratios measured before and after consolidation. All samples exhibited changes in void ratios of  $\Delta e/e_0 \leq 0.04$  (Tabs. 4.2 and 4.3), which corresponds to a sample quality of "very good to excellent" for normally consolidated clays (Lunne et al., 2006).

### Triaxial testing procedure

Two monotonic undrained tests were performed in accordance with DIN 18137-2:2011-04 (2011) to derive the compressional  $s_u^C$  and extensional  $s_u^E$  undrained shear strengths of the Pahoia Tephra (Tab. 4.2). Both parameters are needed to construct the cyclic contour diagram (Andersen and Lauritzen, 1988), in which the average  $\tau_{av}$  and cyclic  $\tau_{cy}$  shear stresses are normalized by the compressional undrained shear strength.  $\tau_{av}$  is defined here as the average undrained shear stress acting on the soil during cyclic loading, while  $\tau_{cy}$  is the single-amplitude shear stress caused by cyclic loads (Fig. 4.2). Note that compressional stress and strain are considered positive and extensional stress and strain are considered negative.

Six series of undrained cyclic tests were performed; in each series the cyclic shear stress ratio was varied at a constant average shear stress (Tab. 4.3). The test series vary in average shear stress ratio, spanning the whole stress range from extensional to compressional undrained shear strength. For each test series, the average and cyclic shear stresses were chosen with the aim to reach failure between 1 and 1000 loading cycles, using the published data from marine clays (Andersen, 2015). The change in average shear stress from the consolidation shear stress was applied undrained by changing the axial total stress  $\sigma_a$  at a constant rate of  $0.1 \text{ kPa/s}$ . After the average shear stress was applied, the sample was allowed to rest undrained for approximately 2 h. The initial shear strain  $\gamma_i$  that develops due to this initial loading is depicted in Fig. 4.2. Shear strain  $\gamma$  has been taken as 1.5 times the axial strain  $\epsilon_a$  assuming that  $\gamma/2 = (\epsilon_a - \epsilon_r)/2$  and  $\epsilon_r = -\epsilon_a/2$ , where  $\epsilon_r$  is the radial strain (Terzaghi et al., 1996). Cyclic sinusoidal loading was applied in stress control with a frequency of  $f = 0.1 \text{ Hz}$ .

Table 4.2 Specifications of monotonic triaxial tests.

Test No.	Movement	$w$ %	$\Delta e_c/e_0$	$\dot{s}$ mm/min	$\sigma'_{ac}$ kPa	$\sigma'_{rc}$ kPa	$\tau_c$ kPa	$s_u$ kPa	$c'$ kPa	$\phi'$ °
<sup>1</sup> CIU-1	Compr.	72 *	n. d.	0.5	205	205	0	133	11 *	35 *
<sup>1</sup> CIU-2	Compr.	72 *	n. d.	0.5	275	275	0	162	11 *	35 *
<sup>1</sup> CIU-3	Compr.	72 *	n. d.	0.5	355	355	0	192	11 *	35 *
<sup>2</sup> CAU-1	Compr.	80	0.02	0.05	267	152	57.5	120		
<sup>2</sup> CAU-2	Ext.	79	0.04	0.05	267	152	57.5	-80		

<sup>1</sup> Isotropically consolidated undrained tests performed by Mills and Moon (2016)

<sup>2</sup> Anisotropically consolidated undrained tests performed in the present study

\* Average values

Compr., compression

Ext., extension

n. d., not determined

Table 4.3 Specifications of cyclic triaxial tests.

Test series	Test No.	$w$ %	$\Delta e_c/e_0$	$f$ Hz	$\tau_{av}$ kPa	$\tau_{av}/s_u^C$	$\tau_{cy}$ kPa	$\tau_{cy}/s_u^C$	$N$
1	CY-15	81	0.02	0.1	-30	-0.25	48	0.4	238
	CY-16	79	0.02	0.1	-30	-0.25	60	0.5	80
	CY-21	80	0.03	0.1	-30	-0.25	72	0.6	3
2	CY-13	83	0.03	0.1	0	0	72	0.6	214
	CY-14	80	0.02	0.1	0	0	84	0.7	59
	CY-17	80	0.03	0.1	0	0	96	0.8	2
3	CY-24	83	0.02	0.1	15	0.125	72	0.6	68
4	CY-19	81	0.02	0.1	30	0.25	48	0.4	> 9743 *
	CY-22	84	0.02	0.1	30	0.25	60	0.5	54
	CY-12	87	0.03	0.1	30	0.25	72	0.6	31
	CY-20	80	0.03	0.1	30	0.25	84	0.7	7
5	CY-8	88	0.02	0.1	57.5	0.48	36	0.3	> 7094 *
	CY-9	82	0.02	0.1	57.5	0.48	48	0.4	1896
	CY-6	75	0.03	0.1	57.5	0.48	60	0.5	7
6	CY-10	80	0.02	0.1	90	0.75	24	0.2	373
	CY-11	82	0.03	0.1	90	0.75	36	0.3	15

Negative shear stress indicates triaxial extension direction

\* No failure achieved

All tests:  $h/d = 2.5 \pm 0.1$ ; B-value = 95%;  $\sigma'_{ac} = 267$  kPa;  $\sigma'_{rc} = 152$  kPa

The pore water pressure development in cohesive soils measured in the triaxial apparatus is strongly strain rate dependent and the relatively high frequency used in the present study may result in uneven distribution of pore water pressure within the sample (Zergoun and Vaid, 1994). Therefore, pore water pressure is not an appropriate failure criterion. Alternatively, shear strain has been used as parameter to quantify the undrained shear failure in clay (Andersen, 2015). In cyclic tests presented in this study failure is defined as the attainment of either 15 % average shear strain  $\gamma_{av}$  or 15 % cyclic shear strain  $\gamma_{cy}$  (Fig. 4.2).

In all triaxial tests, the axial total stress was corrected for the increase of the sample cross section and the stress supported by the rubber membrane according to ASTM D 4767-04 (2004) and DIN 18137-2:2011-04 (2011).

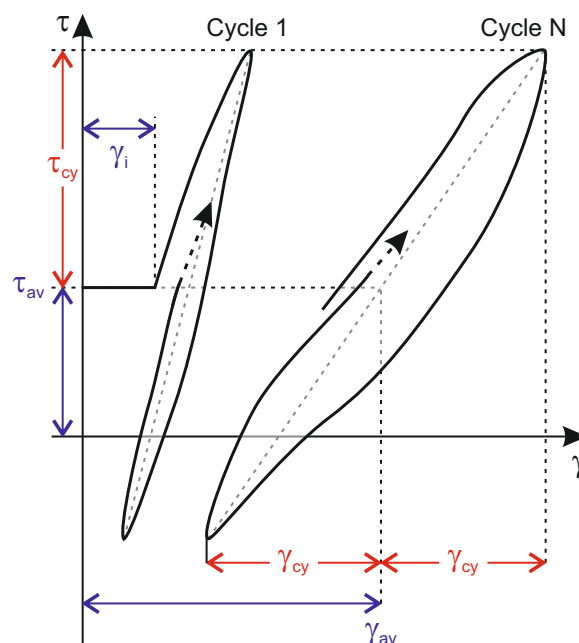


Fig. 4.2 Definition of shear stress, shear strain, and shear modulus (Modified from Andersen, 2009).

### 4.3 Static undrained shear strength of altered tephra

The monotonic undrained shear behaviour of the Pahoia Tephra was analysed using a compilation of the two anisotropically consolidated tests from the present study and three isotropically consolidated tests performed by Mills and Moon (2016). The isotropically consolidated triaxial tests were performed on thin-walled tube samples obtained from the same depth as in the present study, but tested with both larger sample size and higher shear rate (Tab. 4.2).

All samples tested under undrained compression failed at axial strains of  $\varepsilon_a \approx 3\%$  and exhibited strain softening after failure (Fig. 4.3(a)), which is typical for brittle failure in sensitive post-glacial clay (Gylland, 2014). The anisotropically consolidated sample CAU-1 was tested under considerably higher consolidation stress than the isotropically consolidated sample CIU-1. However, both samples exhibit similar undrained shear strengths. The comparatively higher undrained shear strength observed under isotropic consolidation is possibly a result of the higher shear rate that was applied in the isotropic consolidated compression tests. This finding is similar to the behaviour of normally consolidated clays (Lefebvre and Leboeuf, 1987; Zergoun and Vaid, 1994), where a lowering of undrained shear strength was attributed to a larger pore water pressure increase at higher shear rates.

The effective stress paths in isotropically and anisotropically consolidated compression tests exhibit contractive behaviour and define approximately the same failure envelope (Fig. 4.3(b)). The mean effective stress is defined as  $s' = (\sigma'_a + \sigma'_r)/2$ . Isotropically consolidated tests commonly exceeded the failure envelope when reaching their undrained shear strength, likely as a result of the higher shear rate applied. After this, all stress paths of the compression tests follow the same failure envelope. In contrast to the undrained shear strength, the failure envelope of the Pahoia Tephra is largely shear rate independent, which is in agreement with undrained failure envelopes observed in sensitive normally consolidated clays (Lefebvre and Leboeuf, 1987). This suggests that the pore water pressure during strain softening is not affected by the shear rate.

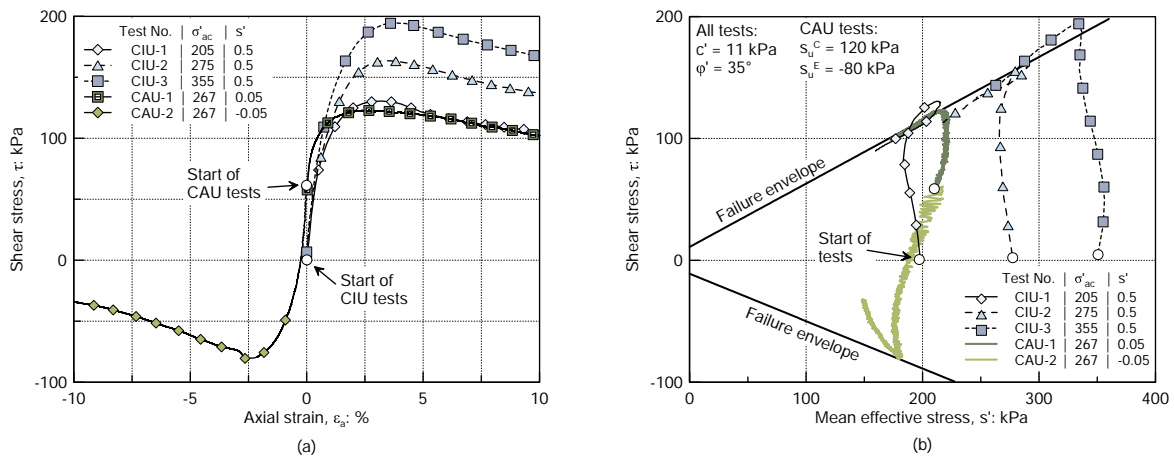


Fig. 4.3 (a) Shear stress – shear strain and (b) shear stress – mean effective stress relationships for the Pahoia Tephra, compiled from monotonic undrained compression and extension tests from the present study and from Mills and Moon (2016).

The effective stress path of the monotonic extension test CAU-2 did not follow the failure envelope after reaching the extensional undrained shear strength (Fig. 4.3(b)). This

observation indicates that the Pahoia Tephra exhibits a less contractive undrained behaviour during extension than during monotonic compression, which is explained by a smaller increase in pore pressure, hence a smaller reduction in mean effective stress in the strain softening regime. No comparable material behaviours for other soils have been described in the literature.

From the undrained compression tests, an effective cohesion of  $c' = 11 \text{ kPa}$  and a critical friction angle of  $\phi'_{crit} = 35^\circ$  were derived (Tab. 4.2 and Fig. 4.3(b)). The critical friction angle of the Pahoia Tephra is comparable to that of sand but significantly larger than that of normally consolidated clay. The critical friction angle obtained for 20 different quartz sands is  $\phi'_{crit} = 33^\circ \pm 2^\circ$  (Mohamad and Dobry, 1986; Wiemer and Kopf, 2016; Bolton, 1986), while for a large number of normally consolidated clays the average value was found to be  $\phi'_{crit} = 28^\circ \pm 6^\circ$  (Diaz-Rodriguez et al., 1992). Because volcanic soils have highly variable mineral composition, the critical friction angle for unaltered tephra is more diverse than those measured on normally consolidated clays. Wiemer and Kopf (2016) studied the direct shear behaviour of different marine and terrestrial unaltered tephtras and observed  $\phi'_{crit}$  ranging from  $33^\circ$  to  $36^\circ$ , while Orense and Pender (2015) found even higher values of  $42^\circ$  to  $44^\circ$  for different pumice sands. Our results show that the altered Pahoia Tephra exhibits frictional behaviour comparable to unaltered volcanic soils.

#### 4.4 Cyclic undrained shear behaviour of altered tephra

During cyclic loading, the soil may be subjected to different average shear stresses, which can vary within the range of compressional and extensional undrained shear strength. Therefore, the influence of average shear stress on the shear strain behaviour of the Pahoia Tephra was studied by comparing scenarios, ranging from extensional stress conditions of  $\tau_{av}/s_u^C = -0.25$  to high compressional stress conditions of  $\tau_{av}/s_u^C = 0.75$  (Figs. 4.4 and 4.5).

The average shear stress controls the shear strain failure mode of the Pahoia Tephra (Fig. 4.4). For all average shear stress ratios applied, an increase in both  $\gamma_{av}$  and  $\gamma_{cy}$  were observed during each test, eventually leading to failure once a given number of loading cycles was reached. In the cases where failure occurred, samples commonly developed a distinctive shear band during a single loading cycle, which was accompanied by a rapid increase in shear strain. This abrupt reduction in strength upon cyclic loading is in accordance with the strain softening and brittle failure observed for the Pahoia Tephra during monotonic compression tests.

Samples tested in the triaxial extensional regime (Test series No. 1 and 2) exhibited a negative average shear strain development until an extensional failure occurred at  $\gamma_{av} =$

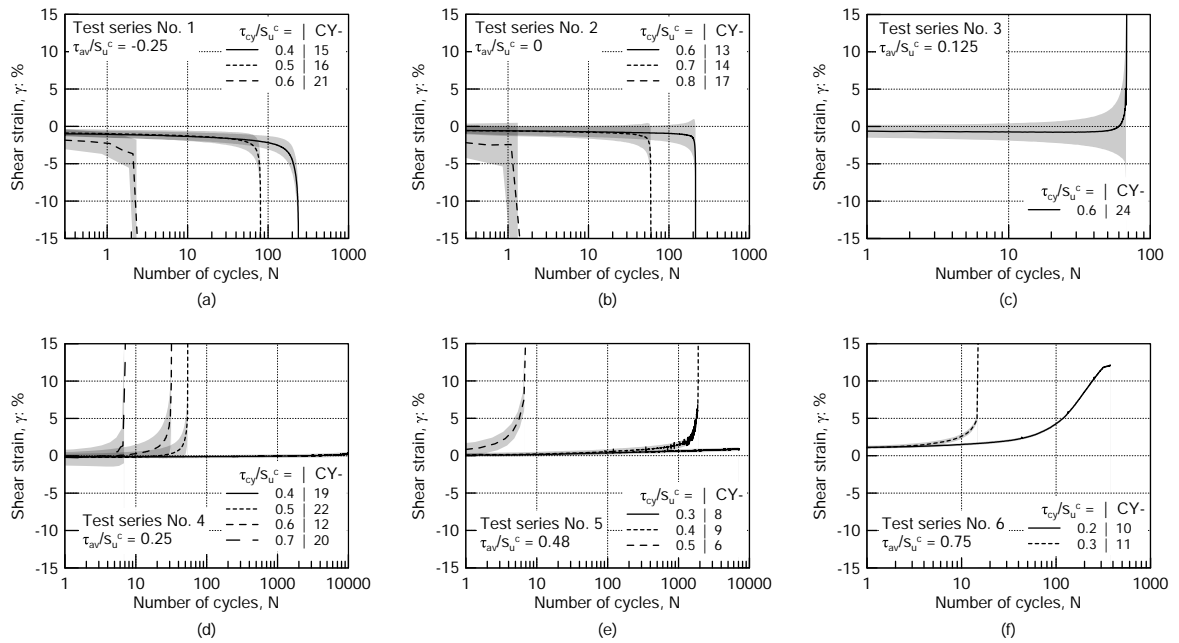


Fig. 4.4 Shear strain response of Pahoia Tephra to undrained loading cycles. Average and cyclic shear strain components are represented by lines and grey shaded areas, respectively.

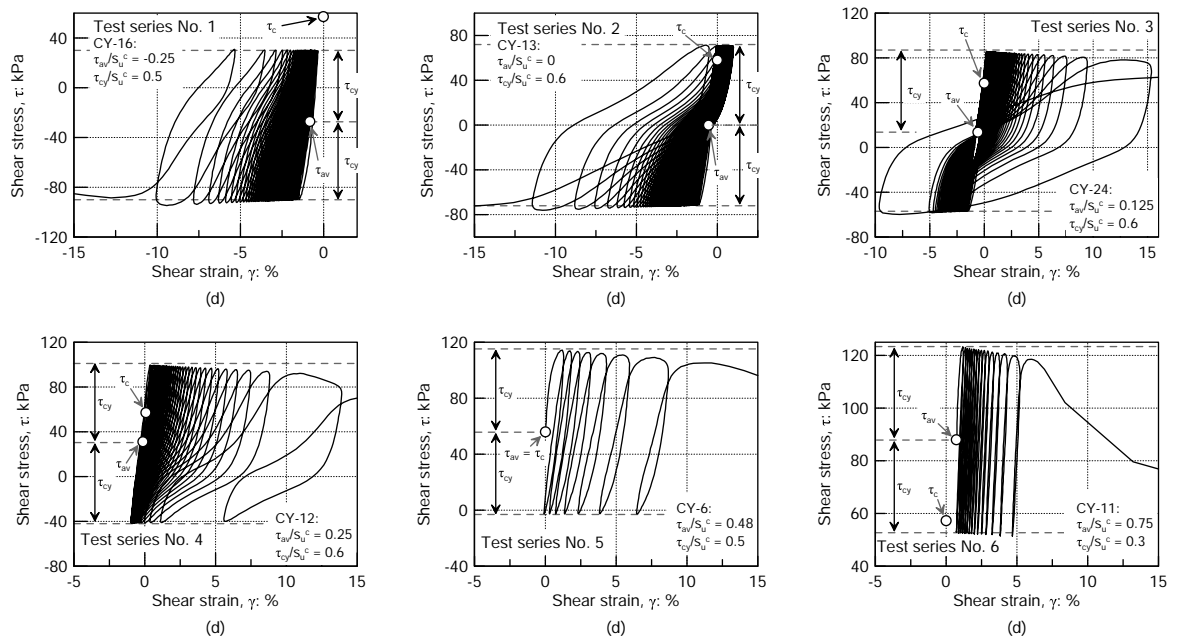


Fig. 4.5 Shear stress – shear strain relationship for the Pahoia Tephra under different average shear stress.

–15%. At negative average shear stress ratios of  $\tau_{av}/s_u^C = -0.25$  (Figs. 4.4(a) and 4.5(a)), the samples developed non-recoverable negative shear strains, being the result of pronounced increases in negative average shear strain. At isotropic stress conditions of  $\tau_{av}/s_u^C = 0$  (Figs. 4.4(b) and 4.5(b)), the cyclic shear strain was larger and a small proportion of negative shear strain was recovered during each loading cycle. At low numbers of loading cycles, this led to symmetrical shear stress - shear strain hysteresis loops. During the last loading cycles, however, the hysteresis loops became asymmetrical with a larger proportion in the extensional regime. This asymmetric shear strain response to symmetric cyclic loading observed for the Pahoia Tephra is similar to the cyclic undrained behaviour of clays, where asymmetric shear strain response is associated with stress reversal (Hyodo et al., 1994b).

In test CY-24 with a low average shear stress ratio of  $\tau_{av}/s_u^C = 0.125$  (Figs. 4.4(c) and 4.5(c)), the sample developed nearly symmetrical shear stress - shear strain hysteresis loops with only minor accumulation of average shear strain. All other samples tested in the triaxial compressional regime (Test series No. 4 - 6) with average shear stress ratio between  $0.25 \leq \tau_{av}/s_u^C \leq 0.75$ , developed positive non-recoverable shear strain until a compressional failure was reached at  $\gamma_{av} = 15\%$ . At moderate average shear stress of  $\tau_{av}/s_u^C = 0.25$  (Figs. 4.4(d) and 4.5(d)), samples still experienced stress reversal, and partly symmetrical shear stress - shear strain hysteresis loops developed. The samples CY-6 and CY-11, tested at average shear stress ratios  $\tau_{av}/s_u^C$  of 0.48 and 0.75, respectively (Figs. 4.4(e, f) and 4.5(e, f)), did not experience stress reversal and developed non-recoverable strain and increasingly asymmetrical hysteresis loops.

The number of loading cycles to failure as a function of average and cyclic shear stress ratios was approximated with a power law (Seed and Idriss, 1971) as:

$$\tau_{av}/s_u^C = a \cdot N^{-b} \quad (4.1)$$

where the parameters  $a$  and  $b$  are determined by numerical fits to the experimental data (Fig. 4.6). Note that for test series 3, which is based on only one test, the power law function was fitted by manually changing the parameters  $a$  and  $b$  obtained for test series 4, until a parallel fit to the other data was reached. The average shear stress strongly affects the number of cycles to failure. Samples tested at the same cyclic shear stress but with higher average shear stress ratios exhibit significantly lower number of cycles to failure. For example, samples CY-8 and CY-11 were tested at the same cyclic shear stress, but with average shear stress ratios  $\tau_{av}/s_u^C$  of 0.48 and 0.75, respectively, illustrated by grey arrow in Fig. 4.6. While the sample CY-8, tested at lower average shear stress, did not achieve failure after more than 7,000 loading cycles, at higher average shear stress, sample CY-11 failed after 15 loading cycles. Wichtmann et al. (2013) also observed a decrease in the number of loading cycles

to failure as a function of increasing average shear stress during cyclic triaxial testing of normally consolidated Onsøy Clay. However, this decrease in number of loading cycles to failure was less pronounced than our observations of the Pahoia Tephra, which is therefore more vulnerable to the average shear stress than Onsøy Clay.

The influence of cyclic shear stress on the undrained behaviour of the Pahoia Tephra is illustrated by the slope of the lines fitted to the test series with constant average shear stress (Fig. 4.6). As expected, the number of cycles to failure increases with decreasing cyclic shear stress ratio for all average shear stress ratios considered. Most power law functions in Fig. 4.6 exhibit similar curvature, which indicates that the vulnerability to cyclic shear stress ratio is not dependent on the average shear stress. The only exception is test series 5 at in situ average shear stress. Compared to the other test series, the power law function fit to the test series 5 data exhibits a significantly lower curvature. Accordingly, for in situ average shear stress, the Pahoia Tephra is more vulnerable to an increase in cyclic shear stress compared to other average shear stress ratios.

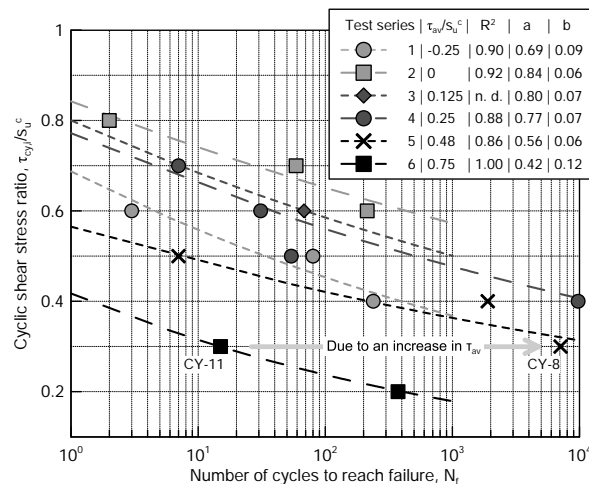


Fig. 4.6 Cyclic shear stress ratios to reach failure in a specific number of loading cycles for different average shear stress ratios.

## 4.5 Cyclic shear strength of altered tephra

We utilized the concept of cyclic shear strength contour diagrams, as proposed by Andersen and Lauritzsen (1988), to comprehensively analyse the cyclic undrained behaviour of the Pahoia Tephra. All test results for different combinations of average and cyclic shear stress ratios are displayed in the average shear stress ratio vs. cyclic shear stress ratio plane of Fig. 4.7(a). Solid contour lines represent average and cyclic shear stress ratios required

for failure after  $N_f = 1, 10, 100,$  and  $1000$  loading cycles, in the following also described as cyclic shear strength, and were derived from Eq. 4.1. All  $N_f$  – contour lines intersect with the horizontal axis at two points, at which the contribution of cyclic shear stress is zero. These points represent the undrained shear strength of the soil, obtained from the monotonic compression and extension tests.

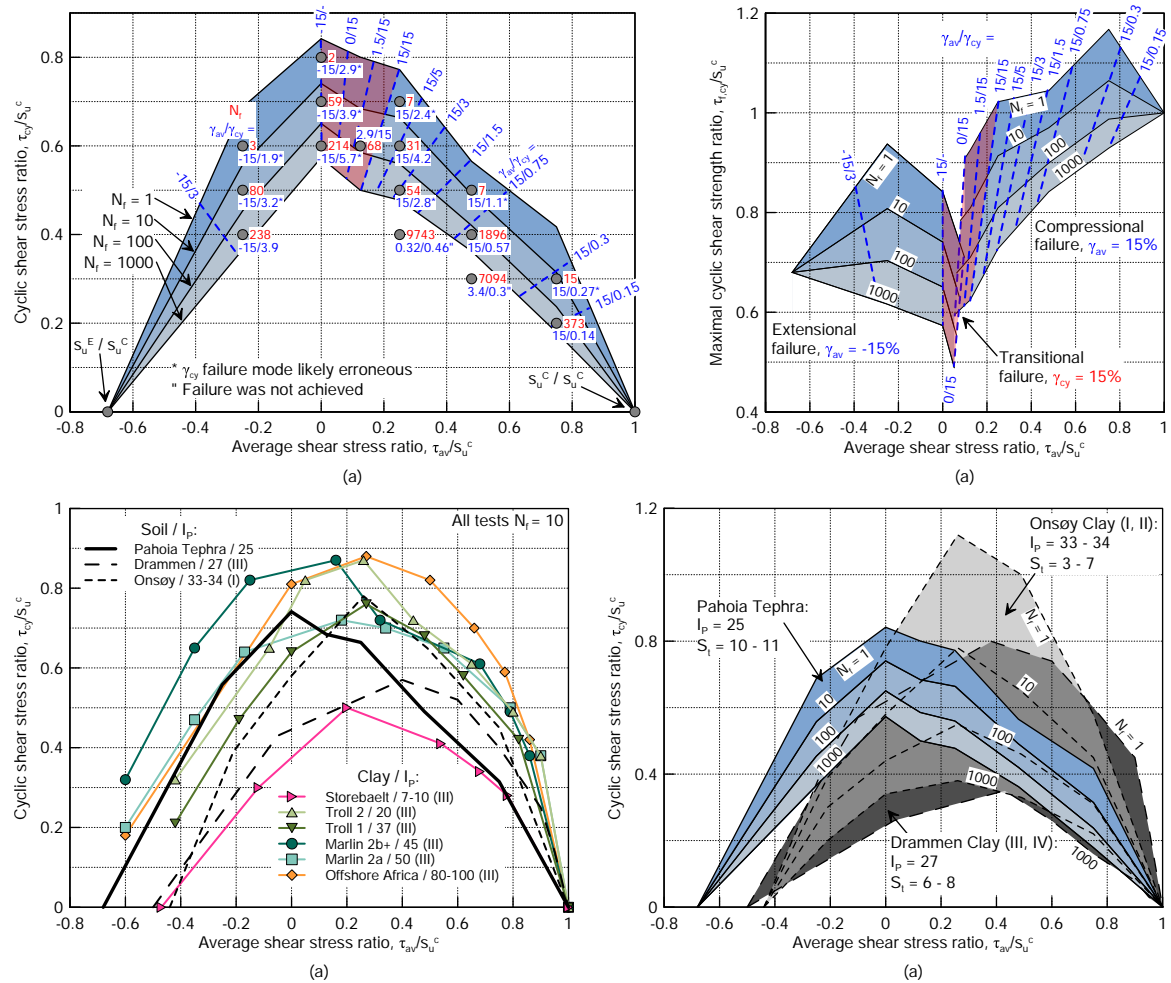


Fig. 4.7 (a) Cyclic shear stress contours for different number of cycles to failure (calculated using Eq. 1 and Fig. 6) as a function of average shear stress. (b) Maximal cyclic shear strength as a function of average shear stress. (c – d) Cyclic shear stress contours compared to Norwegian clays with different plasticity indices and sensitivity. I – Wichtmann et al. (2013), II – Lunne et al. (2003), III – Andersen (2009), IV – Lunne and Lacasse (1999).

Isolines of the shear strain proportions at failure  $\gamma_{av}/\gamma_{cy}$  were added to Fig. 4.7(a) as dashed blue lines. They define the shear stress conditions at which shear failure occurs due to an excessive accumulation of either average shear strain (blue shaded area) or cyclic shear strain (purple shaded area). The calculation of average and cyclic shear strain requires

both the minimum and maximum shear strain of the respective loading cycle (Fig. 4.2). A reliable separation into average and cyclic shear strain was possible in tests where failure was achieved by progressive increase in shear strain, e.g. sample CY-9 in Fig. 4.8. However, some tests failed abruptly during the course of a single loading cycle, e.g. sample CY-22 in Fig. 4.8, hampering the precise separation of the shear strain proportions at failure. Samples with abrupt failure are marked with an asterisk in Fig. 4.7(a) and were weighted less when defining the isolines of shear strains at failure.

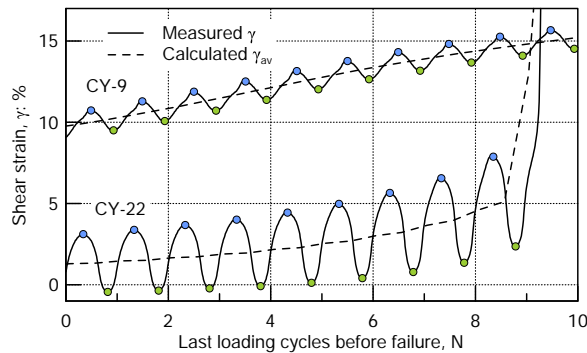


Fig. 4.8 Progressive and abrupt shear strain development during the last loading cycles of test CY-9 and CY-22, respectively.

The maximal cyclic shear strength  $\tau_{f,cy}$  is defined as the sum of the average and cyclic shear stresses at failure, which can be temporarily mobilized during cyclic undrained loading (Fig. 4.7(b)). It may be used to calculate the bearing capacity under cyclic loading (Andersen and Lauritzen, 1988). The calculation of the maximal cyclic shear strength differs for triaxial compression and extension, being  $\tau_{f,cy} = \tau_{av} + \tau_{cy}$  for  $\gamma_{av} \geq 0\%$  and  $\tau_{f,cy} = |\tau_{av} - \tau_{cy}|$  for  $\gamma_{av} \leq 0\%$ . At the transition between compressional and extensional shear strain failure, i.e.  $\gamma_{av} = 0\%$  and  $\gamma_{cy} = 15\%$ , the shear strength contour lines overlap (Andersen, 2015). In the compressional failure region of Fig. 4.7(b), the contour lines for  $N = 1$  and 10 loading cycles are well above the compressional undrained shear strength for large average shear stress ratios. At larger numbers of loading cycles, the contour lines for  $N = 100$  and 1000 are always below the compressional undrained shear strength. This indicates that for a short period of undrained cyclic loading, the Pahoia Tephra can bear more shear stress than under monotonic loading. This might be relevant for the design against strong earthquakes, blasts or storm waves.

Research on cyclic undrained shear strength that used the concept of contour diagrams in the past mainly focused on marine clays. Therefore, we compared the cyclic shear strength of Pahoia Tephra with marine clays only. Lunne et al. (2006) and Lunne and Andersen (2007) showed that sample disturbance reduces the static triaxial compression more than the

static triaxial extensional strength, causing the anisotropy ratio to increase with increasing sample disturbance. In Fig. 4.7(c) the cyclic shear strength contour of the Pahoia Tephra for  $N_f = 10$  loading cycles is compared to that for different marine clays (Andersen, 2004, 2009; Wichtmann et al., 2013). The Pahoia Tephra exhibits an anisotropy ratio  $s_u^E/s_u^C$  of 0.68, which is comparable to tests on tube samples collected from naturally deposited offshore clays. High quality Onsøy Clay block samples (Wichtmann et al., 2013) and Drammen Clay thin-walled tube samples (Andersen, 2009), both reconsolidated in the laboratory, have a lower anisotropy ratio than the Pahoia Tephra.

The cyclic shear strength of the Pahoia Tephra is largest at isotropic stress conditions (Fig. 4.7(a)). Both negative and positive average shear stress, applied in addition to the cyclic shear stress, always decrease the cyclic shear strength. This observation is unique compared to previously published cyclic shear strength contour diagrams for marine clays (Andersen, 2015). Although the general shapes of the cyclic shear strength contours of the marine clays are similar to the cyclic shear strength contours of the Pahoia Tephra, for marine clays the point of maximum cyclic shear stress ratio is shifted to positive average shear stress ratios (Fig. 4.7(c)). This indicates that a small amount of average shear stress strengthens the undrained behaviour in marine clay, but weakens the undrained behaviour of the Pahoia Tephra. This observation is likely related to differences in soil fabric, particle shape, and clay mineralogy between the marine postglacial clays and altered tephra from New Zealand (Bentley et al., 1980; Cunningham et al., 2016; Kluger et al., 2017).

The peak cyclic shear stress ratio of the Pahoia Tephra we observed is consistent with the general relationship that plasticity index increases the cyclic shear strength of soil (Fig. 4.7(c)), which was initially defined for marine clays only (Andersen, 2009; Wichtmann et al., 2013). The Pahoia Tephra exhibits similar peak values of cyclic shear stress ratio to failure after  $N_f = 10$  loading to Onsøy Clay which has a slightly higher plasticity index (Fig. 4.7(c)). Offshore Africa clay with a plasticity index  $I_p$  between 80 and 100 exhibits considerably higher cyclic shear stress ratio than the Pahoia Tephra. In addition, the different shape of the Pahoia Tephra failure contours leads to a significantly higher cyclic shear strength at negative average shear stress, which is similar to the behaviour of highly plastic marine clays (Fig. 4.7(c)).

However, the most significant difference in cyclic shear strength behaviour between the Pahoia Tephra and marine Drammen and Onsøy Clays becomes apparent when comparing the cyclic shear strength contours for different numbers of loading cycles to failure (Fig. 4.7(d)). The Pahoia Tephra does not reach failure after 1000 loading cycles over a much wider range of average and cyclic shear stress ratios compared to marine clay. Additionally, the failure contours are much closer together. For instance, at in situ average shear stress

conditions, the cyclic shear stress ratio of the Pahoia Tephra increases by less than 0.3 when the number of loading cycles  $N_f$  to failure is changed from 1000 to 1. This is only 55% of the increase in cyclic shear strength that is observed for Drammen Clay and 35% of the increase for Onsøy Clay when considering in situ average shear stress ratios (Fig. 4.7(d)). This shows that the Pahoia Tephra is more resistant to small cyclic undrained loading than marine clays, but at a certain shear stress level, the failure occurs over a narrow range of cyclic shear stress ratios. This observation is consistent with the brittle failure observed in our monotonic triaxial tests and in other volcanic-derived soils from New Zealand (Jacquet, 1990). The abrupt failure may be further affected by the higher sensitivity measured for the Pahoia Tephra compared to the marine clays considered (Fig. 4.7(d)).

## 4.6 Conclusions

Sediment covers on volcanic islands are commonly underlain by altered tephra. Understanding their undrained response to cyclic loading is essential to design geotechnical structures against cyclic loading induced by earthquakes, waves and traffic loads. We comprehensively studied the undrained cyclic shear behaviour of an altered, clay-rich tephra from the North Island of New Zealand for the first time through cyclic triaxial tests. We find that:

- The Pahoia Tephra has high sensitivity and contracts during monotonic undrained triaxial tests. Upon failure the tephra experiences considerable strain softening within the range of confining pressures applied in this study, which is similar to brittle failure typically observed in normally consolidated clay. Altered tephra has significantly higher critical friction angles compared with clay, being more similar to sand and unaltered tephra.
- In cyclic undrained triaxial testing, the shear strain development and number of cycles to reach failure of the Pahoia Tephra depends more strongly on average shear stress compared to Norwegian marine clay.
- Cyclic shear strength contour diagrams showed that the Pahoia Tephra exhibits its highest cyclic shear strength at zero average shear stress, which is not observed in marine clay. Average shear stress lowers the cyclic shear strength of the Pahoia Tephra, whereas a small addition of compressive average stress commonly strengthens the undrained response of marine clays.

- The Pahoia Tephra is more resistant to small cyclic undrained loading than marine clays, but above a threshold shear stress, the failure occurs over a narrow range of cyclic shear stress.

The present study highlights that altered tephra exhibits different monotonic and cyclic undrained behaviour than other soil types, which therefore needs to be considered in civil engineering projects. The results here may be used to improve feasibility assessments and preliminary design calculations in subsoils comprised of altered tephra and is a step towards better risk mitigation of geotechnical problems including slope failure.

## Acknowledgments

This research was funded by the DFG Research Center MARUM of the University of Bremen, Germany, through INTERCOAST and the University of Waikato in Hamilton, New Zealand. Parts of the laboratory work were funded by Callaghan Innovation. We thank T. Goetz, T. Manderson, C. Morcom, J. Rau, and B. Stewart for triaxial sampling, D. Culliford, V. Taikato, and T. P. Dempsey from the Coastal Marine Field Station, Tauranga, are gratefully acknowledged for providing assistance during field work. M. E. Jorat and W. de Lange are thankfully acknowledged for their help during borehole logging. We thank M. Huhndorf, R. Radosinsky, and W. Schunn for their laboratory assistance. T. Wichtmann and K. H. Andersen are acknowledged for providing helpful comments on cyclic contour diagrams. We thank M. Ikari and D. A. Hepp for helpful discussions on the paper.

## Author Contributions

M.O. Kluger conceived the project. T. Mörz and V.G. Moon acquired funding for sampling and laboratory experiments. M.O. Kluger and P. Mills carried out the field work. M.O. Kluger designed the experimental program and carried out the triaxial testing, while P. Mills conducted geotechnical index tests. T. Mörz and V.G. Moon supervised this project. M.O. Kluger did the data evaluation, created figures, wrote the first manuscript version, and led the revision process. S. Kreiter revised the manuscript. V.G. Moon, R.P. Orense, and T. Mörz commented on the manuscript. All authors approved the final manuscript.

## Chapter 5

# A new attraction-detachment model for explaining flow sliding in clay-rich tephras

**Max O. Kluger<sup>1</sup>, Vicki G. Moon<sup>2</sup>, Stefan Kreiter<sup>1</sup>, David J. Lowe<sup>2</sup>, G.J. Churchman<sup>3</sup>, Daniel A. Hepp<sup>1</sup>, David Seibel<sup>1</sup>, M. Ehsan Jorat<sup>4</sup>, and Tobias Mörz<sup>1</sup>**

<sup>1</sup>MARUM–Center for Marine Environmental Sciences, University of Bremen, Leobener Straße, 28359 Bremen, Germany

<sup>2</sup>School of Science, University of Waikato, Private Bag 3105, Hamilton 3240, New Zealand

<sup>3</sup>School of Agriculture, Food and Wine, University of Adelaide, Adelaide, SA 5005, Australia

<sup>4</sup>School of Science, Engineering and Technology, Abertay University, Dundee DD11HG, UK

Published in *Geology*, February 2017; v. 45; no. 2; p 131-134

doi:10.1130/G38560.1; ©2016 Geological Society of America

### **Abstract**

Altered pyroclastic (tephra) deposits are highly susceptible to landsliding, leading to fatalities and property damage every year. Halloysite, a low-activity clay mineral, is commonly associated with landslide-prone layers within altered tephra successions, especially in deposits with

high sensitivity, which describes the post-failure strength loss. However, the precise role of halloysite in the development of sensitivity, and thus in sudden and unpredictable landsliding, is unknown. Here we show that an abundance of mushroom cap-shaped (MCS) spheroidal halloysite governs the development of sensitivity, and hence proneness to landsliding, in altered rhyolitic tephtras, North Island, New Zealand. We found that a highly sensitive layer, which was involved in a flow slide, has a remarkably high content of aggregated MCS spheroids with substantial openings on one side. We suggest that short-range electrostatic and van der Waals interactions enabled the MCS spheroids to form interconnected aggregates by attraction between the edges of numerous paired silanol and aluminol sheets that are exposed in the openings and the convex silanol faces on the exterior surfaces of adjacent MCS spheroids. If these weak attractions are overcome during slope failure, multiple, weakly attracted MCS spheroids can be separated from one another, and the prevailing repulsion between exterior MCS surfaces results in a low remolded shear strength, a high sensitivity, and a high propensity for flow sliding. The evidence indicates that the attraction-detachment model explains the high sensitivity and contributes to an improved understanding of the mechanisms of flow sliding in sensitive, altered tephtras rich in spheroidal halloysite.

**Keywords** Landslide · halloysite morphology · halloysite spheroids · sensitivity · tephtra · structural breakdown · electrostatic interactions · variable charge · coulombic forces · van der Waals' forces · Quaternary

## 5.1 Introduction

Most East Asian and western Pacific countries are located in tectonically active, high-rainfall areas where landslides are a major natural hazard. These landslides are typically triggered by rainstorms or earthquakes and are responsible for fatalities and enormous property damage every year. Many destructive landslides have occurred in pyroclastic deposits in Japan, Indonesia, Hong Kong, and New Zealand (Chau et al., 2004; Chigira, 2014; Moon, 2016), such deposits commonly containing layers rich in clay minerals formed mainly by chemical weathering during either pedogenesis or diagenesis. In regions with predominantly rhyolitic volcanism, halloysite is a common clay mineral (Churchman and Lowe, 2012) and is therefore potentially a key geological factor increasing the risk of landslides (Kirk et al., 1997; Chigira, 2014). Halloysite is a 1:1 Si:Al layered aluminosilicate member of the kaolin subgroup that exhibits various structural morphologies including tubes, spheroids, polyhedrons, plates, and books (Joussein et al., 2005; Cunningham et al., 2016).

Spheroidal halloysite, in particular, has been recognized in landslide-prone layers of pyroclastic material in Japan (Tanaka, 1992) and New Zealand (Smalley et al., 1980). Smalley et al. (1980) linked a high content of spheroidal halloysite to high sensitivity. Sensitivity refers to the post-failure strength loss in the failure zone during landsliding, and is quantified in the laboratory as the ratio of the undisturbed to remolded undrained shear strength at the same water content (Terzaghi, 1944). High sensitivities were first described for post-glacial, brackish and marine clayey sediments in the Northern Hemisphere (Skempton and Northey, 1952) that are subject to landslides with dimensions and long runout distances that are difficult to predict. In this study, we investigate processes that have led to high sensitivity in halloysite-rich pyroclastic materials in order to improve landslide-hazard evaluation.

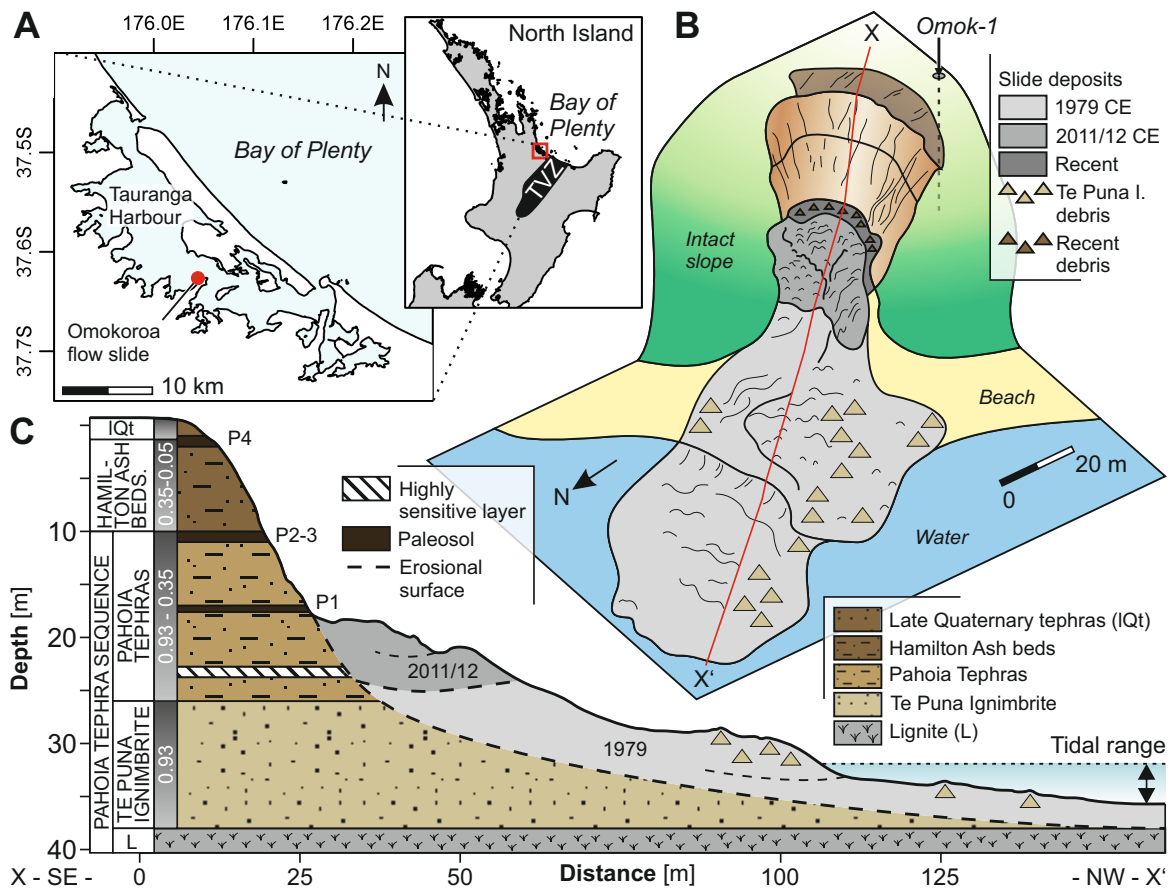


Fig. 5.1 A: Map of Tauranga Harbour, New Zealand, with Taupo Volcanic Zone (TVZ) as main source for Quaternary tephras at study site. B: Three-dimensional view of the flow slide at Omokoroa; red line marks position of profile in C. I.—Ignimbrite. C: Profile through flow slide with simplified stratigraphy and associated paleosols (P1–P4) of drill core Omok-1 and ages (in Ma) after Moon et al. (2015b).

## 5.2 Geological setting

Much of the central part of New Zealand's North Island is covered by thick rhyolitic tephtras (Lowe, 2011) derived from eruptions in the Taupo Volcanic Zone (Briggs et al., 2005), which are commonly altered into halloysite-rich successions. We focus here on a coastal flow slide at Omokoroa, Bay of Plenty (Fig. 5.1A), where  $\sim 10,000 m^3$  of material was transported downslope over long distance into a lagoon in 1979 CE (Moon et al., 2015b) as well as during two minor reactivations in 2011 and 2012. The 1979 event was likely initiated in a white, highly sensitive layer with high spheroidal halloysite concentration (Smalley et al., 1980) (and lacking any detectable allophane; Cunningham et al. (2016)).

We have analyzed a 40-m-long sediment core, *Omok-1*, which we bored via rotary flush drilling in unfailed material near the headwall (Fig. 5.1B). The lithology of Omok-1 was determined by correlation with units of a previously studied adjacent headwall face (Moon et al., 2015b) comprising a succession mainly of Quaternary rhyolitic tephtras: underlain by lignite at the base of the core, the Pahoia Tephtra sequence includes the Te Puna Ignimbrite (ca. 0.93 Ma) and a series of altered tephtras which are informally divided into lower and upper Pahoia Tephtra units based on two distinct paleosols (P1 and P3). All of these deposits and paleosols are overlain by successions of younger altered tephtras called Hamilton Ash beds (ca. 0.35 to ca. 0.05 Ma) and late Quaternary tephtras ( $< ca. 0.05 Ma$ ) (Figs. 5.1C and 5.2A). The lower Pahoia Tephtras include the 0.3-m-thick, white, highly sensitive clay-rich layer that failed in 1979 (Fig. 5.1C), having high porosity and high natural water content (Smalley et al., 1980).

## 5.3 Methods

We performed laboratory vane shear tests on samples from the Pahoia Tephtra sequence and Hamilton Ash beds to measure the sensitivity  $S$  (Equ. 5.1):

$$S = s_u/s_r, \quad (5.1)$$

where the undisturbed strength ( $s_u$ ) was measured on the intact surface of the split core, and the remolded strength ( $s_r$ ) was measured on core samples with the same water content but that had been kneaded by hand for 10 min (Jacquet, 1990). Halloysite concentration in bulk samples was measured by X-ray diffraction (XRD) using a Philips PW analytical diffractometer, and quantification was performed using QUAX software (Vogt et al., 2002). Scanning electron microscopy (SEM) was undertaken with a Zeiss Supra40 microscope on 24 shock-frozen, freeze-dried, and gold-coated bulk core samples (Reed, 2005). The relative

abundances of halloysite particles having distinct morphologies were quantified using a point-counting approach (Frolov and Maling, 1969). Six representative SEM images of planar soil surfaces were chosen for each sample, and at least 600 particles were counted based on rectangular grids. In the white, highly sensitive layer, the change of halloysite particle arrangement upon remolding was quantified by comparing 20 SEM images of undisturbed and remolded material, providing >1000 counts respectively. The spheroid diameters were measured from six representative particles per SEM image.

## 5.4 Highly sensitive slide-prone layer dominated by spheroidal halloysite

The sensitivity is low in the upper Pahoia Tephra, especially in the paleosols P2 and P3 (Figs. 5.2A and 5.2B). However, the sensitivity tends to increase with depth, reaching values of 15–20 in the lower Pahoia Tephra. The highest sensitivity (Rosenqvist, 1953) of  $S = 55$ , and the lowest remolded shear strength within the profile of  $s_r = 1.4 \text{ kPa}$ , were measured in the white, highly sensitive layer at 23 m depth.

The upper Pahoia Tephra have a halloysite content of 10–20 wt % comprising almost entirely tubular halloysite (Figs. 5.2C and 5.2D). The lower Pahoia Tephra have 40–50 wt % halloysite comprising mostly spheroidal particles. In the highly sensitive layer, 76% of the halloysite is spheroidal and the spheroid sizes are greater than those in the surrounding layers (Figs. 5.2D and 5.2E). A three-dimensional line plot reveals a clear correlation between high sensitivities and high halloysite bulk concentration, and a high content of spheroids with large diameters (Fig. 5.2F). The high sensitivity is associated with low remolded shear strength rather than with high undisturbed shear strength (Fig. 5.2G).

We found that deposits with high tubular halloysite content hamper sensitivity development, whereas halloysite spheroids facilitate sensitivity and dominate the highly sensitive layer at 23 m depth within the lower Pahoia Tephra. The highly sensitive layer has low remolded shear strength after failure, which, together with its high water content (Smalley et al., 1980), partly contributed to the long runout distance of the flow slide at Omokoroa.

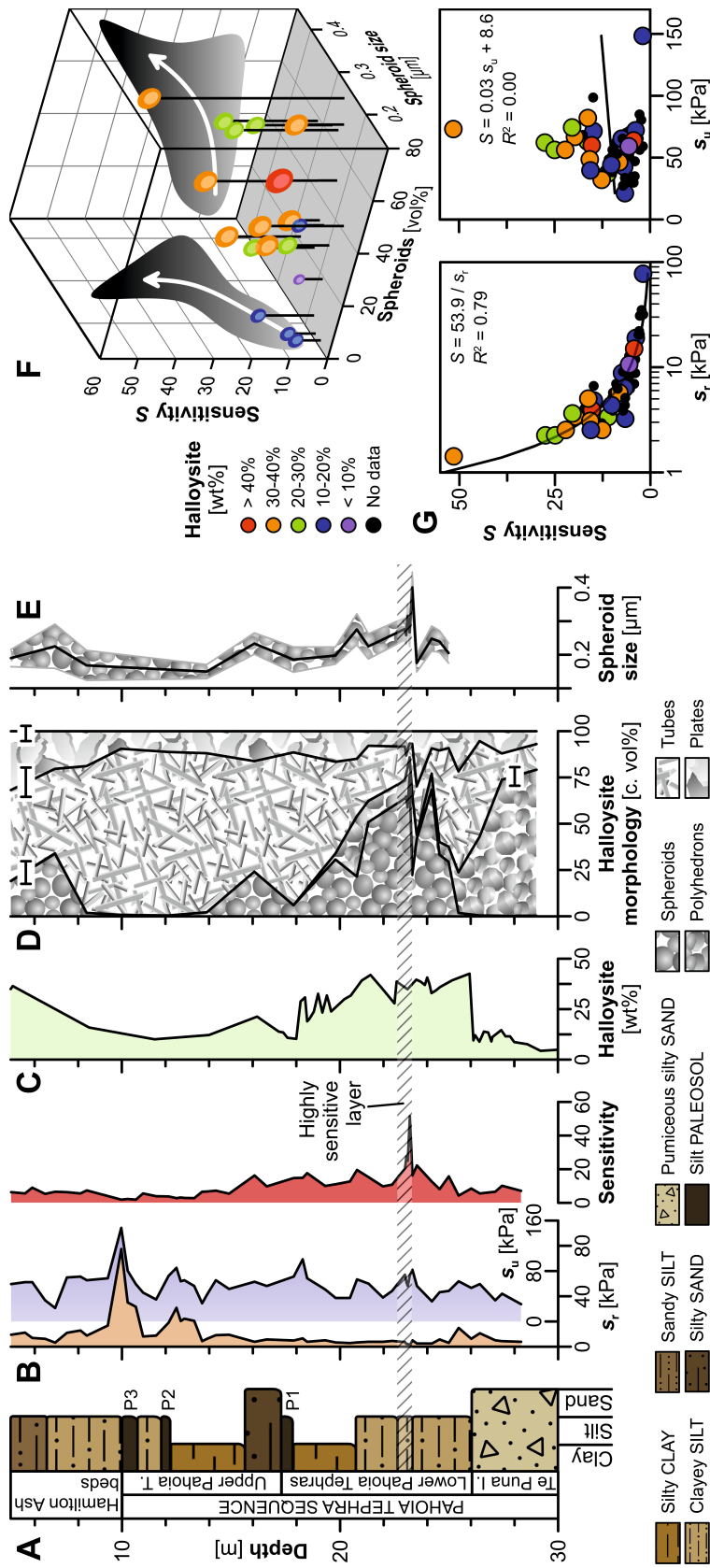


Fig. 5.2 A: Stratigraphy of drill core Omok-1 after Moon et al. (2015b) showing main lithological units as defined in Figure 5.1, three paleosols (P1-P3), and highly sensitive white layer at 23 m depth (hatched area). I.-Ignimbrite; T.-Tephra. B: Undisturbed ( $s_r$ , blue) and remolded ( $s_u$ , orange) shear strength, and sensitivity ( $S = s_r/s_u$ ). C: Haloisite bulk concentration. D: Cumulative volume percent (c. vol %) of haloisite morphologies with bars indicating average standard deviations. E: Average spheroid sizes with standard deviations depicted by fill patterns. F: Three-dimensional line plot illustrating relationship between spheroid content, sensitivity, spheroid size, and haloisite concentration; gray graded areas enable trends in sensitivity to be visualized. G: Dependency between sensitivity and shear strength.

## 5.5 New Halloysite morphology

We present here the first observations of a previously unreported halloysite particle morphology, which is visible in the SEM images of the remolded halloysite fabrics of the highly sensitive layer. In the undisturbed state, the spheroidal halloysites are distinctly aggregated into networks of well-connected particles (Figs. 5.3E and 5.3F). After remolding, however, most of the aggregates have broken apart into small, loose clusters or individual halloysite particles that are typically  $\sim 250 - 400$  nm in diameter (Figs. 5.3G and 5.3H). Individual spheroids have distinctive "deformities" in the form of openings  $\sim 80 - 160$  nm in diameter on one side. These openings were previously hidden by contact with other spheroids. The deformities give the particles an ovate "mushroom cap" appearance. Pointcounting individual mushroom-cap shapes in both undisturbed (aggregated) and remolded (disaggregated) samples showed that the observable mushroom-cap shapes were much more abundant in the remolded samples, increasing from  $4.4\% \pm 3.2\%$  to  $44.9\% \pm 11.6\%$ .

## 5.6 Attraction-detachment model for flow sliding in altered tephtras

The open-sided, mushroom cap-shaped halloysite morphology has not been reported previously. Because this particular morphology overwhelmingly occurs in the highly sensitive slide-prone layer, we hypothesize that this unique particle shape controls the mechanical behavior of halloysite clays.

Halloysite is composed of an Al-octahedral (aluminol) sheet with a net positive charge and a Si-tetrahedral (silanol) sheet with a net negative charge at pH values between 2 and 8 (Fig. 5.3I) (Churchman et al., 2016). The two sheets have slightly different dimensions, with the silanol sheet being larger. This misfit in the sheet sizes causes the halloysite layer to be curved (Churchman and Lowe, 2012), with the larger negatively charged silanol sheet on the outside of the curvature and the positively charged smaller aluminol sheet on the inside. The halloysite spheroids observed in our study are most likely composed of concentrically stacked 1:1 layers, i.e., with an onion-like structure, as shown in numerous studies including those on spheroidal halloysite derived from altered tephtras in New Zealand, Japan, and Argentina (Wada et al., 1977; Kirkman, 1981; Cravero et al., 2012; Berthonneau et al., 2015). For a perfect halloysite spheroid, the outermost silanol surface carries a net negative charge, and hence the electrostatic interactions between individual spheroids would be repulsive (Fig. 5.3I). Our study shows, however, a halloysite structure where both silanol and aluminol layers are exposed at spheroid openings, and therefore charges

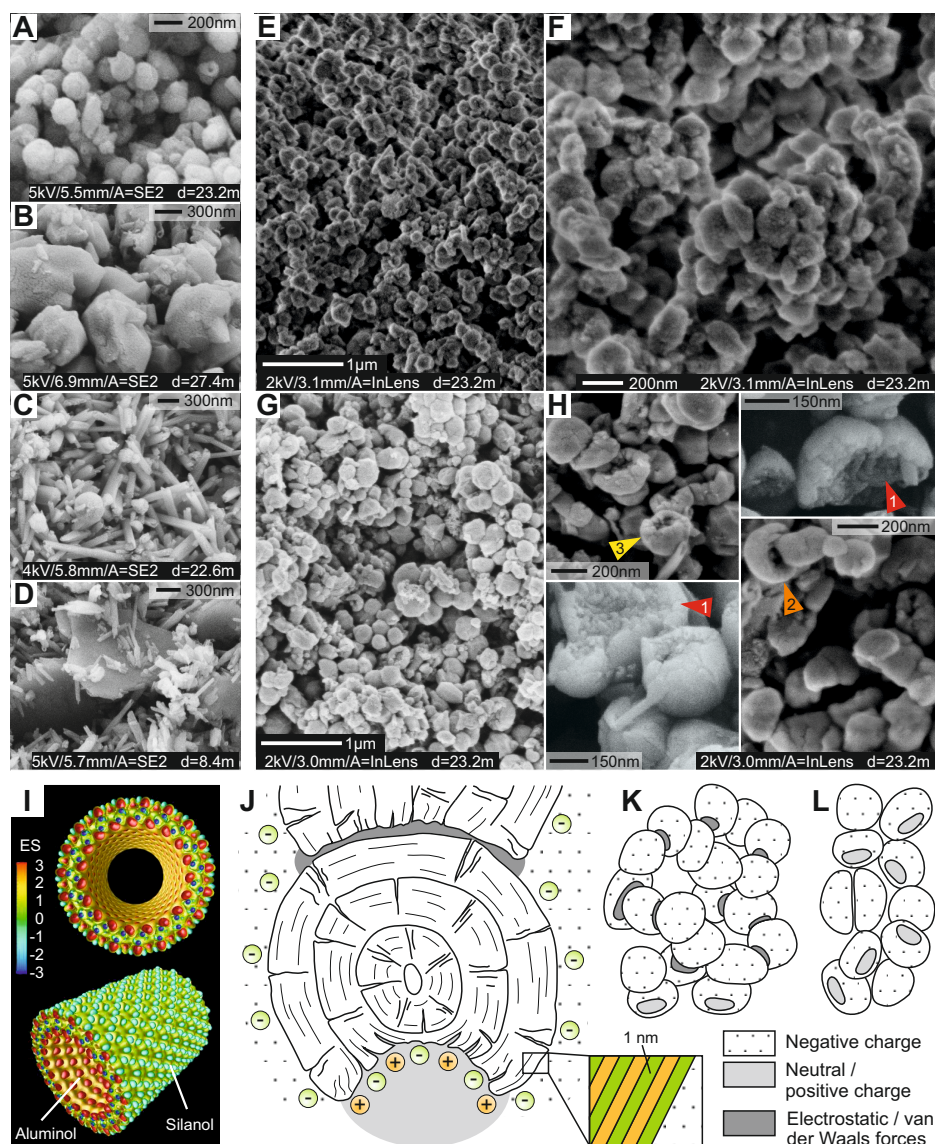


Fig. 5.3 A–D: Scanning electron microscopy (SEM) images of spheroids (A), polyhedrons (B), tubes (C), and plates (D) representing the main halloysite morphologies in Pahoia Tephra sequence (New Zealand). E–H: SEM images from the highly sensitive layer of undisturbed and multiply-connected halloysite spheroids (E,F) and remolded spheroids (G,H) showing smaller clusters or detached spheroids within much looser particle network. 1–exposed layers in spheroid openings; 2–partially separated halloysite spheroids; 3–detached mushroom cap-shaped halloysite spheroid. I: Electrostatic field proximal to halloysite nanotubes with colored equipotential surfaces (ES), modified with permission from Guimarães et al. (2010), copyright 2010 American Chemical Society. J: Conceptual mushroom cap-shaped spheroid cross-section and weak electrostatic and/or van der Waals attractions arising between exposed silanol-aluminol sheets in spheroid openings and negatively charged convex exterior surfaces; enlargement is adapted from Berthonneau et al. (2015). Circles with + and – relate to positive and negative electrostatic field proximal to spheroid’s exterior surface. K,L: Mushroom cap-shaped spheroids connect with one another between concave openings and convex outer spheroid surfaces, forming aggregates (K) which are partly detached because of remolding (L).

within the openings would correspondingly be weakly positive or neutral overall (Fig. 5.3J), as indicated from charge density-functional tight-binding modeling applied to halloysite nanotubes (Guimarães et al., 2010). If sufficient numbers of positively charged openings are exposed, the electrostatic interactions between them and the negative exterior silanol surfaces would allow the mushroom cap-shaped spheroids to form stacked aggregates (Fig. 5.3K). If the paired silanol and aluminol sheets exposed in the openings are neutral overall, then a net increase in particle attraction will still occur because electrostatic repulsion is reduced and the larger contact areas lead to higher van der Waals forces (Israelachvili, 2011).

During diagenesis via hydrolysis of volcanic glass (Cunningham et al., 2016), the halloysite spheroids may form consecutively on top of one another in pore spaces, generating the distinct openings during synthesis. The attractive forces between the openings and the convex exterior surfaces are demonstrably strong enough to allow for the formation of aggregates, but also permit easy disaggregation by mechanical detachment during shear (Fig. 5.3L). New random contacts between convex silanol surfaces probably lead to a decrease in average attraction between particles. We posit that the detachment of attractive spheroidal particle contacts, in the presence of abundant water having negligible interaction with ions in soil solution because of the inactive nature of halloysite (Smalley et al., 1980), leads to the very low post-failure shear strength, facilitating a flow slide with long runout distance. The interparticle attraction-detachment model appears to successfully explain (at nanoscale dimensions) the post-failure behavior of the highly sensitive tephra layer at Omokoroa, which is dominated by the imperfect halloysite spheroids. The question therefore arises whether similar altered tephtras elsewhere have high contents of spheroidal halloysite with potentially hidden mushroom-cap forms, and whether such forms helped mobilize other landslides in the past.

## 5.7 Conclusions

We investigated a sequence of altered, rhyolitic Quaternary tephtras in New Zealand and the reasons why a landslide-prone layer dominated by spheroidal halloysite was highly sensitive. We explain this high sensitivity with an electrostatic attraction-detachment model. Weakly positive or neutral charges on silanol and aluminol sheet edges exposed in the concave openings of spheroidal halloysite particles were attracted to the negatively charged convex silanol surfaces of adjacent spheroids. Such short-range attractions between spheroid openings and the exterior surfaces of adjacent spheroids stabilize an aggregated halloysite framework. If the aggregates are detached by remolding, the loose arrangement of the spheroids exhibits low remolded shear strength. We suggest that the attraction-detachment

model, based on the identification of mushroom-cap halloysite morphologies, provides a potential key for the identification of sensitive altered tephras that are predisposed to sudden failure that triggers landsliding.

## **Acknowledgments**

This research was funded by the DFG Research Center MARUM (University of Bremen) through INTERCOAST and the University of Waikato (Hamilton, New Zealand). We thank C. Schulze for vane shear tests; B. Steinborn and C. Vogt for XRD analyses; P. Witte, A. Hübner, C. Schott, S. Buchheister, and V. Diekamp for laboratory assistance; M. Ikari, F. Sense, J. Lane, and P. Pasbakhsh for comments; and F. Terrible, J.K. Torrance, F. Cravero, M. McSaveney, and an anonymous reviewer for helpful reviews.

## **Author Contributions**

M.O. Kluger and S. Kreiter conceived the project. T. Mörz, V.G. Moon, and M.E. Jorat acquired funding for core drilling and laboratory and field experiments. M.O. Kluger designed and led the experimental program, and did parts of the laboratory experiments. D. Seibel did most of the scanning electron microscopic analyses and S. Kreiter, T. Mörz, V.G. Moon, and M.E. Jorat carried out the drilling campaign. T. Mörz, V.G. Moon, and D.J. Lowe supervised this project. M.O. Kluger did most of the data evaluation, created figures, wrote the first manuscript version, and led the revision process. D. Seibel contributed to the data evaluation. D.J. Lowe largely contributed to discussion and revised and edited the first and subsequent manuscript versions. V.G. Moon, S. Kreiter, G.J. Churchman, T. Mörz, and D.A. Hepp contributed to discussion and revised the final version of the manuscript. All authors approved the final manuscript.

# Chapter 6

## Conclusions

This doctoral thesis contributed to broaden the understanding of pre- and post-failure mechanisms of landslides in sensitive soil at the interface between land and water. Two landslides were investigated that occurred in sensitive soil and affected society, economy, and natural environment in coastal regions: (1) The coastal submarine Orkdalsfjord landslide in post-glacial sediments, Norway, and (2) the coastal subaerial Omokoroa flow slide in weathered tephra, New Zealand. The following section summarizes the most important findings in response to the research hypotheses (Chapter 1.5).

**Cyclic loading affects the in situ shear strength of sensitive glacio-marine soil:** The in situ weakening of the Orkdalsfjord landslide during cyclic loading was investigated using static and vibratory cone penetration testing (CPTU) and two gravity cores obtained during expedition POS472 from the Orkdalsfjord landslide headwall. Small scale grain size variabilities within the stratified clayey to sandy fjord sediments were detected. Interbedded very coarse silt layers lose up to 68 % cone resistance during vibratory CPTU and are therefore considered as more vulnerable to cyclic loading compared to surrounding finer silts in which no decrease in cone resistance was detected. This shows that only relatively small vibrations are necessary to considerably reduce the shear strength of very coarse silt layers. This observation is supported by cyclic triaxial testing, in which very coarse silt fails after five times fewer number of loading cycles compared to medium-coarse silt. Accordingly, the very coarse silt layers may have contributed to the weakening of the Orkdalsfjord landslide in case cyclic loading occurred during landsliding.

**Cyclic shear strength of sensitive weathered tephra differs from post-glacial sensitive clay:** The cyclic loading behavior of the halloysite-rich Pahoia Tephra from an interval above the failure surface of the Omokoroa flow slide was analyzed by monotonic and cyclic triaxial testing. The Pahoia Tephra contracts during monotonic undrained triaxial tests. Upon failure, the weathered tephra experiences considerable strain softening, which is similar

to brittle failure observed in sensitive post-glacial clay. Weathered tephra has significantly higher critical friction angle than clay, being comparable to sand or unaltered tephra. Based on cyclic undrained triaxial testing, the shear strain development and number of cycles to reach failure of the Pahoia Tephra depends more strongly on average and cyclic shear stress compared with sensitive post-glacial clay. The Pahoia Tephra exhibits its highest cyclic shear strength at isotropic stress conditions, which is different to the sensitive post-glacial clays considered. Average shear stress lowers the cyclic shear strength of the Pahoia Tephra, while a limited addition of average shear stress commonly strengthens the undrained response of marine clays. The Pahoia Tephra is more stable against small cyclic undrained loading than marine clays, but above a threshold shear stress, the failure occurs rather suddenly over a narrow range of cyclic shear stress. The results may be used to improve feasibility assessments and preliminary design calculations in subsoils comprised of sensitive weathered tephra and is a first step towards better risk mitigation of slope failure.

**High sensitivity in weathered tephra is caused by specific halloysite morphologies:**

The role of secondary clay minerals on the development of high sensitivities, thus in the post-failure softening during the Omokoroa flow slide was analyzed along a drill core using scanning electron microscopy and laboratory vane shear tests. Halloysite dominates the Pahoia Tephra, a sequence that was involved in the Omokoroa flow slide. The halloysite particle morphologies are highly variable with depth. While tubular morphologies are prevalent in the upper tephra successions, the lower Pahoia Tephra sequence is dominated by spheroidal halloysite. This change in halloysite morphology coincides with an increase in sensitivity with depth. Therefore, spheroidal halloysite is likely the key in the development of sensitivity in weathered tephra from New Zealand and potentially elsewhere in regions of similar volcanic origin. In the failure surface of the Omokoroa flow slide, a new open-sided spheroidal halloysite particle shape in the form of 'mushroom caps' is recognized for the first time that governs the development of high mobility in the failure surface during landsliding. Based on a new 'attraction-detachment' model, it is suggested that the rearrangement in the halloysite texture during the failure process reduces the attractions between the particles at nanoscale dimensions and thus predisposes flow sliding.

Various aspects of the cyclic loading behavior of sensitive post-glacial silts and weathered tephra were studied, contributing to a better understanding of landslide initiation during cyclic loading scenarios such as earthquakes. Both soil types are vulnerable to cyclic loading, which therefore needs to be considered when planning civil engineering projects on or close to slopes comprised of post-glacial silt or weathered tephra. A new conceptual model explains the high sensitivities in halloysite-rich tephra and therefore the post-failure softening during

landsliding, which provides a potential key for the identification of sensitive weathered tephra that are predisposed to flow sliding.



# References

- Achmus, M. (2010). Untersuchungen zu OWEA-Gründungsstrukturen im Projekt GI-GAWIND alpha ventus. In *Workshop Gründung von Offshore-Windenergieanlagen, Triantafyllidis T (ed.)*. Karlsruhe Institut für Technologie: Karlsruhe, pages 183–200.
- Alarcon-Guzman, A., Leonards, G., and Chameau, J. (1988). Undrained monotonic and cyclic strength of sands. *Journal of Geotechnical Engineering*, 114(10):1089–1109.
- Anaraki, K. (2008). Hypoplasticity investigated: Parameter determination and numerical simulation. Master's thesis, MS Thesis, Delft University of Technology, Delft.
- Andersen, K. (2004). Cyclic clay data for foundation design of structures subjected to wave loading. In *Proceedings of the International Conference on Cyclic Behaviour of Soils and Liquefaction Phenomena, CBS04, Bochum, Germany*, volume 31, pages 371–387.
- Andersen, K. (2015). Cyclic soil parameters for offshore foundation design. *Frontiers in Offshore Geotechnics III*, page 5.
- Andersen, K. H. (2009). Bearing capacity under cyclic loading-offshore, along the coast, and on land. the 21st bjerrum lecture presented in oslo, 23 november 2007. *Canadian Geotechnical Journal*, 46(5):513–535.
- Andersen, K. H. and Lauritzsen, R. (1988). Bearing capacity for foundations with cyclic loads. *Journal of Geotechnical Engineering*, 114(5):540–555.
- Andersson-Sköld, Y., Torrance, J. K., Lind, B., Odén, K., Stevens, R. L., and Rankka, K. (2005). Quick clay—a case study of chemical perspective in southwest sweden. *Engineering Geology*, 82(2):107–118.
- Ansal, A. M. and Erken, A. (1989). Undrained behavior of clay under cyclic shear stresses. *Journal of Geotechnical Engineering*, 115(7):968–983.
- Assier-Rzadkieaicz, S., Heinrich, P., Sabatier, P., Savoye, B., and Bourillet, J. (2000). Numerical modelling of a landslide-generated tsunami: the 1979 nice event. *Pure and Applied Geophysics*, 157(10):1707–1727.
- ASTM D 4318-10 (2010). Standard test methods for liquid limit, plastic limit, and plasticity index of soils. *Annual Book of ASTM Standards*, 4:1–16.
- ASTM D 4767-04 (2004). Standard test method for consolidated undrained triaxial compression test for cohesive soils. ASTM Int., West Conshohocken, Pa.

- Bałachowski, L. (2006). Penetration resistance of lubiatowo sand in calibration chamber tests. *Archives of Hydro-Engineering and Environmental Mechanics*, 53(4):311–329.
- Bauer, E. (1996). Calibration of a comprehensive hypoplastic model for granular materials. *Soils and Foundations*, 36:13–36.
- Bayne, J. and Tjelta, T. (1987). Advanced cone penetrometer development for in-situ testing at gullfaks c. In *Proceedings of the 19th Offshore Technology Conference, Houston*, volume 4, pages 531–540.
- Bentley, S. P., Clark, N. J., and Smalley, I. J. (1980). Mineralogy of a norwegian postglacial clay and some geotechnical implications. *The Canadian Mineralogist*, 18(4):535–547.
- Berthonneau, J., Grauby, O., Jeannin, C., Chaudanson, D., Joussein, E., and Baronnet, A. (2015). Native morphology of hydrated spheroidal halloysite observed by environmental transmission electron microscopy. *Clays and Clay Minerals*, 63(5):368–377.
- Bishop, A. (1971). The influence of progressive failure on the choice of the method of stability analysis. *Geotechnique*, 21(2):168–172.
- Bjerrum, L. (1967). Progressive failure in slopes of overconsolidated plastic clay and clay shales. *Journal of Soil Mechanics & Foundations Div.*
- Bjerrum, L. (1971). Subaqueous slope failures in norwegian fjords. *Norwegian Geotechnical Institute Publ*, (88).
- Bolton, M. (1986). The strength and dilatancy of sands. *Géotechnique*, 36(1):65–78.
- Bonita, J. A. (2000). *The effects of vibration on the penetration resistance and pore water pressure in sands*. PhD thesis, Virginia Polytechnic Institute and State University.
- Boulanger, R. W. and Idriss, I. (2006). Liquefaction susceptibility criteria for silts and clays. *Journal of Geotechnical and Geoenvironmental Engineering*, 132(11):1413–1426.
- Boulanger, R. W. and Idriss, I. (2007). Evaluation of cyclic softening in silts and clays. *Journal of geotechnical and geoenvironmental engineering*, 133(6):641–652.
- Briggs, R., Houghton, B., McWilliams, M., and Wilson, C. (2005). 40ar/39ar ages of silicic volcanic rocks in the tauranga-kaimai area, new zealand: dating the transition between volcanism in the coromandel arc and the taupo volcanic zone. *New Zealand Journal of Geology and Geophysics*, 48(3):459–469.
- Brooker, E. W. and Ireland, H. O. (1965). Earth pressures at rest related to stress history. *Canadian Geotechnical Journal*, 2(1):1–15.
- Casagrande, A. (1932). Research on the atterberg limits of soils. *Public Roads*, 13(8):121–136.
- Chatra, A. S. and Dadagoudar, G. (2010). Numerical simulation of hypoplastic constitutive model for sand. *GEOtrendz, Indian Geotechnical Conference*.

- Chau, K., Sze, Y., Fung, M., Wong, W., Fong, E., and Chan, L. (2004). Landslide hazard analysis for hong kong using landslide inventory and gis. *Computers & Geosciences*, 30(4):429–443.
- Chigira, M. (2014). Geological and geomorphological features of deep-seated catastrophic landslides in tectonically active regions of asia and implications for hazard mapping. *Episodes*, 37(4):284–294.
- Chu, D. B., Stewart, J. P., Lee, S., Tsai, J.-S., Lin, P., Chu, B., Seed, R. B., Hsu, S., Yu, M., and Wang, M. C. (2004). Documentation of soil conditions at liquefaction and non-liquefaction sites from 1999 chi–chi (taiwan) earthquake. *Soil Dynamics and Earthquake Engineering*, 24(9):647–657.
- Churchman, G. and Lowe, D. J. (2012). Alteration, formation, and occurrence of minerals in soils. In Huang, P. M., Li, Y., and Sumner, M. E., editors, *Handbook of Soil Sciences. Properties and Processes, 2nd edition*, pages 20.1–20.72. CRC Press, USA.
- Churchman, G., Pasbakhsh, P., Lowe, D., and Theng, B. (2016). Unique but diverse: some observations on the formation, structure, and morphology of halloysite. *Clay Minerals (in press)*.
- Cornforth, D. H. (1973). Prediction of drained strength of sands from relative density measurements. *ASTM STP*, 523:281–303.
- Cravero, F., Maiza, P., and Marfil, S. (2012). Halloysite in argentinian deposits: origin and textural constraints. *Clay Minerals*, 47(3):329–340.
- Cunningham, M. J., Lowe, D. J., Wyatt, J. B., Moon, V. G., and Jock Churchman, G. (2016). Discovery of halloysite books in altered silicic quaternary tephras, northern new zealand. *Clay Minerals*, 51(3):351–372.
- Das, B. (2010). *Principles of foundation engineering*. Cengage Learning.
- DeGregorio, V. B. (1990). Loading systems, sample preparation, and liquefaction. *Journal of geotechnical engineering*, 116(5):805–821.
- Della, N., Belkhatir, M., Arab, A., Canou, J., and Dupla, J.-C. (2014). Effect of fabric method on instability behavior of granular material. *Acta Mechanica*, pages 1–15.
- Demers, D., Robitaille, D., Locat, P., and Potvin, J. (2014). Inventory of large landslides in sensitive clay in the province of québec, canada: preliminary analysis. In L'Heureux, J.-S., Locat, A., Leroueil, S., Demers, D., and Locat, J., editors, *Landslides in Sensitive Clays: From Geosciences to Risk Management*, pages 77–89. Springer Netherlands, Dordrecht.
- Diaz-Rodriguez, J., Leroueil, S., and Aleman, J. (1992). Yielding of mexico city clay and other natural clays. *Journal of Geotechnical Engineering*, 118(7):981–995.
- DIN 18126:1996-11 (1996). Soil, investigation and testing - determination of density of non-cohesive soils for maximum and minimum compactness.
- DIN 18127:2012-09 (2012). Soil, investigation and testing - proctor-test.

- DIN 18137-2:2011-04 (2011). Soil investigation and testing - determination of shear strength - part 2: triaxial test. Beuth.
- DIN 4094-4:2002-01 (2002). Subsoil - field testing - part 4: field vane test. Beuth Verlag GmbH.
- DIN EN 1997-1/NA:2010-12 (2010). National annex - nationally determined parameters - eurocode 7: Geotechnical design - part 1: General rules.
- DIN EN ISO 14688-2:2004 (2004). Geotechnical investigation and testing - identification and classification of soil - part 2: Principles for a classification.
- Duncan, J. M., Wright, S. G., and Brandon, T. L. (2014). *Soil strength and slope stability*. John Wiley & Sons.
- Eckel, E. B. (1958). Introduction to landslides and engineering practice. *Highway Research Board Special Report*, (29).
- Egashira, K. and Ohtsubo, M. (1982). Smectite in marine quick-clays of japan. *CLAYS CLAY MINER. Clays Clay Miner.*, 30(4):275.
- Ehlers, J., Eissmann, L., Lippstreu, L., Stephan, H.-J., and Wansa, S. (2004). Pleistocene glaciations of north germany. *Developments in Quaternary Sciences*, 2:135–146.
- Ezaoui, A. and Di Benedetto, H. (2009). Experimental measurements of the global anisotropic elastic behaviour of dry hostun sand during triaxial tests, and effect of sample preparation. *Géotechnique*, 59(7):621–635.
- Fjeldskaar, W., Lindholm, C., Dehls, J. F., and Fjeldskaar, I. (2000). Postglacial uplift, neotectonics and seismicity in fennoscandia. *Quaternary Science Reviews*, 19(14):1413–1422.
- Fleischer, M., Kreiter, S., Mörz, T., and Huhndorf, M. (2016). A small volume calibration chamber for cone penetration testing (cpt) on submarine soils. In *Submarine Mass Movements and their Consequences*, pages 181–189. Springer.
- Folk, R. L. (2002). Petrology of sedimentary rocks.
- Folk, R. L. and Ward, W. C. (1957). Brazos river bar: a study in the significance of grain size parameters. *Journal of Sedimentary Research*, 27(1).
- Friedman, G. M. and Johnson, K. G. (1982). *Exercises in Sedimentology*. Wiley.
- Frolov, Y. and Maling, D. (1969). The accuracy of area measurement by point counting techniques. *The Cartographic Journal*, 6(1):21–35.
- Frost, J. D. and Park, J.-Y. (2003). A critical assessment of the moist tamping technique. *ASTM geotechnical testing journal*, 26(1):57–70.
- Georgiannou, V., Tsomokos, A., and Stavrou, K. (2008). Monotonic and cyclic behaviour of sand under torsional loading. *Geotechnique*, 58(2):113–124.
- Gregersen, O. (1981). The quick clay landslide in rissa, norway. *NGI publication*, 135:1–6.

- Gudehus, G. (1996). A comprehensive constitutive equation for granular materials. *Soils and Foundations*, 36:1–12.
- Guimarães, L., Enyashin, A. N., Seifert, G., and Duarte, H. A. (2010). Structural, electronic, and mechanical properties of single-walled halloysite nanotube models. *The Journal of Physical Chemistry C*, 114(26):11358–11363.
- Gulliver, C., Houghton, B., and County, T. (1980). Omokoroa point land stability investigation. Technical report, Tonkin & Taylor.
- Guo, T. and Prakash, S. (1999). Liquefaction of silts and silt-clay mixtures. *Journal of Geotechnical and Geoenvironmental Engineering*, 125(8):706–710.
- Gylland, A. S. (2014). The effect of deformation rate in progressive slope failure. In *Landslides in Sensitive Clays*, pages 267–277. Springer.
- Hampton, M. A., Lee, H. J., and Locat, J. (1996). Submarine landslides. *Reviews of geophysics*, 34(1):33–59.
- Hepp, D. A., Hebbeln, D., Kreiter, S., Keil, H., Bathmann, C., Ehlers, J., and Mörz, T. (2012). An east-west-trending quaternary tunnel valley in the south-eastern north sea and its seismic-sedimentological interpretation. *Journal of Quaternary science*, 27:8:844–853.
- Herle, I. (1997). *Hypoplastizität und Granulometrie einfacher Korngerüste*. PhD thesis, Institut für Boden- und Felsmechanik der Universität Karlsruhe.
- Herle, I. and Gudehus, G. (1999). Determination of parameters of a hypoplastic constitutive model from properties of grain assemblies. *Mechanics of Cohesive-frictional Materials*, 4(5):461–486.
- Herle, I. and Mayer, P.-M. (1999). Verformungsberechnung einer unterwasserbetonbaugrube auf der grundlage hypoplastisch ermittelter parameter des berliner sandes. *Bautechnik*, 76(1):34–48.
- Hight, D., Böese, R., Butcher, A., Clayton, C., and Smith, P. (1992). Disturbance of the bothkennar clay prior to laboratory testing. *Géotechnique*, 42(2):199–217.
- Hsu, H.-H. and Huang, A.-B. (1999). Calibration of cone penetration test in sand. *Proceedings of the National Science Council, Republic of China. Part A, Physical science and engineering*, 23(5):579–590.
- Huang, A.-B. and Hsu, H.-H. (2005). Cone penetration tests under simulated field conditions. *Geotechnique*, 55(5):345–354.
- Hyde, A. and Brown, S. (1976). The plastic deformation of a silty clay under creep and repeated loading. *Geotechnique*, 26(1):173–184.
- Hyodo, M., Tanimizu, H., Yasufuku, N., and Murata, H. (1994a). Undrained cyclic and monotonic triaxial behaviour of saturated loose sand. *Soils and foundations*, 34(1):19–32.
- Hyodo, M., Yamamoto, Y., and Sugiyama, M. (1994b). Undrained cyclic shear behaviour of normally consolidated clay subjected to initial static shear stress. *Soils and Foundations*, 34(4):1–11.

- Idriss, I. (1985). Evaluating seismic risk in engineering practice. In *Proceedings of the eleventh international conference on soil mechanics and foundation engineering*. Balkema (AA).
- Idriss, I. and Boulanger, R. W. (2008). *Soil liquefaction during earthquakes*. Earthquake engineering research institute.
- Ishihara, K. (1985). Stability of natural deposits during earthquakes. In *Proceedings, 11th International Conference on Soil Mechanics and Foundation Engineering, San Francisco*, volume 1, pages 321–376.
- Israelachvili, J. N. (2011). *Intermolecular and Surface Forces (3rd Edition)*. Elsevier.
- Jacobsen, M. (1976). On pluvial compaction of sand. Technical report, Aalborg Universitetscenter, Inst. for Vand, Jord og Miljøteknik, Laboratoriet for Fundering.
- Jacquet, D. (1990). Sensitivity to remoulding of some volcanic ash soils in new zealand. *Engineering Geology*, 28(1):1–25.
- Jaky, J. (1948). Pressure in silos. In *Proceedings of the 2nd international conference on soil mechanics and foundation engineering*, volume 1, pages 103–107.
- Jang, D.-J. and Frost, J. D. (1998). Sand structure differences resulting from specimen preparation procedures. In *Geotechnical Earthquake Engineering and Soil Dynamics III*, pages 234–245. ASCE.
- Jardine, R., Overy, R., and Chow, F. (1998). Axial capacity of offshore piles in dense north sea sands. *Journal of geotechnical and geoenvironmental engineering*, 124(2):171–178.
- Jorat, M., Kreiter, S., Mörz, T., Moon, V., and de Lange, W. (2014a). Utilizing cone penetration tests for landslide evaluation. In *Submarine Mass Movements and Their Consequences*, pages 55–71. Springer.
- Jorat, M., Mörz, T., Schunn, W., and Kreiter (2014b). Geotechnical offshore seabed tool (gost): A new cone penetrometer. In *3rd International Symposium on Cone Penetration Testing, Las Vegas, Nevada, USA*.
- Jorat, M. E., Mörz, T., Moon, V., Kreiter, S., and de Lange, W. (2015). Utilizing piezovibrocone in marine soils at tauranga harbor, new zealand. *Journal of Geomechanics and Engineering*, 9(1):1–14.
- Joussein, E., Petit, S., Churchman, J., Theng, B., Righi, D., and Delvaux, B. (2005). Halloysite clay minerals—a review. *Clay Minerals*, 40(4):383–426.
- Juneja, A. and Raghunandan, M. (2010). Effect of sample preparation on strength of sands. *GEOTrendz, Indian Geotechnical Conference*.
- Kaiser, A., Holden, C., Beavan, J., Beetham, D., Benites, R., Celentano, A., Collett, D., Cousins, J., Cubrinovski, M., and Dellow, G. (2012). The mw 6.2 christchurch earthquake of february 2011: preliminary report. *New Zealand journal of geology and geophysics*, 55(1):67–90.

- Kerr, P. F. and Drew, I. M. (1968). Quick-clay slides in the usa. *Engineering Geology*, 2(4):215–238.
- Kirk, P., Campbell, S., Fletcher, C., and Merriman, R. (1997). The significance of primary volcanic fabrics and clay distribution in landslides in hong kong. *Journal of the Geological Society*, 154(6):1009–1019.
- Kirkman, J. H. (1981). Morphology and structure of halloysite in new zealand tephras. *Clays and Clay Minerals*, 29(1):1–9.
- Kluger, M. O. (2013). Hypoplastizität: Von der Parameterbestimmung bis zur numerischen Modellierung eines Cuxhavener Sandes. Master's thesis, University of Bremen.
- Kluger, M. O., Kreiter, S., Biryaltseva, T., and Mörz (2016a). Hypoplastic modeling of highly dense cuxhaven-sand with north sea subsoil characteristics. *Acta Geo*.
- Kluger, M. O., Kreiter, S., L'Heureux, J.-S., Stegmann, S., Moon, V., and Mörz, T. (2016b). In situ cyclic softening of marine silts by vibratory cptu at orkdalsfjord test site, mid norway. In *Submarine Mass Movements and their Consequences*, pages 201–209. Springer.
- Kluger, M. O., Moon, V. G., Kreiter, S., Lowe, D. J., Churchman, G., Hepp, D. A., Seibel, D., Jorat, M. E., and Mörz, T. (2017). A new attraction-detachment model for explaining flow sliding in clay-rich tephras. *Geology*, 42(2):131–134.
- Knudsen, K. L. (1988). Marine interglacial deposits in the Cuxhaven area, NW Germany: A comparison of Holsteinian, Eemian and Holocene foraminiferal faunas. *Geozon Science Media*.
- Kolymbas, D. (1978). *Ein nichtlineares viskoplastisches Stoffgesetz für Böden*. Institut für Bodenmechanik und Felsmechanik, Universität Fridericiana in Karlsruhe.
- Kolymbas, D. (1985). A generalized hypoplastic constitutive law. *Proceedings of the XI International Conference on Soil Mechanics and Foundation Engineering. San Francisco*, 5:2626.
- Kolymbas, D. (1988). *Eine konstitutive Theorie für Böden und andere körnige Stoffe*, volume 109. Institut für Bodenmechanik und Felsmechanik der Universität Fridericiana.
- Kolymbas, D. (2000). *Introduction to hypoplasticity*. Balkema.
- Kramer, S. (1996). *Geotechnical earthquake engineering*. Prentice–Hall international series in civil engineering and engineering mechanics. New Jersey.
- Kreiter, S., Hepp, D., Ossig, B., Hebig, J., Otto, D., Schlue, B., Mörz, T., and Kopf, A. (2010a). Cyclic soil parameters of complex offshore soils: a practical engineering perspective. In *Workshop Gründung von Offshore-Windenergieanlagen. Karlsruher Institut für Technologie, Karlsruhe*, pages 165–181.
- Kreiter, S., Moerz, T., Strasser, M., Lange, M., Schunn, W., Schlue, B., Otto, D., and Kopf, A. (2010b). Advanced dynamic soil testing—introducing the new marum dynamic triaxial testing device. In *Submarine Mass Movements and their Consequences*, pages 31–41. Springer.

- Kurup, P., Voyiadjis, G., and Tumay, M. (1994). Calibration chamber studies of piezocone test in cohesive soils. *Journal of Geotechnical Engineering*, 120(1):81–107.
- Kvalstad, T. J., Andresen, L., Forsberg, C. F., Berg, K., Bryn, P., and Wangen, M. (2005). The storegga slide: evaluation of triggering sources and slide mechanics. *Marine and Petroleum Geology*, 22(1):245–256.
- Ladd, R. (1978). Preparing test specimens using undercompaction. *Geotechnical Testing Journal, GTJODJ*, 1(1):16–23.
- Ladd, R. S. (1974). Specimen preparation and liquefaction of sands. *Journal of Geotechnical and Geoenvironmental Engineering*, 100(Proc. Paper 10857 Proceeding).
- Lagioia, R., Sanzeni, A., and Colleselli, F. (2006). Air, water and vacuum pluviation of sand specimens for the triaxial apparatus. *Soils and foundations*, 46(1):61–67.
- Lefebvre, G. and Leboeuf, D. (1987). Rate effects and cyclic loading of sensitive clays. *Journal of Geotechnical Engineering*, 113(5):476–489.
- Leroueil, S., Tavenas, F., Samson, L., and Morin, P. (1983). Preconsolidation pressure of champlain clays. part ii. laboratory determination. *Canadian Geotechnical Journal*, 20(4):803–816.
- L'Heureux, J.-S., Locat, A., Leroueil, S., Demers, D., and Locat, J. (2014a). Landslides in sensitive clays - from geosciences to risk management. In *Landslides in Sensitive Clays - From Geosciences to Risk Management*, pages 1–12. Springer.
- L'Heureux, J.-S., Longva, O., Hansen, L., and Vanneste, M. (2014b). The 1930 landslide in orkdalsfjorden: morphology and failure mechanism. In *Submarine Mass Movements and Their Consequences*, pages 239–247. Springer.
- Lo, K. (1969). The pore pressure-strain relationship of normally consolidated undisturbed clays: Part ii. experimental investigation and practical applications. *Canadian Geotechnical Journal*, 6(4):395–412.
- Lo, K. and Becker, D. (1979). Pore-pressure response beneath a ring foundation on clay. *Canadian Geotechnical Journal*, 16(3):551–566.
- Locat, A., Leroueil, S., Bernander, S., Demers, D., Jostad, H. P., and Ouehb, L. (2011). Progressive failures in eastern canadian and scandinavian sensitive clays. *Canadian Geotechnical Journal*, 48(11):1696–1712.
- Locat, J. and Leroueil, S. (1997). Landslide stages and risk assessment issues in sensitive clays and other soft sediments. In Cruden, D. and Fell., R., editors, *Proceedings of the International Workshop on Landslide Risk Assessment, Hawaii.*, pages 261–270. AA Balkema, Rotterdam, The Netherlands.
- Longva, O., Janbu, N., Blikra, L., and Bøe, R. (2003). *The 1996 Finneidfjord slide; seafloor failure and slide dynamics*, pages 531–538. Springer.
- Lowe, D. J. (1986). *Rates of chemical weathering of rocks and minerals*, chapter Controls on the rates of weathering and clay mineral genesis in airfall tephra: a review and New Zealand case study, pages 265–330. Elsevier.

- Lowe, D. J. (2011). Tephrochronology and its application: a review. *Quaternary Geochronology*, 6(2):107–153.
- Lunne, T. (2012). The fourth James K. Mitchell lecture: The CPT in offshore soil investigations—a historic perspective. *Geomechanics and Geoengineering*, 7(2):75–101.
- Lunne, T. and Andersen, K. H. (2007). Soft clay shear strength parameters for deepwater geotechnical design. In *Offshore Site Investigation and Geotechnics, Confronting New Challenges and Sharing Knowledge*. Society of Underwater Technology.
- Lunne, T., Berre, T., Andersen, K. H., Strandvik, S., and Sjørsen, M. (2006). Effects of sample disturbance and consolidation procedures on measured shear strength of soft marine Norwegian clays. *Canadian Geotechnical Journal*, 43(7):726–750.
- Lunne, T., Christoffersen, H. P., et al. (1983). Interpretation of cone penetrometer data for offshore sands. In *Offshore Technology Conference*. Offshore Technology Conference.
- Lunne, T. and Lacasse, S. (1999). Geotechnical characteristics of low plasticity Drammen clay. In Tsuchida, T. and Nakase, A., editors, *Proceedings of the International Symposium on Characterisation of Soft Marine Clays - Bothkennar, Drammen, Quebec and Ariake clays*, pages 33–56, Yokosuka, Japan. A. A. Balkema, Rotterdam, The Netherlands.
- Lunne, T., Long, M., and Forsberg, C. (2003). Characterisation and engineering properties of Onsøy clay. *Characterisation and Engineering Properties of Natural Soils*, 1:395–428.
- Lunne, T., Myrvoll, F., and Kjekstad, O. (1981). Observed settlements of five North Sea gravity platforms. In *Offshore Technology Conference*. Offshore Technology Conference.
- Lunne, T., Robertson, P., and Powell, J. (1997). Cone penetration testing. *Geotechnical Practice*.
- Matsuoka, H. and Nakai, T. (1974). Stress-deformation and strength characteristics of soil under three different principal stresses. In *Proc. JSCE*, volume 232, pages 59–70.
- McGregor, H. V., Dupont, L., Stuu, J.-B. W., and Kuhlmann, H. (2009). Vegetation change, goats, and religion: a 2000-year history of land use in southern Morocco. *Quaternary Science Reviews*, 28(15):1434–1448.
- Mills, P. and Moon, V. (2016). Static failure mechanisms in sensitive volcanic soils in the Tauranga region, New Zealand. In Neeson, F., Lacey, D., Buxton, D., and Storie, L., editors, *11th Australia and New Zealand Young Geotechnical Professionals Conference*, Queenstown, New Zealand. New Zealand Geotechnical Society.
- Mitchell, J. (1988). New developments in penetration tests and equipment. In *Proc 1st International Symposium on Penetration Testing, ISOPT-1*, pages 245–261, Orlando, Rotterdam: AA Balkema.
- Miura, S. and Toki, S. (1982). A sample preparation method and its effect on static and cyclic deformation-strength properties of sand. *Soils and Foundations*, 22(1):61–77.
- Miura, S., Yagi, K., and Asonuma, T. (2003). Deformation-strength evaluation of crushable volcanic soils by laboratory and in-situ testing. *Soils and Foundations*, 43(4):47–57.

- Mohamad, R. and Dobry, R. (1986). Undrained monotonic and cyclic triaxial strength of sand. *Journal of Geotechnical Engineering*, 112(10):941–958.
- Moon, V. (2016). Halloysite behaving badly: geomechanics and slope behaviour of halloysite-rich soils. *Clay Minerals*, 51(3):517–528.
- Moon, V., Cunningham, M., Wyatt, J. B., Lowe, D. J., Morz, T., and Jorat, M. (2013). Landslides in sensitive soils, tauranga, new zealand. In Chin, C., editor, *Proc. 19th NZGS Geotechnical Symposium*, pages 537–544, Queenstown.
- Moon, V., de Lange, W., Garae, C., Mörz, T., Jorat, M., and Kreiter, S. (2015a). Monitoring the landslide at bramley drive, tauranga, nz.
- Moon, V. G., Lowe, D. J., Cunningham, M. J., Wyatt, J. B., de Lange, W. P., Churchman, G. J., Mörz, T., Kreiter, S., Kluger, M. O., and Jorat, M. E. (2015b). Sensitive pyroclastic-derived halloysitic soils in northern new zealand: Interplay of microstructure, minerals, and geomechanics. *Volcanic Rocks and Soils*, pages 3–21.
- Morgenstern, N. and Price, V. E. (1965). The analysis of the stability of general slip surfaces.
- Muir Wood, D. (1990). *Soil behaviour and critical state soil mechanics*. Cambridge university press.
- Mulilis, J., Arulanandan, K., Mitchell, J., Chan, C., and Seed, H. (1977). Effects of sample preparation on sand liquefaction. *Journal of the Geotechnical Engineering Division*, 103(2):91–108.
- Naumann, M., Schnabel, C., Fritz, J., and Djuren, D. (2013). Erstellung von baugrundschnitten in der deutschen nordsee: Schnittzeichnungen vom 03.09.2012 - 23.04.2013. Technical report, Geopotenzial Deutsche Nordsee - Modul B: Dokumentation ; 9.
- Niemunis, A. and Herle, I. (1997). Hypoplastic model for cohesionless soils with elastic strain range. *Mechanics of Cohesive-frictional Materials*, 2(4):279–299.
- Norsk Geoteknisk Forening (1974). Retningslinjer for presentasjon av geotekniske undersøkelser.
- NZGS (2001). Guideline for hand held shear vane tests. New Zealand Geotechnical Society.
- NZS 4402.4.1.1:1986 (1986). Methods of testing soils for civil engineering purposes.
- Orense, R. and Pender, M. (2015). From micro to macro: An investigation of the geomechanical behaviour of pumice sand. *Volcanic Rocks and Soils*, page 45.
- Quigley, R. M. (1980). Geology, mineralogy, and geochemistry of canadian soft soils: a geotechnical perspective. *Canadian Geotechnical Journal*, 17(2):261–285.
- Randolph, M., Jamiolkowski, M., and Zdravkovic, L. (2004). Load carrying capacity of foundations. In *Proc. Skempton Memorial Conf., London*, volume 1, pages 207–240.
- Rankka, K., Andersson-Sköld, Y., Hultén, C., Larsson, R., Leroux, V., and Dahlin, T. (2004). Quick clay in sweden. *Swedish Geotechnical Institute Report*, 65:145.

- Reed, S. J. B. (2005). *Electron Microprobe Analysis and Scanning Electron Microscopy in Geology*. Cambridge University Press.
- Riecke, R., Meyerhoff, F., and Galal, G. (2012). Offshore großrohrrammpfähle - praktische nachweisführung der axialen pfahltragfähigkeiten im baufeld bard offshore 1. In *Vorträge zum 8. Hans Lorenz Symposium*, pages 149–164. TU Berlin, Grundbauinstitut.
- Robertson, P. and Campanella, R. (1983). Interpretation of cone penetration tests. Part I: Sand. *Canadian Geotechnical Journal*, 20(4):718–733.
- Robertson, P. and Wride, C. (1998). Evaluating cyclic liquefaction potential using the cone penetration test. *Canadian Geotechnical Journal*, 35(3):442–459.
- Rondón, H., Wichtmann, T., Triantafyllidis, T., and Lizcano, A. (2007). Hypoplastic material constants for a well-graded granular material for base and subbase layers of flexible pavements. *Acta Geotechnica*, 2(2):113–126.
- Rosenqvist, I. T. (1953). Considerations on the sensitivity of norwegian quick-clays. *Geotechnique*, 3(5):195–200.
- Rosenqvist, I. T. (1966). Norwegian research into the properties of quick clay—a review. *Engineering Geology*, 1(6):445–450.
- Rowe, P. (1969). The relation between the shear strength of sands in triaxial compression, plane strain and direct. *Geotechnique*, 19(1):75–86.
- Sangrey, D. (1972). Naturally cemented sensitive soils. *Geotechnique*, 22(1):139–152.
- Sangrey, D., Henkel, D., and Esrig, M. (1969). The effective stress response of a saturated clay soil to repeated loading. *Canadian Geotechnical Journal*, 6(3):241–252.
- Sasaki, Y., Itoh, Y., and Shimazu, T. (1974). A study on the relationship between the results of vibratory cone penetration tests and earthquake-induced settlement of embankments. In *Proceedings, 19th annual meeting of JSSMFE, Tokyo, Japan*.
- Sasaki, Y., Itoh, Y., and Shimazu, T. (1984). A study on the relationship between the results of vibratory cone penetration tests and earthquake-induced settlement of embankments. In *Proceedings, 19th annual meeting of JSSMFE, Tokyo, Japan*.
- Seed, H. B., Idriss, I., and Arango, I. (1983). Evaluation of liquefaction potential using field performance data. *Journal of Geotechnical Engineering*, 109(3):458–482.
- Seed, H. B. and Idriss, I. M. (1971). Simplified procedure for evaluating soil liquefaction potential. *Journal of Soil Mechanics & Foundations Div*, 97(9):1249–1273.
- Seibel, D. (2015). *Einfluss der Halloysit-Morphologie auf die undrainierte Scherfestigkeit der Pahoia Tephra Neuseelands - Ein Vergleich von REM-Aufnahmen und Flügelsondenversuchen*. PhD thesis, University of Bremen.
- Sindowski, K.-H. (1963). Die drenthestadiale Altenwalder Stauchmoräne südlich Cuxhaven (Beitrag zum Punkt 1 Hohe Lieth der Exkursion B der Frühjahrstagung der Deutschen Geologischen Gesellschaft in Cuxhaven 1963.). *Zeitschrift der Deutschen Geologischen Gesellschaft*, 115:158–162.

- Singh, S. (1996). Liquefaction characteristics of silts. *Geotechnical & Geological Engineering*, 14(1):1–19.
- Skempton, A. (1953). Soil mechanics in relation to geology. *Proceedings of the Yorkshire Geological Society*, 29(1):33–62.
- Skempton, A. and Northey, R. (1952). The sensitivity of clays. *Geotechnique*, 3(1):30–53.
- Small, C. and Nicholls, R. J. (2003). A global analysis of human settlement in coastal zones. *Journal of Coastal Research*, pages 584–599.
- Smalley, I. (1971). Nature of quickclays. *Nature*, 231(310).
- Smalley, I., Ross, C. W., and Whitton, J. (1980). Clays from new zealand support the inactive particle theory of soil sensitivity. *Nature*, 288:576–577.
- Solberg, I.-L., Rønning, J. S., Dalsegg, E., Hansen, L., Rokoengen, K., and Sandven, R. (2008). Resistivity measurements as a tool for outlining quick-clay extent and valley-fill stratigraphy: a feasibility study from buvika, central norway. *Canadian Geotechnical Journal*, 45(2):210–225.
- Stegmann, S., Baeten, N., Fleischmann, T., Kluger, M., Kreiter, S., Lange, M., Li, W., Roskoden, R., Rösner, A., Schunn, W., and Völker, D. (2017). Report and preliminary results of rv poseidon expedition pos472 norgeotech. Technical report, University Bremen.
- Steiner, A., Kopf, A. J., L'Heureux, J.-S., Kreiter, S., Stegmann, S., Hafliadason, H., and Moerz, T. (2013). In situ dynamic piezocone penetrometer tests in natural clayey soils—a reappraisal of strain-rate corrections. *Canadian Geotechnical Journal*, 51(3):272–288.
- Susila, E. and Hryciw, R. (2003). Large displacement FEM modelling of the cone penetration test (CPT) in normally consolidated sand. *International Journal for Numerical and Analytical Methods in Geomechanics*, 27(7):585–602.
- Tanaka, K. (1992). Slope hazards and clay minerals. *Nendo Kagaku*, 32(1):16–22.
- Tavenas, F. (1984). Landslides in canadian sensitive clays—a state-of-the-art. In *Proceedings of the 4th International Symposium on Landslides, Toronto, Ont*, pages 16–21.
- Terzaghi, K. (1944). *Ends and Means in Soil Mechanics*. Harvard University.
- Terzaghi, K., Peck, R. B., and Mesri, G. (1996). *Soil mechanics in engineering practice*. John Wiley & Sons.
- Tokimatsu, K. (1988). Penetration tests for dynamic problems. In *Proc 1st International Symposium on Penetration Testing, ISOPT-1*, pages 117–136, Orlando. Rotterdam: AA Balkema.
- Torrance, J. K. (1983). Towards a general model of quick clay development. *Sedimentology*, 30(4):547–555.
- Torrance, J. K. (1992). Discussion on sensitivity to remoulding of some volcanic ash soils in new zealand, by d. jacquet. *Engineering Geology*, 32(1):101–105.

- Udden, J. A. (1914). Mechanical composition of clastic sediments. *Geological Society of America Bulletin*, 25(1):655–744.
- Updike, R. G. and Carpenter, B. A. (1986). *Engineering geology of the government hill area, Anchorage, Alaska*. Department of the Interior, US Geological Survey.
- Vaid, Y. P., Sivathayalan, S., and Stedman, D. (1999). Influence of specimen-reconstituting method on the undrained response of sand. *ASTM geotechnical testing journal*, 22(3):187–195.
- Varnes, D. J. (1978). Slope movement types and processes. *Special report*, 176:11–33.
- Vogt, C., Lauterjung, J., and Fischer, R. X. (2002). Investigation of the clay fraction (< 2  $\mu\text{m}$ ) of the clay minerals society reference clays. *Clays and Clay Minerals*, 50(3):388–400.
- von Wolffersdorff, P. A. (1996). A hypoplastic relation for granular materials with a predefined limit state surface. *Mechanics of cohesive-frictional materials*, 1:251–271.
- Wada, S.-I., Aoki, K., and Wada, K. (1977). The interior structure of spherical halloysite particles. *Clay Science*, 5(2):113–121.
- Weifner, T. and Kolymbas, D. (2007). A hypoplastic model for clay and sand. *Acta Geotechnica*, 2(2):103–112.
- Wentworth, C. K. (1922). A scale of grade and class terms for clastic sediments. *The Journal of Geology*, 30(5):377–392.
- Wesley, L. (1973). Some basic engineering properties of halloysite and allophane clays in java, indonesia. *Geotechnique*, 23(4):471–494.
- Wesley, L. (1977). Shear strength properties of halloysite and allophane clays in java, indonesia. *Geotechnique*, 27(2):125–136.
- Wichtmann, T. (2005a). *Explicit accumulation model for non-cohesive soils under cyclic loading*. PhD thesis, Institut für Grundbau und Bodenmechanik der Ruhr-Universität Bochum.
- Wichtmann, T. (2005b). *Explicit accumulation model for non-cohesive soils under cyclic loading*. Inst. für Grundbau und Bodenmechanik.
- Wichtmann, T., Andersen, K., Sjørusen, M., and Berre, T. (2013). Cyclic tests on high-quality undisturbed block samples of soft marine norwegian clay. *Canadian Geotechnical Journal*, 50(4):400–412.
- Wichtmann, T., Niemunis, A., and Triantafyllidis, T. I. (2010). Recent improvements of a high-cycle accumulation model for sand. In *Workshop "Gründung von Offshore-Windenergieanlagen"*, Karlsruhe, pages 35–47.
- Wieczorek, G. F., Jibson, R., Wilson, R., and Buchanan-Banks, J. (1982). Geotechnical properties of ash deposits near hilo, hawaii. Report 2331-1258, US Geological Survey.
- Wiemer, G. and Kopf, A. (2016). On the role of volcanic ash deposits as preferential submarine slope failure planes. *Landslides*, pages 1–10.

- Wienbroer, H. and Zachert, H. (2010). Modellversuche zur Verformungsakkumulation einer zyklisch belasteten Flachgründung. In *Workshop "Gründung von Offshore-Windenergieanlagen"*, Karlsruhe, pages 65–79.
- Wise, C., Mayne, P., and Schneider, J. (1999). Prototype piezovibrocone for evaluating soil liquefaction susceptibility. *Geotech Earthquake Engineering*, 2:537–542.
- Witt, K. J. (2008). *Grundbau - Taschenbuch. Teil 1: Geotechnische Grundlagen. 7. Auflage.* Ernst und Sohn.
- Wood, F. M., Yamamuro, J. A., and Lade, P. V. (2008). Effect of depositional method on the undrained response of silty sand. *Canadian Geotechnical Journal*, 45(11):1525–1537.
- Wu, W., Bauer, E., and Kolymbas, D. (1996). Hypoplastic constitutive model with critical state for granular materials. *Mechanics of materials*, 23(1):45–69.
- Yamamuro, J. A. and Wood, F. M. (2004). Effect of depositional method on the undrained behavior and microstructure of sand with silt. *Soil Dynamics and Earthquake Engineering*, 24(9):751–760.
- Yasuhara, K., Hirao, K., and Hyde, A. F. (1992). Effects of cyclic loading on undrained strength and compressibility of clay. *Soils and Foundations*, 32(1):100–116.
- Yoshimoto, N., Orense, R. P., Hyodo, M., and Nakata, Y. (2013). Dynamic behavior of granulated coal ash during earthquakes. *Journal of Geotechnical and Geoenvironmental Engineering*, 140(2):04013002.
- Youd, T., Idriss, I., Andrus, R. D., Arango, I., Castro, G., Christian, J. T., Dobry, R., Finn, W. L., Harder Jr, L. F., and Hynes, M. E. (2001). Liquefaction resistance of soils: summary report from the 1996 nceer and 1998 nceer/nsf workshops on evaluation of liquefaction resistance of soils. *Journal of geotechnical and geoenvironmental engineering*, 127(10):817–833.
- Zergoun, M. and Vaid, Y. (1994). Effective stress response of clay to undrained cyclic loading. *Canadian Geotechnical Journal*, 31(5):714–727.

# Appendix A

## Conferences

- Moon, V.; Lowe, D.J. G.; Cunningham, M.J.; Wyatt, J.B.; de Lange, W.P.; Churchmann, G.J.; Mörz, T.; Kreiter, S.; **Kluger, M.O.**; Jorat, M.E. (2015): Sensitive pyroclastic-derived halloysitic soils in northern New Zealand: Interplay of microstructure, minerals, and geomechanics. Keynote lecture, Volcanic Rocks and Soils. 3-21
- **Kluger, M.O.**; Kreiter, S.; L'Heureux, J.-S.; Stegmann, S.; Moon, V.; Mörz, T. (2015): In situ cyclic softening of marine silts by vibratory CPTU at Orkdalsfjord test site, mid Norway. Presentation, 7th Symposium on Submarine Mass Movements and Their Consequences, Wellington, November 2015
- Lowe, D.J.; Loame, R.C.; Moon, V.G.; **Kluger, M.O.**; Villamor, P.; de Lange, W.P.; Vandergoes, M.J.; Rees, A.B.H.; Davies, S.M.; Johnston, R.; Mörz, T. (2016): Tephra seismites: a new tool to evaluate, date, map, and model paleoseismicity using tephra liquefaction in c. 20,000-year-old lake sediments in the Waikato region, New Zealand. Presentation Abstracts, Australasian Quaternary Association (AQUA) Biennial Conference “Quaternary Perspectives from the City of Volcanoes”, University of Auckland, Auckland, 5-9 December, 2016, p. 100.
- Lowe, D.J.; **Kluger, M.O.**; Moon, V.G.; Kreiter, S.; Churchman, G.J.; Hepp, D.A.; Seibel, D.; Jorat, M.E.; Mörz, T. (2016): A new attraction-detachment model for explaining landsliding in clay-rich Quaternary tephra, eastern North Island, New Zealand. Poster Abstracts, Australasian Quaternary Association (AQUA) Biennial Conference “Quaternary Perspectives from the City of Volcanoes”, University of Auckland, Auckland, 5-9 December, 2016, p. 99.
- **Kluger, M.O.**; Moon, G.V.; Kreiter, S.; Lowe, D.J.; Churchman, G.J.; Hepp, D.A.; Seibel, D.; Jorat, E.; Mörz, T. (2016): A new attraction-disseverance model for

explaining landsliding in clay-rich tephtras. Poster Abstracts, AGU Fall Meeting 2016, 12.-16. December 2016

- **Kluger, M.O.**; Moon, V.; Kreiter, S.; Lowe, D.J.; Churchman, G.J.; Hepp, E.J.; Mörz, T. (accepted) Tale of the unexpected: How halloysite predisposes flow sliding. Presentation Abstracts, XVI International Clay Conference, 2017, Granada. Spain

# Appendix B

## Abstracts

### **B.1 A new attraction-disseverance model for explaining landsliding in clay-rich tephras**

**Max O. Kluger<sup>1</sup>, Vicki G. Moon<sup>2</sup>, Stefan Kreiter<sup>1</sup>, David J. Lowe<sup>2</sup>, G.J. Churchman<sup>3</sup>, Daniel A. Hepp<sup>1</sup>, David Seibel<sup>1</sup>, M. Ehsan Jorat<sup>4</sup>, and Tobias Mörz<sup>1</sup>**

<sup>1</sup>MARUM–Center for Marine Environmental Sciences, University of Bremen, Leobener Straße, 28359 Bremen, Germany

<sup>2</sup>School of Science, University of Waikato, Private Bag 3105, Hamilton 3240, New Zealand

<sup>3</sup>School of Agriculture, Food and Wine, University of Adelaide, Adelaide, SA 5005, Australia

<sup>4</sup>School of Science, Engineering and Technology, Abertay University, Dundee DD11HG, UK

Poster at the *AGU Fall Meeting*, December 2016, San Francisco, CA, USA

### **Abstract**

Altered tephras are highly susceptible to landsliding and account for fatalities and property damage every year. The clay mineral halloysite is often associated with landslide-prone layers within weathered tephra successions, especially in deposits with high sensitivity, which describes the post-failure strength loss. However, the precise role of halloysite on the development of sensitivity and thus sudden and unpredictable landsliding is unknown. Here we show

that an abundance of halloysite, dominated by a distinctive ovate mushroom-cap-shaped (MCS) spherical morphology, governs the development of sensitivity, and hence proneness to landsliding, in weathered rhyolitic tephras in eastern North Island, New Zealand. We found that a highly sensitive layer, which was involved in a retrogressive landslide, has an extraordinarily high content of aggregated MCS spheres with imperfectly-closed exterior surfaces, i.e., the MCS spheres have substantial openings on one side. We suggest that short-range electrostatic and van der Waals' interactions enabled the MCS spheres to form interconnected aggregates by attraction between numerous paired silanol and aluminol layers with a weakly positive, or neutral, charge exposed in the openings and the negatively-charged convex silanol faces on the curved exterior surfaces of the spheres. However, if these weak attractions are overcome during slope failure, the prevailing repulsion between two exterior surfaces result in a low remolded shear strength, i.e., a high sensitivity, and thus a high propensity for flow-like landsliding. Our results indicate that this novel electrostatic attraction-disseverance model explains the high sensitivity and therefore contributes to a general understanding of the mechanisms of landsliding in sensitive altered tephras rich in spherical halloysite.

## **B.2 A new attraction-detachment model for explaining landsliding in clay-rich Quaternary tephras, eastern North Island, New Zealand**

**David J. Lowe<sup>1</sup>, Max O. Kluger<sup>2</sup>, Vicki G. Moon<sup>1</sup>, Stefan Kreiter<sup>2</sup>, G.J. Churchman<sup>3</sup>, Daniel A. Hepp<sup>2</sup>, David Seibel<sup>2</sup>, M. Ehsan Jorat<sup>4</sup>, and Tobias Mörz<sup>2</sup>**

<sup>1</sup>School of Science, University of Waikato, Private Bag 3105, Hamilton 3240, New Zealand

<sup>2</sup>MARUM—Center for Marine Environmental Sciences, University of Bremen, Leobener Straße, 28359 Bremen, Germany

<sup>3</sup>School of Agriculture, Food and Wine, University of Adelaide, Adelaide, SA 5005, Australia

<sup>4</sup>School of Science, Engineering and Technology, Abertay University, Dundee DD11HG, UK

Oral presentation at the *Australasian Quaternary Association (AQUA) 2016 biennial meeting*, December 2016, Auckland, New Zealand

## Abstract

Altered tephra deposits are highly susceptible to landsliding. Halloysite, a low-activity, 1:1 aluminosilicate clay mineral, is often associated with landslide-prone layers within weathered-tephra successions, especially in deposits with high sensitivity, which describes post-failure strength loss. However, the precise role that halloysite plays in the development of sensitivity and thus in sudden and unpredictable landsliding, is unknown. We show that an abundance of halloysite, dominated by a distinctive mushroom-cap-shaped (MCS) spheroidal morphology, governs the development of sensitivity, and hence proneness to landsliding, in weathered rhyolitic tephra <0.93 Ma in the Tauranga region, eastern North Island, New Zealand. We found that a highly sensitive tephra layer, which was involved in a landslide, has a high content of aggregated MCS spheroids with imperfectly-closed exterior surfaces, i.e., the spheroids have substantial openings on one side. We suggest that short-range electrostatic and van der Waals' interactions enabled the MCS spheroids to form interconnected aggregates by attraction between the edges of numerous paired silanol and aluminol sheets that are exposed in the openings and the convex silanol faces on the exterior surfaces of adjacent MCS spheroids. If these weak attractions are overcome during slope failure, multiple, weakly-attracted MCS spheroids can be separated from one another and the prevailing repulsion between exterior MCS surfaces results in low remolded shear strength, high sensitivity, and high propensity for flow-like landsliding. Our evidence indicates that the proposed electrostatic attraction-detachment model explains the high sensitivity and helps understanding of the mechanisms of landsliding in sensitive, altered tephra rich in spheroidal halloysite.

## B.3 Tale of the unexpected: How halloysite predisposes flow sliding

**Max O. Kluger<sup>1</sup>, Vicki G. Moon<sup>2</sup>, Stefan Kreiter<sup>1</sup>, David J. Lowe<sup>2</sup>, G.J. Churchman<sup>3</sup>, Daniel A. Hepp<sup>1</sup>, and Tobias Mörz<sup>1</sup>**

<sup>1</sup>MARUM—Center for Marine Environmental Sciences, University of Bremen, Leobener Straße, 28359 Bremen, Germany

<sup>2</sup>School of Science, University of Waikato, Private Bag 3105, Hamilton 3240, New Zealand

<sup>3</sup>School of Agriculture, Food and Wine, University of Adelaide, Adelaide, SA 5005, Australia

Oral presentation accepted at the *16th International Clay Conference*, 2017, Granada, Spain

## **Abstract**

In many regions around the world, tephra from volcanic eruptions cover wide areas of the landscape. With time, the primary constituents of tephra may alter to the low-activity clay mineral halloysite, which has often been associated with layers that are susceptible to damaging and unpredictable flow slides. However, the precise role of halloysite in the development of the high mobility during landsliding is unknown. In this study (Kluger et al., 2017), a succession of altered tephra was analysed, having been involved in a recent flow slide in North Island, New Zealand. We found a new open-sided spheroidal halloysite particle shape in the form of “mushroom caps” that apparently governed the development of high mobility in the failure zone during landsliding. We suggest that the rearrangement in the halloysite texture during the failure process reduced the attractions between the particles at nanoscale dimensions and thus predisposed flow sliding. Our findings contribute to an improved understanding of the mechanisms of flow sliding in altered tephra rich in halloysite.

# Appendix C

## Hypoplastic modeling of high-density Cuxhaven-Sand as a North Sea subsoil analogue

Max O. Kluger<sup>1</sup>, Stefan Kreiter<sup>1</sup>, Taisiya Biryaltseva<sup>2</sup>, Vicki G. Moon<sup>3</sup>, and Tobias Mörz<sup>1</sup>

<sup>1</sup>MARUM–Center for Marine Environmental Sciences, University of Bremen, Leobener Straße, 28359 Bremen, Germany

<sup>2</sup>Fraunhofer Institute for Wind Energy and Energy System Technology (IWES), 28359 Bremen, Germany

<sup>3</sup>School of Science, University of Waikato, Private Bag 3105, Hamilton 3240, New Zealand

In preparation for submission to *International Journal of Geomechanics*

### Abstract

Granular soils which exhibit plastic behavior and large volume change under shear stress can be described by hypoplastic models, which are useful for predicting tilting of offshore foundations. The Cuxhaven-Sand is similar to dense North Sea subsoil and is therefore an important analogue material in studies dealing with cone penetration tests and innovative foundation design like gravity foundations or suction buckets. In the present study hypoplastic constants are determined for Cuxhaven-Sand from geotechnical laboratory experiments to serve as constraints for future finite element modeling studies. Special focus

was given to investigating the influence of different sample reconstitutions on parameter determination and on the hypoplastic model predictions for dense Cuxhaven-Sand regarding initial tangent modulus, peak shear strength and volume change. The most appropriate sample reconstitution seems to be dry pluviation whereas moist tamping and lateral tapping are not ideal for soil homogeneity and affect the peak state response. The hypoplastic model is appropriate for describing results of cone penetration tests in Cuxhaven-Sand. For the design of gravity-based foundations the model is only useful in cases of uniaxial compression, because without lateral constraints, the prediction of small strain behavior is limited.

**Keywords** Cuxhaven-Sand · Sample reconstitution · Hypoplastic constants · Peak strength · Volume change

## C.1 Introduction

Offshore wind power foundations are affected by static as well as cyclic loads, possibly exceeding the serviceability limits of offshore foundations during long term operation. In Northern Germany special interest lies in characterizing the destabilization process of offshore wind foundations due to cyclic loads from operation, wind and waves (Wichtmann et al., 2010; Wienbroer and Zachert, 2010). Tilting of offshore structures is often induced by differential settling (Randolph et al., 2004). The theory of hypoplasticity, first introduced by Kolymbas (1985), is one possible approach to model the stress-strain behavior of granular soils bearing offshore wind foundations (Anaraki, 2008). The in situ relative density is the most important state parameter for such hypoplastic simulations, which for North Sea subsoil are derived from cone penetration tests (CPT) using correlations from calibration chamber studies (Lunne et al., 1983; Robertson and Campanella, 1983; Kurup et al., 1994; Hsu and Huang, 1999; Huang and Hsu, 2005; Bałachowski, 2006). During the Cenozoic, wide areas of the today's North Sea were covered by large ice sheets (Ehlers et al., 2004) inducing overloading stress into the subsoil. As a consequence, North Sea sands are very dense and have extremely high cone resistances of up to 100 MPa (Jardine et al., 1998; Kreiter et al., 2010a; Achmus, 2010), which is well beyond the defined upper limit of the current DIN-EN standard of 25 MPa cone resistance for the same relative density (DIN EN 1997-1/NA:2010-12, 2010). However, the DIN-EN standard uses a constant relative density for all cone resistances higher than 25 MPa, so the strength limitations of high-density sediments cannot reliably be evaluated. In a CPT-calibration chamber project (Fleischer et al., 2016) it is planned to model cone penetration tests, cone calibration chamber tests and settlement of offshore gravity-based foundations with the hypoplastic constitutive equation by von

Wolffersdorff (1996) to provide a robust regional correlation for cone resistances and relative densities higher than the DIN-EN limit. The deformation during these two scenarios are quite different; while a cone penetration test induces higher shear stresses and shear failure (Susila and Hryciw, 2003), the construction of an offshore gravity-based foundation causes a normal stress increase, settlement and relatively low shear stress increases (Lunne et al., 1981; Das, 2010). A precise method of describing the mechanical behavior of sediments under a wide range of conditions is therefore needed to allow realistic modeling of gravitationally-loaded foundation sands from the North Sea with high cone resistance. Here, we consider the foundation sand as a hypoplastic material and calculate the hypoplastic parameters following Herle and Gudehus (1999), which uses limit void ratios, sand cone pluviation and oedometric and triaxial compression tests on reconstituted specimens. The stress-strain response of granular materials is highly affected by the applied sample reconstitution (Mulilis et al., 1977; Della et al., 2014), however, a standard procedure for preparing dense triaxial samples for the hypoplastic parameter determination has not yet been developed.

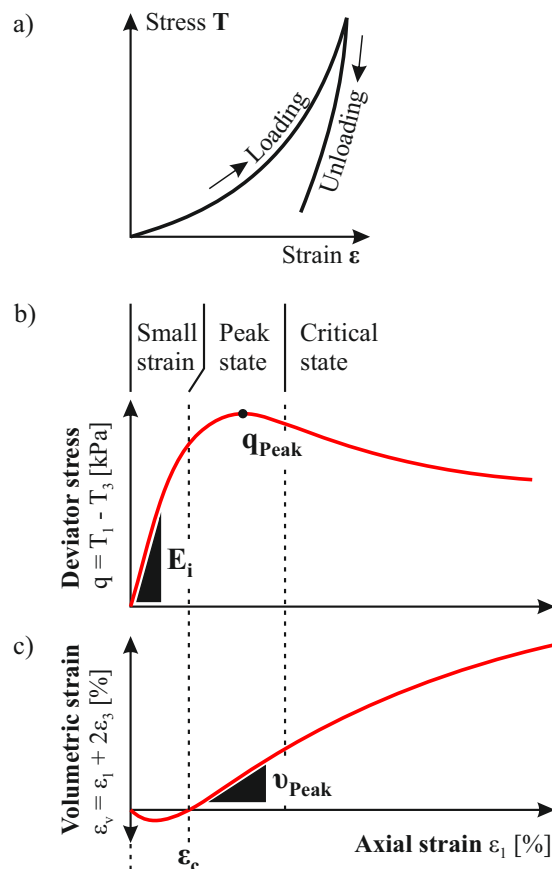


Fig. C.1 a) General stress-strain relationship of granular materials. b) Schematic deviator stress and c) Volumetric strain curves for dense granular materials.

The reconstitution of both dense and homogeneous sand specimens for triaxial testing is challenging and may vary in terms of moisture conditions, soil emplacement and treatment after soil is placed (Della et al., 2014), where tamping, lateral tapping and pluviation are the predominant methods. Tamping is either conducted under dry (Ezaoui and Di Benedetto, 2009), moist (Ladd, 1974; Mulilis et al., 1977; Ladd, 1978; DeGregorio, 1990; Vaid et al., 1999; Frost and Park, 2003; Rondón et al., 2007; Della et al., 2014) or submerged (Juneja and Raghunandan, 2010) conditions using a proctor hammer or tamper which induces additional compaction into the soil specimen. The high initial densities that can be achieved with tamping are accompanied by inhomogeneous soil fabrics (Jang and Frost, 1998) often leading to shear band formation during triaxial testing (Rondón et al., 2007). Frost and Park (2003) investigated uniformity and amount of energy applied to each soil layer and discovered the development of layering with large internal deviations of relative density. The authors further postulated that the applied stresses are sometimes even higher than typical consolidation stresses. Consequently, tamped soil specimens exhibit high stiffness in vertical direction (Ezaoui and Di Benedetto, 2009), which are undesirable in laboratory element tests (Vaid et al., 1999; Frost and Park, 2003). With lateral tapping techniques (DeGregorio, 1990; Anaraki, 2008; Ezaoui and Di Benedetto, 2009; Della et al., 2014) additional energy is applied by lateral blows on sample mold resulting in horizontal stiffness increase (Ezaoui and Di Benedetto, 2009). Laterally tapped specimens tend to exhibit bulged-shaped deformation or exhibit shear bands when reaching failure (Anaraki, 2008). Pluviation techniques are widely used to steadily rain sand into the sample mold through the air (Jacobsen, 1976; Miura and Toki, 1982; DeGregorio, 1990; Wichtmann, 2005a; Wood et al., 2008; Juneja and Raghunandan, 2010), water (Vaid et al., 1999; Yamamuro and Wood, 2004; Juneja and Raghunandan, 2010) or more recently through vacuum (Lagioia et al., 2006). The density is controlled by sand flow rate and fall height (Yamamuro and Wood, 2004; Wood et al., 2008) producing homogeneous specimens (Jang and Frost, 1998; Frost and Park, 2003) with large density ranges (Jacobsen, 1976; Miura and Toki, 1982). The medium in which the sand is pluviated has effects on the soil fabric. Air pluviated sand specimens exhibit highly reproducible samples (Miura and Toki, 1982) with uniform density distribution with depth (Frost and Park, 2003). Vaid et al. (1999), however, recommends water pluviation as it resembles naturally deposited alluvial fill sands and therefore more accurately reproduces in situ sample characteristics. Although water pluviation is capable of forming homogeneous specimens it is not possible to achieve high densities (Lagioia et al., 2006). For large densities near the densest state Lagioia et al. (2006) suggest vacuum pluviation. The absence of air results in a more uniform sand rain with less turbulence providing better homogeneity compared to air pluviation (Lagioia et al., 2006).

In this study we investigate how vacuum pluviation, moist tamping, and lateral tapping influence the triaxial stress-strain response and therefore the hypoplastic parameters of high-density Cuxhaven-Sand. Furthermore, the performance of the hypoplastic model is studied regarding the simulation of cone penetration tests and the deformation behavior below gravity-based foundations in Cuxhaven-Sand.

## C.2 Hypoplasticity

Granular materials are known to exhibit plastic behavior often without hardly any elastic range (Muir Wood, 1990; Witt, 2008). Their stiffness increases with mean effective stress showing an even greater incremental stiffness during unloading (Fig. C.1a). After unloading a considerable amount of non-recoverable strain remains in the soil fabric which is accompanied by large volumetric strain.

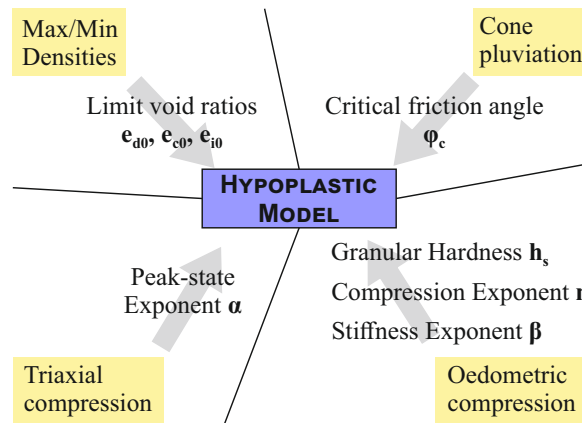


Fig. C.2 Sketch of hypoplastic parameter determination.

In triaxial compression of dense sands the deviator stress curves  $q(\varepsilon_1)$  exhibit high initial tangent modulus  $E_i = \Delta q_{,i} / \Delta \varepsilon_{1,i}$  and high peak strength  $q_{Peak}$  (Fig. C.1b). In the volumetric strain diagram  $\varepsilon_v(\varepsilon_1)$  this is accompanied by a distinct range of contraction  $\varepsilon_c$  and a high angle of peak dilatancy  $\nu_{Peak}$  (Fig. C.1c). The non-linearity, irreversibility and load anisotropy visible in Fig. C.1 is described by hypoplastic constitutive equations (Kolymbas, 1978, 1988; von Wolffersdorff, 1996; Wu et al., 1996; Niemunis and Herle, 1997; Weifner and Kolymbas, 2007). Hypoplastic models are incremental non-linear equations of rate type, valid for rate independent materials (Kolymbas, 2000). The theory of hypoplasticity is an alternative to elasto-plasticity for modeling the behavior of granular materials. Compared to elasto-plasticity the stress-strain curve is not separated into an elastic and plastic portion.

Hypoplasticity uses different state parameters without yield surfaces, flow rules and consistency conditions (Kolymbas, 1988; von Wolffersdorff, 1996). Even though there are common state parameters like stress and strain in the hypoplastic and elastic-plastic constitutive equations, in hypoplasticity the sign convention is taken from continuum mechanics where tensile stresses and strains are positive. The hypoplastic model by von Wolffersdorff (1996) is a single element approach that uses the actual strain rate tensor  $\mathbf{D}$  ( $\equiv \dot{\boldsymbol{\epsilon}}$ ) and two state variables - the actual stress tensor  $\mathbf{T}$  and void ratio  $e$ , to calculate the stress rate tensor  $\dot{\mathbf{T}}$  which is constant over the entire sample. Its general tensor form is written after Bauer (1996); Gudehus (1996) as:

$$\dot{\mathbf{T}} = \mathcal{L}(\mathbf{T}, e) : \mathbf{D} + \mathbf{N}(\mathbf{T}, e) \|\mathbf{D}\| \quad (\text{C.1})$$

Eq. C.1 is composed of a linear and non-linear portion, expressed by two tensor functions  $\mathcal{L}$  and  $\mathbf{N}$  (See appendix C.7 for details). Tensor functions  $\mathcal{L}$  and  $\mathbf{N}$  include eight material constants  $\varphi_c$ ,  $h_s$ ,  $n$ ,  $e_{d0}$ ,  $e_{c0}$ ,  $e_{i0}$ ,  $\alpha$  and  $\beta$  that are obtained from geotechnical laboratory tests following a procedure proposed by Herle and Gudehus (1999) (Fig. C.2, App. C.7). Thereby  $\varphi_c$  is the critical friction angle obtained from sand cone pluviation. The granular hardness  $h_s$  and the compression exponent  $n$  describe the decrease of void ratio with increasing mean stress  $p = (T_1 + 2T_3)/3$ .  $e_{d0}$ ,  $e_{c0}$ ,  $e_{i0}$  are the limit void ratios at densest, critical and loosest but stress free state ( $p = 0$ ). The exponent  $\alpha$  controls the influence of the initial void ratio  $e_i$  on the peak friction angle  $\varphi_p$ . The exponent  $\beta$  affects an increase of the stress rate with increasing density.

Niemunis and Herle (1997) added the intergranular strain to the hypoplastic model proposed by von Wolffersdorff (1996). Supplementary constants eliminate the ratcheting effect that arises in the soil fabric when the direction of deformation is reversed. In this study only static compression experiments are conducted, hence, the extension with intergranular strain is not considered.

The predictive efficiency of the hypoplastic model was investigated in many studies (von Wolffersdorff, 1996; Herle, 1997; Wichtmann, 2005a; Rondón et al., 2007; Anaraki, 2008; Chatra and Dadagoudar, 2010). Sensitivity and multiparameter analyses (Herle, 1997; Anaraki, 2008) explored the influences of hypoplastic constants on the general triaxial and oedometric stress-strain response. Thus far, not much emphasize has been given to pinpoint the model prediction for peak state and small strain behavior. In this study we analyze the peak state prediction with respect to peak shear strength and peak angle of dilatancy. In addition, the initial tangent modulus and the small strain contraction behavior are studied.



Table C.1 Grain size moments of the Cuxhaven-Sand.

Material	Mean $\bar{X}$ [ $\mu m$ ]	Sorting $\sigma$ [ $\mu m$ ]	Skewness $Sk$ [ $\mu m$ ]	Kurtosis $K$ [ $\mu m$ ]
Cuxhaven-Sand	231.15	1.86	-0.39	8.21

Naumann et al., 2013; Achmus, 2010). From this interval an amount of 4 t material was sampled and homogenized, to be used as an analogue of North Sea subsoil.

Based on binocular microscopy the Cuxhaven-Sand is composed almost entirely of quartz (> 95%) with sub-angular to angular grains following classification of Folk (2002). From grain size distribution (Fig. C.4) the Cuxhaven-Sand is a medium sand, moderately sorted and has a symmetrical grain size distribution (Tab. C.1, classification after Friedman and Johnson (1982)).

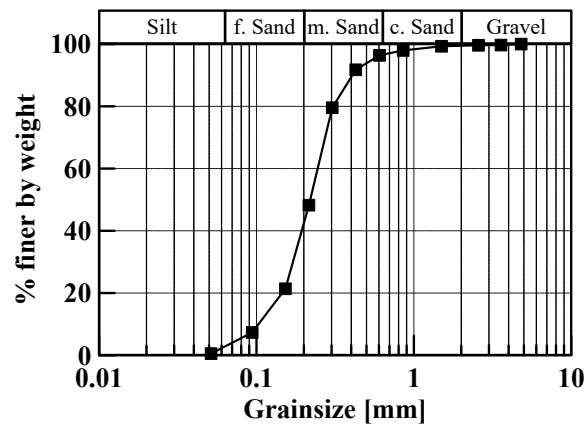


Fig. C.4 Grain size distribution of Cuxhaven-Sand.

### C.3.2 Oedometric compression test

In oedometer tests (Fig. C.5a) a soil sample is placed in a rigid steel ring prohibiting lateral strain ( $\epsilon_2 = \epsilon_3 = 0$ ). By increasing vertical load the specimen is compressed uniaxially under anisotropic stress conditions:  $T_1 = T_2/K_0$ , where  $K_0$  is the earth pressure coefficient. Loose samples were reconstituted by pluviating a sand cone with a funnel into the oedometer until the mold was filled completely following DIN 18126:1996-11 (1996). Afterwards, the tip of the sand cone was removed and the surface flattened using a trowel. In order to reach higher densities, a lateral tapping procedure was performed using a small hammer following Mulilis et al. (1977).

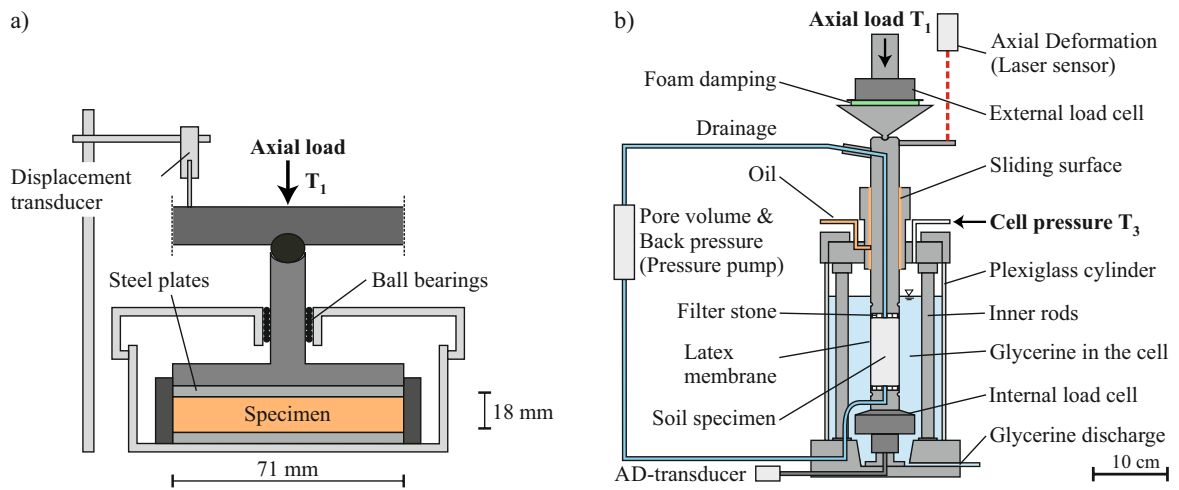


Fig. C.5 Schematic diagrams of: a) oedometer and b) triaxial devices.

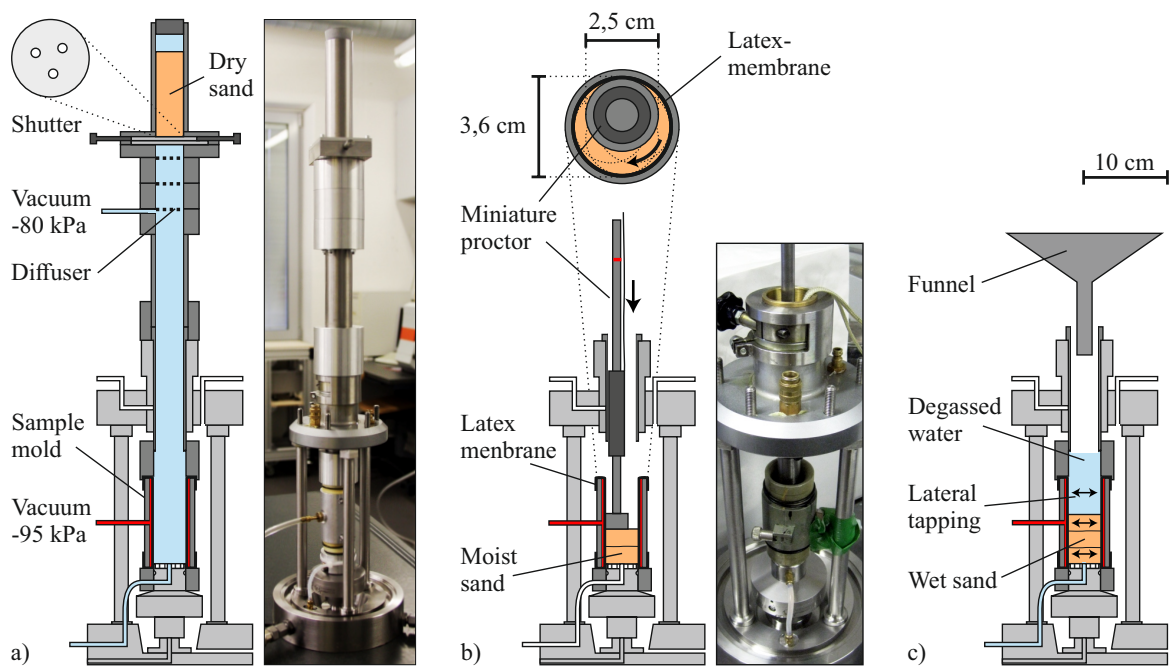


Fig. C.6 Schematic illustration of the applied sample reconstitutions. a) Dry pluviation, b) Moist tamping and c) Lateral tapping.

Table C.2 Comparison between different proctor test procedures.

	Miniature proctor test		Proctor test
	This study	Rondón Rondón et al. (2007)	DIN 18127
Energy [ $kNm/m^3$ ]	698,6	2200	596,8

### C.3.3 Triaxial compression test

The apparatus used for drained triaxial compression tests with displacement rate  $\dot{s} = 0.1 \text{ mm/min}$  ( $D_1 = \text{const.}$ ) is depicted in Fig. C.5b. A piston induces axial stress on the top of a cylindrical sample (Slenderness ratio:  $h/d \approx 2$ , Diameter:  $d = 36 \text{ mm}$ , height:  $h = 90 \text{ mm}$ ) which is measured by an internal load sensor. Volume changes during shearing are recorded by a pressure controller with a syringe pump (Kreiter et al., 2010a,b).

**Dry pluviation** A device was designed based on the work of Lagioia et al. (2006) to pluviate dry 36 mm diameter specimens from a fall height of 45 cm directly into the triaxial apparatus under controlled vacuum of maximal 80 %. The flow rate of sand grains and therefore the density of the sample is regulated by a shutter with different sized openings (Fig. C.6a). In this study pluviated samples were used with vacuum ranging from 60 to 80 %.

**Moist tamping** The moist tamping technique applied is based on the compaction with a proctor hammer (DIN 18127:2012-09, 2012) Specimens were prepared using a miniature proctor hammer (Fig. C.6b) by tamping 4 layers ( $n = 4$ ) into the sample mold. Its fall weight ( $m = 0.2 \text{ kg} \rightarrow W = 2 \text{ N}$ ) was dropped from a height of  $h = 0.2 \text{ m}$  and 40 blows ( $N = 40$ ) were applied to each layer. The energy per total volume of the sample ( $V = 9.2 \cdot 10^{-5} \text{ m}^3$ ) is calculated as  $E = (NnWh)/V$  after Rondón et al. (2007) providing a good comparability to standard proctor tests (Tab. C.2).

**Lateral tapping** A lateral tapping technique was adopted from the standard procedure to obtain the minimal void ratio (DIN 18126:1996-11, 1996). The procedure was slightly modified for triaxial tests (Fig. C.6c), where the sand was pluviated in five layers into the sample mold in degassed water. Each of the five layers were compacted at three radial positions by approx. 40 lateral hits for 20 s on the sample mold, respectively.

## C.4 Hypoplastic constants

The critical friction angle  $\varphi_c$  was obtained from the angle of the sand cones created by air pluviation (height  $h \approx 8 \text{ cm}$ ) using a photo imaging technique similar to Anaraki (2008). From 36 individual measurements a mean value of  $\varphi_c = 32^\circ \pm 1.8^\circ$  was determined.

The limit void ratios at zero stress were calculated from  $e_{d0} \approx e_{min}$ ,  $e_{c0} \approx e_{max}$  and  $e_{i0} \approx 1.15e_{max}$  (Herle and Gudehus, 1999) with  $e_{min} = 0.47 \pm 0.002$  and  $e_{max} = 0.85 \pm 0.02$  being the mean minimum and maximum void ratios from five experiments following DIN 18126:1996-11 (1996).

The granular hardness  $h_s$  and the compression exponent  $n$  were determined from two oedometric compression tests on dry and initially loose ( $e_0 = 0.82$ ,  $I_{D0} = 0.07$ ) samples. To calculate the mean stress  $p = (T_1 + 2T_3)/3$  the lateral stress was estimated as  $T_3 = K_0 T_1$  with  $K_0 = 1 - \sin\varphi_P$ . The peak friction angle  $\varphi_P$  is highly dependent on the void ratio  $e$ .  $\varphi_P$  as a function of  $e$  was estimated by a sequence of triaxial compression tests with constant strain rate on loose, medium and dense Cuxhaven-Sand specimens with different lateral stresses following the procedure by Wichtmann (2005b). Loose and medium-dense samples were reconstituted by sand pluviation similar to the oedometric tests (App. C.3.2). These tests were not further used for comparison of sample reconstitution. High-density samples were reconstituted with moist tamping (App. C.3.3). Fig. C.7a utilizes the density-dependent stress obliquity  $\eta_P = q_P/p_P$  at peak state to calculate  $\varphi_P$  as a function of  $e$  (Fig. C.7b) after Eq. C.2 and C.3:

$$\varphi_P = \sin^{-1} \left( \frac{3\eta_P}{6 + \eta_P} \right) \quad \text{leading to} \quad (\text{C.2})$$

$$\varphi_P(e) = -29.22e + 57.00 \quad (\text{C.3})$$

Note that the point with  $e = 0.85$  is taken from cone pluviation tests. Mean values of  $h_s = 1056 \text{ MPa}$  and  $n = 0.29$  were determined by fitting Eq. C.14 to the curves of  $e(p)$  with highest initial void ratio (uppermost curves in Fig. C.8).

The exponent  $\alpha$  was determined from drained triaxial compression tests with constant strain rate (Fig. C.5b) using initially dense specimens prepared by vacuum pluviation, moist tamping, and lateral tapping (App. C.3.3). The deviator stress and volumetric strain with increasing axial deformation for tests comparing the three preparation methods are depicted in Fig. C.9a. Dry pluviated specimens show consistent behavior, with high peak and critical strength. Moist tamped and laterally tapped samples were reconstituted with same or higher initial densities compared to dry pluviation, although they exhibit lower peak shear strengths. In addition, the deviator stress curves of moist tamped and laterally tapped samples exhibit steeper decreases in post peak shear strength and have lower critical shear strengths. Therefore  $\alpha = 0.19$  was obtained from dry pluviated samples as the mean value of two tests using Eq. C.15 ( $0.51 \leq e_0 \leq 0.57$ ,  $0.72 \leq I_{D0} \leq 0.90$ ), the results are listed in Tab. C.3.

Exponent  $\beta$  was determined from Eq. C.18 by comparing the stiffness increase of two oedometric compression curves  $e(p)$  with different initial void ratios but same mean stress. Stiffness moduli  $E_s$  were taken from initially loose ( $e_0 = 0.82$ ) and dense ( $e_0 = 0.49$ )

specimens (Fig. C.8). From the  $E_s$ -values for different load levels a mean  $\beta = 1.58 \pm 0.20$  was calculated.

The eight hypoplastic constants for the Cuxhaven-Sand are summarized in Tab. C.4.

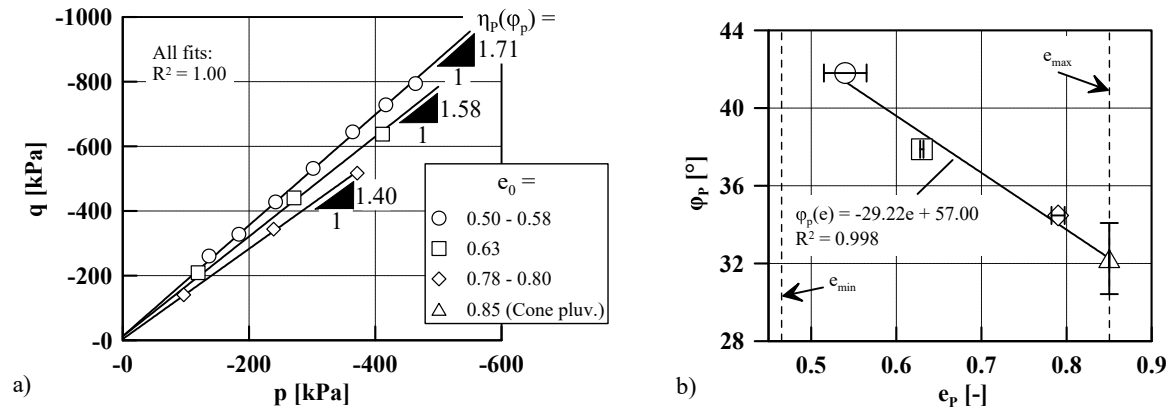


Fig. C.7 a) Peak shear stresses in the  $p - q$ -plane for samples with different initial void ratios. b) Peak friction angle as a function of the void ratio at peak state. The error bars indicate the standard deviation of each individual series of measurements.

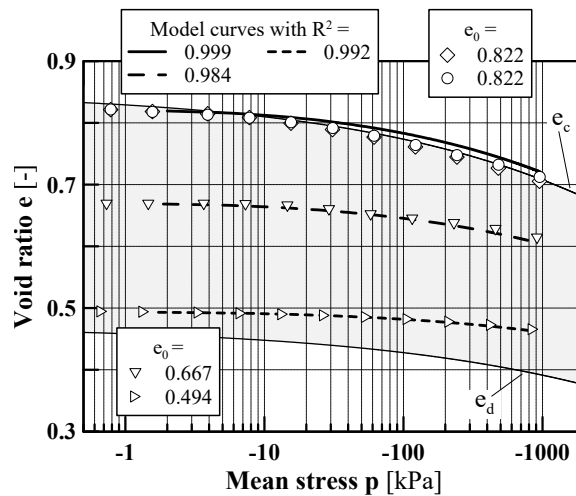


Fig. C.8 Oedometer compression curves with different initial void ratios. Laboratory and simulation results are denoted by symbols and thick lines, respectively. The range between critical and densest void ratios is shaded in gray.

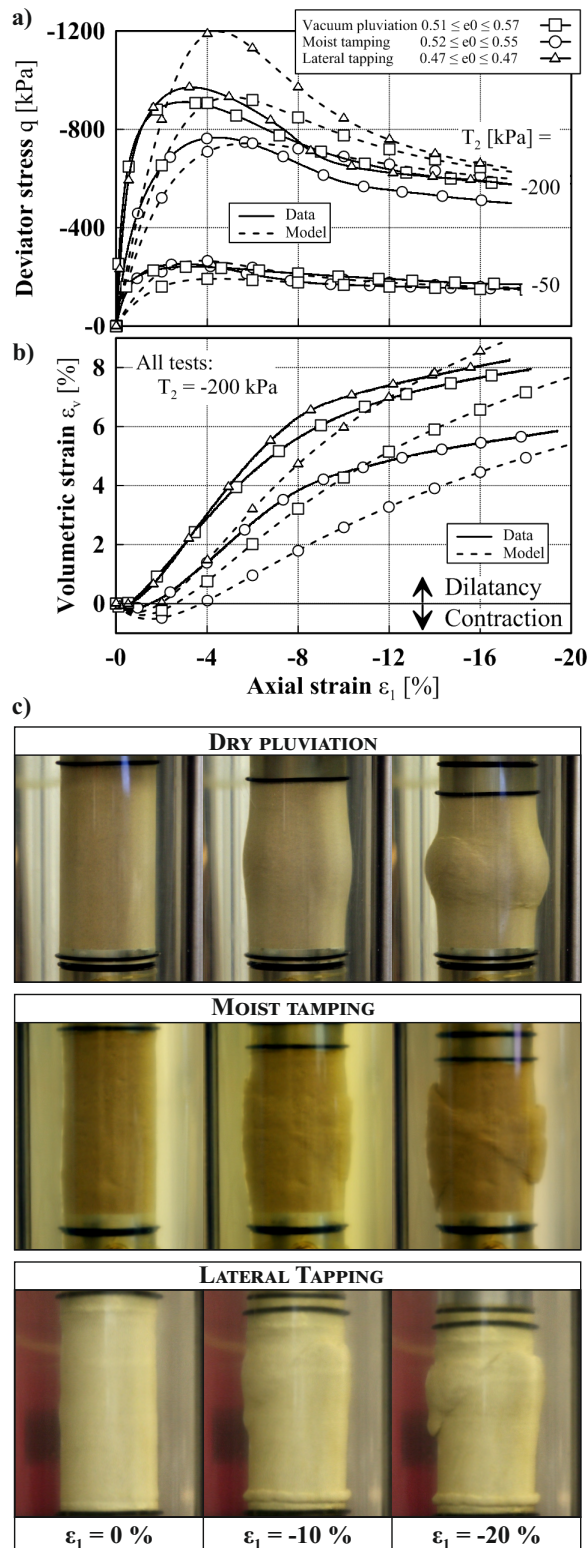


Fig. C.9 Comparison between data and modeled curves in triaxial compression tests for: a) deviator stress and b) volumetric strain. c) Photographs taken during triaxial shearing at 0, -10 and -20 % axial strain.

Table C.3 Comparison of  $\alpha$  regarding different sample preparation methods. *SD* - Standard deviation. In *bold* - picked hypoplastic constant.

Method	Pluviation	Tamping	Lateral tapping
No. of tests	2	2	2
Mean $\alpha$ [-]	<b>0.19</b>	0.24	0.15
SD $\alpha$ [-]	$\pm 0.009$	$\pm 0.077$	$\pm 0.008$

Table C.4 Hypoplastic constants for the Cuxhaven-Sand.

$\varphi_c$ [°]	$h_s$ [MPa]	$n$ [-]	$e_{d0}$ [-]	$e_{c0}$ [-]	$e_{i0}$ [-]	$\alpha$ [-]	$\beta$ [-]
32	1056	0.29	0.47	0.85	0.98	0.19	1.58

## C.5 Results

### C.5.1 Quality of sample reconstitution

Triaxial test samples were reconstituted by dry pluviation under air and vacuum, moist tamping and lateral tapping respectively to archive high initial densities. The repeatability of the void ratio is expressed with the standard deviation *SD* which, despite the generally small number of tests, shows that pluviated and laterally tapped specimens have smallest deviation from mean values (Tab. C.5). Moist tamped samples have four times higher *SD*-values. In Fig. C.10 the initial void ratios  $e_0$  of dry pluviated samples are displayed showing a small decrease of  $e_0$  as a function of applied vacuum. Note that the linear regression was restricted to shutter aperture diameters of 4 mm because smaller shutters resulted in repeated clogging and unsteady particle flow.

The sample deformation during triaxial compression with constant strain rate was documented with photos taken at axial strains of  $\varepsilon_1 = 0\%$ ,  $\varepsilon_1 = 10\%$  and  $\varepsilon_1 = 20\%$ , (Fig. C.9c). Dry pluviated specimens deform homogenously into a bulged shape and do not

Table C.5 Initial void ratios  $e_0$  for different reconstituting techniques. *SD* - Standard deviation.

Method	Pluviation	Tamping	Lateral tapping
Vacuum [%]	0	60-80	
No. of tests	3	4	2
Mean $e_0$ [-]	0.57	0.54	0.47
SD $e_0$ [-]	$\pm 0.005$	$\pm 0.007$	$\pm 0.007$

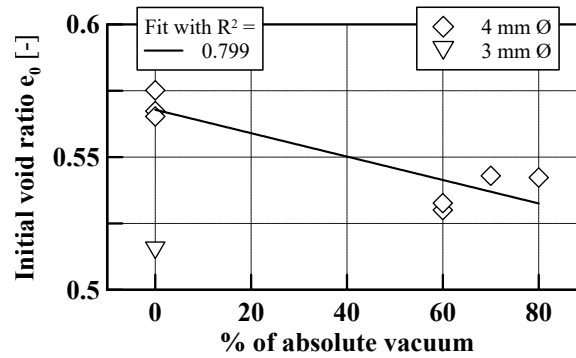


Fig. C.10 Initial void ratios of dry pluviated triaxial samples with shutters containing grid openings of 3 or 4 mm.

Table C.6 Sensitivity of hypoplastic parameter variations on deviatoric stress and volumetric strain. Influence:  $-$  *neglectable*,  $+$  *noticeable*,  $++$  *considerable*.

Material behavior	$n$	$e_{d0}$	$\alpha$
Peak strength $ q_{Peak} $	+	++	+
Peak angle of dilatancy $v_{Peak}$	++	++	+
Initial elasticity modulus $E_i$	++	+	-
Range of contraction $ \varepsilon_c $	++	+	-

develop shear bands. In contrast, moist tamped and lateral laterally tapped samples deform inhomogeneously and develop shear bands after reaching peak shear strength. The effect of sample reconstitution on peak shear strength is visible by comparing moist tamped and dry pluviated Cuxhaven-Sand with initially dense fabric (Fig. C.9a). The difference in peak shear strength between tamped and pluviated triaxial compression curves at consolidation stresses of  $T_2 = -200 \text{ kPa}$  is around 16 %.

## C.5.2 Simulations of element tests

Using the hypoplastic constants obtained for the Cuxhaven-Sand (Tab. C.4) and the equations by von Wolffersdorff (1996), oedometer and triaxial tests are simulated with Matlab and compared with the laboratory data. The only differences between the tests are the state variables initial void ratio at the start of the test  $e_i$  and the actual stress and deformation rate tensors  $\mathbf{T}$  and  $\mathbf{D}$ . For a better comparison the simulated curves were added to Figs. C.8 and C.9.

The hypoplastic model satisfactorily reproduces the oedometric compression curves ( $R^2 > 0.98$ ), which show increase in stiffness with density and mean stress (Fig. C.8).

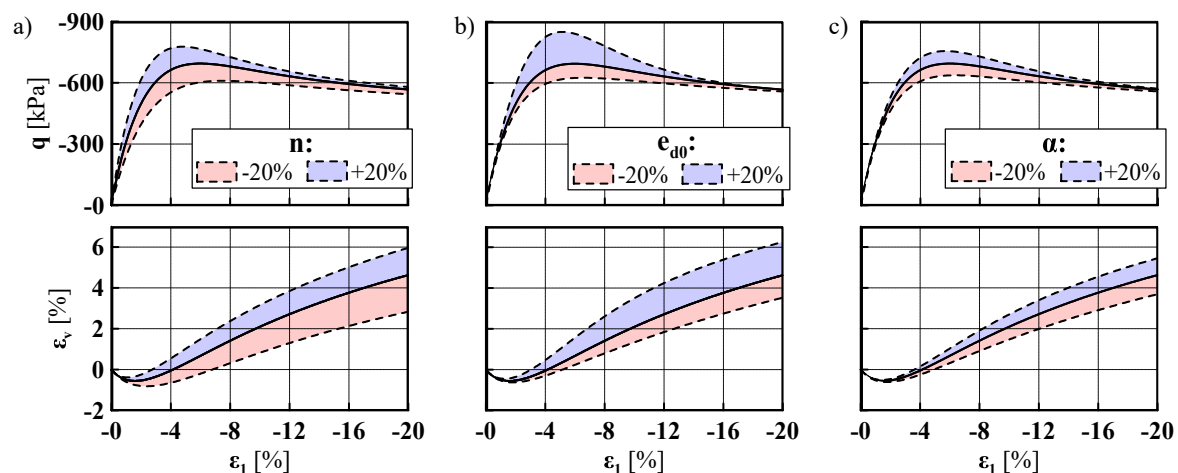


Fig. C.11 Influence of hypoplastic parameter variation on modeled deviatoric stress and volumetric strain of initial dense triaxial tests ( $e_0 = 0.52$ ,  $T_3 = -200 \text{ kPa}$ ). Lines denote simulations with original  $e_0$  and dashed lines indicate a single parameter variation of  $\pm 20\%$ . a) Variation of expression exponent  $n$  b) Variation of limit void ratio  $e_{d0}$  at stress free state c) Variation of exponent  $\alpha$ .

In triaxial element tests the quality of the simulation depends considerably on the applied sample reconstitution. With dry pluviated samples a good match between predicted and measured peak and critical shear strength is obtained (Fig. C.9a). Larger differences are observed where shear bands develop. In tests with moist tamped and laterally tapped samples the critical shear strength is overestimated by the model. In addition, the laterally tapped samples show a much smaller measured peak shear strength in comparison with the simulated curve. At the beginning of deviator stress curves a systematic underestimation of initial tangent modulus  $E_i$  is observed, which shifts the peak state to higher  $\varepsilon_1$ . The simulated volumetric strain curves provide a adequate fit to the experimental data (Fig. C.9b), However the range of contraction  $|\varepsilon_c|$  is overestimated while the peak angle of dilatancy  $v_{Peak}$  is underestimated.

### C.5.3 Sensitivity analysis of triaxial element tests

Simulations of triaxial element tests reveal systematic underestimations of initial tangent modulus  $E_i$  and overestimation of range of contraction  $|\varepsilon_c|$  that are independent of initial void ratio and reconstituting method (Fig. C.9a, b). These errors may have been caused by uncertainty in the determined hypoplastic constants. To estimate the impact of individual hypoplastic parameters on the model result a sensitivity study was carried out, where the value of each parameter was separately varied by  $\pm 20\%$  while the others were kept constant.

Three specific parameters -  $n$ ,  $e_{d0}$  and  $\alpha$  - were found to have the most influence on peak state and small strain development (Fig. C.11).

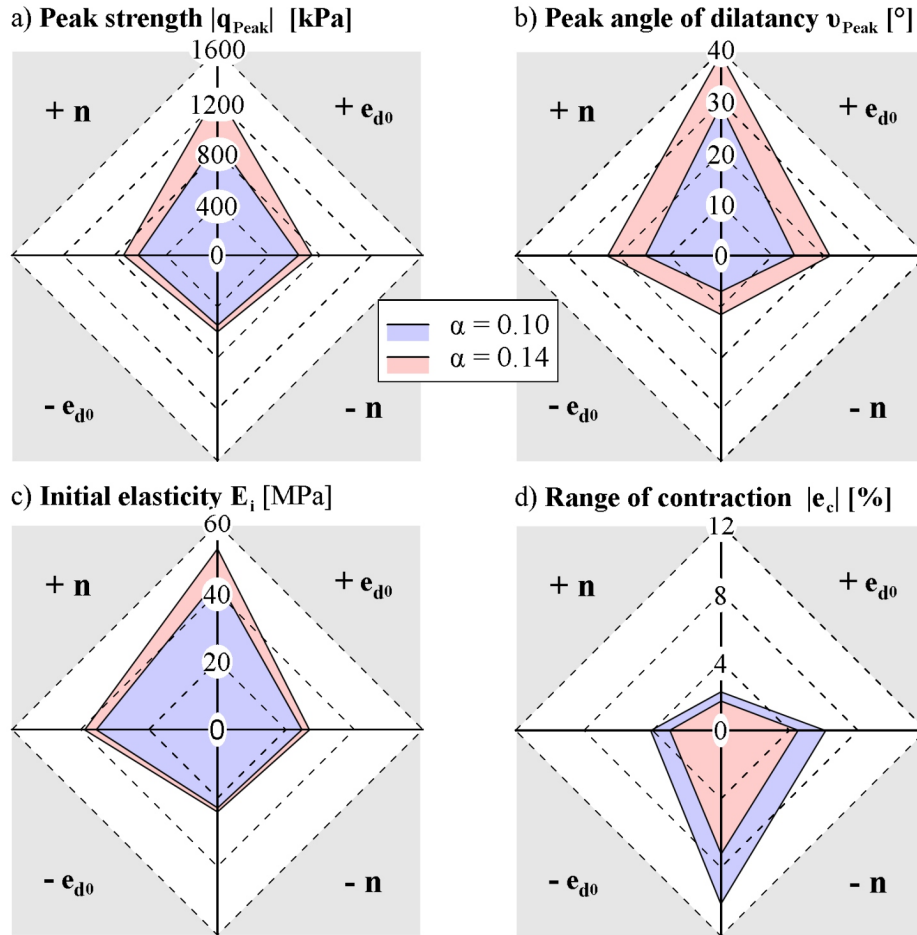


Fig. C.12 Multiparameter analysis of triaxial element tests for deviatoric stress and volumetric strain curves ( $e_0 = 0.52$ ,  $T_3 = -200 \text{ kPa}$ ). The effect of varying  $n$ ,  $e_{d0}$  and  $a$  by 20% on a) initial tangent modulus  $E_i$  b) peak strength  $q_{Peak}$  c) range of contraction  $\varepsilon_c$  c) angle of dilatancy at peak state  $v_{Peak}$ .

By conducting a multiparameter analysis it was further investigated to what extent combinations of these three parameters influence the peak state and small strain development of triaxial element tests. This is illustrated with radar charts in order to display multivariate data in a two-dimensional chart of three variables (Fig. C.12). The dashed “contour” lines indicate the change induced in each measurable quantity ( $q_{Peak}$ ,  $v_{Peak}$ ,  $E_i$  and  $\varepsilon_c$ ) from a 20% change (either positive or negative) in  $n$  or  $e_{d0}$ . Each axis represents a combined effect of two variables; thus moving from one axis to another represents the change in relative contribution of one of the two variables. For example, in Figure C.12a, moving from the top vertical axis to the right horizontal axis tracks a progressive change from the combined effect of a

20 % increase in  $n$  and  $e_{d0}$  to the effect of a 20 % decrease in  $n$  and 20 % increase in  $e_{d0}$  on peak strength. The variation of parameter  $\alpha$  is depicted by the two colored shapes. The multiparameter analysis shows that a 20 % increase in both  $n$  and  $e_{d0}$  has the largest effect on  $q_{Peak}$ ,  $v_{Peak}$ , and  $E_i$ . Larger  $\alpha$  enhances this effect. In contrast,  $\varepsilon_c$  is most strongly affected by a 20 % decrease in both  $n$  and  $e_{d0}$ ; this effect is enhanced by a decrease in  $\alpha$  (Tab. C.6).

## C.6 Discussion

### C.6.1 Influence of sample reconstitution on hypoplastic soil behavior

Reconstitution techniques significantly affect the fabric of granular soils (Vaid et al., 1999; Frost and Park, 2003) and therefore the triaxial stress and strain behavior (Mulilis et al., 1977; Della et al., 2014). This is observed during drained triaxial shearing of the Cuxhaven-Sand with constant strain rate (Fig. C.9). Cuxhaven-Sand specimens prepared by dry pluviation deform homogeneously into bulged shapes after reaching peak shear strength without the formation of shear bands, a consequence of uniform soil fabric. However, internal layering was observed in laterally tapped and moist tamped specimens (Fig. C.9c). These reconstitution methods induce anisotropy into the soil fabric, which leads to anisotropy in mechanical properties (Jang and Frost, 1998; Frost and Park, 2003; Ezaoui and Di Benedetto, 2009). The interfaces between sand layers act as zones of weakness and therefore prone to form sliding surfaces at reduced peak and critical strength (Fig. C.9a). The different sample reconstitutions also influence the form of the stress-strain curves at peak state and therefore the determination of the hypoplastic exponent  $\alpha$ . Because  $\alpha$  is determined from the void ratio and deviator stress at peak state it varies significantly with the used sample reconstitution. For lateral tapping and moist tamping, for instance, the deviation in  $\alpha$  is 60 % (Tab. C.3). Hence, the uncertainty of  $\alpha$  also influences the peak strength in model simulations.

Juneja and Raghunandan (2010) quantitatively investigated the effect of specimen heterogeneity in triaxial compression tests by comparing the peak ( $q_{Peak}$ ) with the critical ( $q_{Crit}$ ) deviator stress for a large relative density range. Therefore the stress reduction ratio  $q_{Red} = q_{Crit}/q_{Peak}$  is introduced as the amount of peak strength loss after failure. In Fig. C.13  $q_{Red}$  ratios from different studies are compared as a function of relative density  $I_D$  and reconstitution technique (Herle and Mayer, 1999; Rondón et al., 2007; Anaraki, 2008; Juneja and Raghunandan, 2010; Kluger, 2013; Kluger et al., 2016a). A common feature in all studies, independent of the applied sample reconstitution, is the general decrease of  $q_{Red}$  with higher  $I_D$ . As expected from critical state soil mechanics, the increasing difference in void ratio

between the initial and the critical state leads to relatively higher peak strength (Muir Wood, 1990). Another factor leading to lower critical shear strength, is the inhomogeneous soil fabric which may contribute to a lower  $q_{Red}$ -ratio. This influence is visible when comparing the  $q_{Red}$ -ratios for different sample reconstitutions (Fig. C.13). Pluviated specimens have the most uniform soil fabrics which is highlighted by the highest  $q_{Red}$ -ratio in the loose to medium relative density range. At high relative densities all sample reconstitutions cluster in a similar  $q_{Red}$ -range, supporting Wood's suggestions, that for high relative densities the reconstitution method does not play an important role in sample uniformity and peak strength (Wood et al., 2008). Because tamped samples exhibit internal layering their  $q_{Red}$ -ratios do not show a significant correlation with initial relative density. Pluviation techniques seem to form the most homogeneous soil fabrics and most reproducible relative density. In contrast, moist tamping and lateral tapping techniques are not recommended for triaxial element tests as they lead to unrealistically low peak and critical strengths.

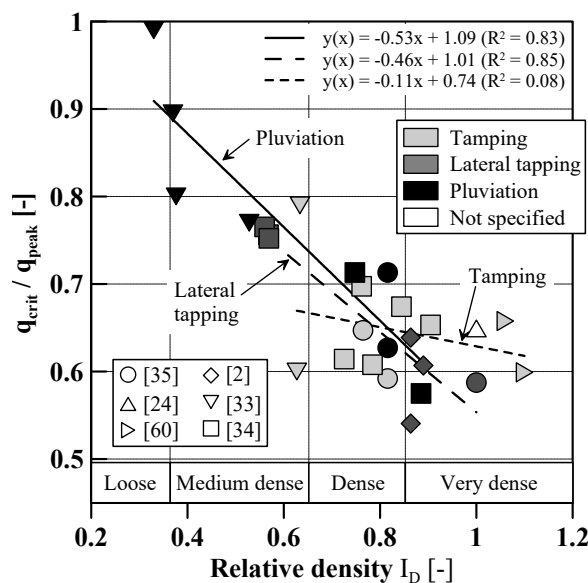


Fig. C.13 Comparison of peak and critical deviator stress ratio for different reconstitution methods and initial relative density. Relative density ranges after DIN EN ISO 14688-2:2004 (2004).

### C.6.2 Hypoplastic model prediction for North Sea sand

The hypoplastic modeling of cone penetration tests which by design induce large strains in the soil fabric requires a sophisticated prediction of peak and critical shear strength (Susila and Hryciw, 2003). Using the hypoplastic parameter set (Tab. C.4) the peak and critical shear strengths of triaxial compression tests on dense pluviated Cuxhaven-Sand are satisfactorily

reproduced. The sensitivity analysis, however, reveals a strong influence of the void ratio at densest possible state  $e_{d0}$  on the simulated peak shear strength (Fig. C.11b). Herle (1997) noted that the modeled peak shear strength is highly sensitive to void ratio for initial void ratios close to  $e_{d0}$ . This implies that small inaccuracies of initial void ratio may lead to large deviations in modeled  $q_{Peak}$ . When reaching peak state the soil sample starts to deform into a bulged shape or develops shear bands that lead to anisotropic stress distribution with lower axial shear strength. Because the requirement of an element test with single stress state is no longer fulfilled the hypoplastic model overestimates  $q_{crit}$ . From multi-parameter analysis (Fig. C.12a) the variations of  $n$ ,  $e_{d0}$  and  $\alpha$  have a cumulative effect on the simulated peak shear strength. The model quality of the Cuxhaven-Sand is compared to the literature (von Wolffersdorff, 1996; Herle, 1997; Herle and Mayer, 1999; Wichtmann, 2005a; Rondón et al., 2007; Anaraki, 2008; Chatra and Dadagoudar, 2010) by using a ratio between hypoplastic model simulations and triaxial test results (Fig. C.14). In all studies the ratio of modeled to measured peak shear strengths  $q_{Peak,Model}/q_{Peak,Test}$  clusters around 1 indicating a good overall prediction of peak shear strength (Fig. C.14a).

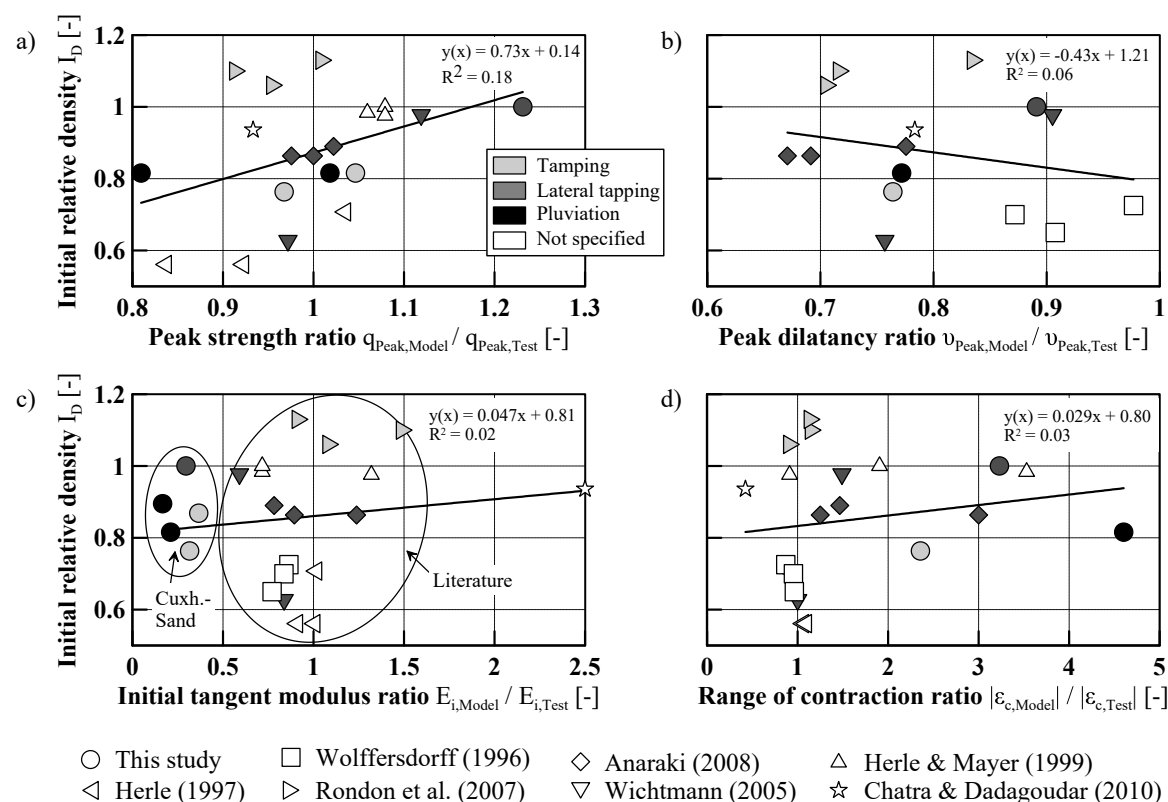


Fig. C.14 Comparison between model simulations and laboratory data for triaxial compression tests in different sands for a) Peak shear strength b) Peak angle of dilatancy c) Initial tangent modulus d) Range of contraction.

During cone penetration, dense sands are subjected to large volumetric changes. Therefore the hypoplastic model should simulate the dilatancy of the Cuxhaven-Sand realistically. Simulated volumetric strain curves reveal a systematic underestimation of peak angle of dilatancy  $v_{Peak}$  (Fig. C.9b) but an improvement of the volumetric strain prediction towards the critical state. The underestimation of peak dilatancy might be caused by inaccurately determined  $n$  or  $e_{d0}$  (Fig. C.11, C.12) but other studies have also reported same systematic underestimation of modeled volumetric strain at peak state (Fig. C.14b, Wichtmann (2005a); Rondón et al. (2007); Anaraki (2008); Chatra and Dadagoudar (2010)). As a consequence, the not reliable volumetric strain predictions at peak state may affect the simulation of cone penetration tests. Whether this is a major problem remains unclear, especially because the volumetric strain at critical state matches well.

Gravity-based foundations mainly induce elevated normal stresses in the subsoil and for the vast majority of the affected soil volume, the shear stress is far below the peak shear strength (Lunne et al., 1983; Das, 2010). Therefore it is important that the settlement and small strain behavior of the Cuxhaven-Sand is simulated well. The stresses in an oedometric compression test are similar to the stresses below a foundation and are simulated well by using the proposed hypoplastic constants (Fig. C.8). Since the soil below a foundation is not fully laterally constrained, the results of the triaxial test have to be considered were the initial tangent modulus  $E_i$  is systematically underestimated (Fig. C.9a). The compression exponent  $n$  significantly influences  $E_i$  in triaxial element tests, as shown in the sensitivity analysis (Fig. C.11a, C.12c) and therefore  $n$  might be responsible for the low initial stiffness in model simulations. However,  $n$  is calculated from the well-matching oedometric tests after Eq. C.14 (Fig. C.8). Since low values of  $E_{i,Model}/E_{i,Test}$  are independent of specimen reconstitution technique and initial relative density (Fig. C.14c), it is possible that differences between oedometric and triaxial sample reconstitution cause the mismatch of simulated  $E_i$ . Other studies found a better match of the initial tangent modulus using a different sediment type (Herle, 1997; von Wolffersdorff, 1996; Anaraki, 2008), and therefore a possible explanation is that the behavior of the Cuxhaven-Sand may not entirely be described by the hypoplastic model by von Wolffersdorff (1996).

Subsoil below gravity-based foundations only undergo small volumetric strain within their contractive range  $|\varepsilon_c|$ , which are systematically overestimated by the hypoplastic model (Fig. C.9b). Similar to the initial tangent modulus,  $|\varepsilon_c|$  is likewise strongly affected by a variation of  $n$  (Fig. C.11a, C.12d). Hence, higher values of  $n$  lead to higher initial tangent modulus and lower range of contraction and therefore may improve the match between the model and test results. The range of contraction ratio  $\varepsilon_{c,Model}/\varepsilon_{c,Test}$  reveals high deviations for the Cuxhaven-Sand compared to the literature (Fig. C.14d), although outliers with a

similar range of contraction ratios have been observed in other studies as well (Herle and Mayer, 1999; Anaraki, 2008).

## C.7 Conclusions

- [1] Hypoplastic constants were determined for the Cuxhaven-Sand to provide a basis for future simulations of cone penetration tests and the assessment of gravity-based foundations.
- [2] Internal layering produced by moist tamping or lateral tapping reduces peak shear strength of dense Cuxhaven-Sand and may lead to inaccuracies in soil characterization, especially in hypoplastic parameter  $\alpha$ .
- [3] Pluviation induces the least heterogeneity into high-density samples and is therefore the most appropriate sample reconstitution for the determination of hypoplastic constants. Moist tamping and tapping are not recommended when considering soil's homogeneity and peak state response.
- [4] From a laboratory perspective the hypoplastic model by von Wolffersdorff (1996) satisfactorily reproduces peak and critical strength in triaxial compression tests and is therefore applicable for simulating cone penetrations in the Cuxhaven-Sand. However, simulation of volumetric changes at peak state underestimates dilatancy.
- [5] The simulation of deformation below gravity-based foundations in the Cuxhaven-Sand is appropriate when considering parameters extracted from oedometric compression tests. Below the edge of the foundation, where lateral strains occur the predictive power of the hypoplastic model concerning the small strain contraction behavior is reduced due to underestimation of initial triaxial tangent modulus and overestimation of the range of contraction.
- [6] The hypoplastic parameter  $n$  seems to be partly responsible for the wide range of modeled initial tangent modulus and range of contraction of triaxial compression tests.

## Acknowledgements

The authors acknowledge funding by the Integrated Coastal Zone and Shelf Sea Research Training Group INTERCOAST and the MARUM Center for Marine Environmental Sciences at the University of Bremen. This research was partly funded by German Federal Ministry

for Economic Affairs and Energy. We thank Marc Huhndorf from the University of Bremen for invaluable technical assistance during laboratory work and construction of laboratory equipment. We are grateful for the assistance of Daniel Otto and Gauvain Wiemer during triaxial laboratory tests. We acknowledge Daniel A. Hepp and Matt J. Ikari for helpful discussions on the paper.

## Hypoplastic model by von Wolffersdorff

In the following section, the mathematical formulation of the hypoplastic constitutive model for granular materials is shortly presented. Therefor the symbol  $\cdot$  denotes a single contraction or matrix product in the shape of  $\mathbf{A} \cdot \mathbf{B} = A_{ik}B_{kj} = C_{ij}$  whereas a colon means a double contraction, eg.  $\mathbf{A} : \mathbf{B} = A_{ij}B_{ij} = C$ . Dyadic multiplication is written as  $\mathbf{A} \mathbf{B} = A_{ij}B_{kl} = C_{ijkl}$ .

The general form of the hypoplastic model is written after Bauer (1996) and Gudehus (1996) as:

$$\dot{\mathbf{T}} = \mathcal{L}(\mathbf{T}, e) : \mathbf{D} + \mathbf{N}(\mathbf{T}, e) \|\mathbf{D}\| \quad (\text{C.4})$$

The objective JAUMANN stress rate  $\dot{\mathbf{T}}$  is a function of the actual CAUCHY stress  $\mathbf{T}$ , the strain rate  $\mathbf{D}$  and the void ratio  $e$ .  $\|\mathbf{D}\| = \sqrt{D_{ij}D_{ij}}$  denotes Euclidian norm. According to von Wolffersdorff (1996)  $\mathcal{L}$  and  $\mathbf{N}$  are fourth-order linear and second-order nonlinear tensor functions, respectively and are calculated from:

$$\mathcal{L} = fbfe \frac{1}{tr(\hat{\mathbf{T}} \cdot \hat{\mathbf{T}})} (F^2 \mathbf{1} + a^2 \hat{\mathbf{T}} \hat{\mathbf{T}}) \quad (\text{C.5})$$

$$\mathbf{N} = fbfe fa \frac{Fa}{tr(\hat{\mathbf{T}} \cdot \hat{\mathbf{T}})} (\hat{\mathbf{T}} + \hat{\mathbf{T}}^*) \quad (\text{C.6})$$

Therein  $\hat{\mathbf{T}} = \mathbf{T}/tr\mathbf{T}$  is the normalized stress tensor,  $\hat{\mathbf{T}}^* = \hat{\mathbf{T}} - \frac{1}{3}\mathbf{1}$  the normalized deviatoric stress tensor and  $\mathbf{1} = 1_{ijkl}$  an identity tensor. The dimensionless factors  $a$  and  $F$  are depending on the critical friction angle  $\varphi_c$  and the actual deviatoric stress level and arise from the MATSUOKA-NAKAI failure criterion (Matsuoka and Nakai, 1974):

$$a = \frac{\sqrt{3}(3 - \sin\varphi_c)}{2\sqrt{2}\sin\varphi_c} \quad (\text{C.7})$$

$$F = \sqrt{\frac{1}{8}\tan^2\psi + \frac{2 - \tan^2\psi}{2 + \sqrt{2}\tan\psi\cos(3\theta)}} - \frac{1}{2\sqrt{2}}\tan\psi \quad (\text{C.8})$$

$$\tan\psi = \sqrt{3}\|\hat{\mathbf{T}}^*\| \quad (\text{C.9})$$

$$\cos(3\theta) = -\sqrt{6} \frac{\text{tr}(\hat{\mathbf{T}}^* \cdot \hat{\mathbf{T}}^* \cdot \hat{\mathbf{T}}^*)}{[\text{tr}(\hat{\mathbf{T}}^* \cdot \hat{\mathbf{T}}^*)]^{3/2}} \quad (\text{C.10})$$

The angles  $\psi$  and  $\theta$  describe the position of  $\mathbf{T}$  in the three-dimensional stress space. The factors  $f_d$ ,  $f_e$  and  $f_b$  in Eq. C.5 and C.6 incorporate the influence of stress and density on the grain skeletons stiffness:

$$f_d = r_e^\alpha = \left( \frac{e - e_d}{e_c - e_d} \right)^\alpha \quad (\text{C.11})$$

$$f_e = \left( \frac{e_c}{e} \right)^\beta \quad (\text{C.12})$$

$$f_b = \frac{h_s}{n} \left( \frac{e_{i0}}{e_{c0}} \right)^\beta \frac{1 + e_i}{e_i} \left( \frac{3p}{h_s} \right)^{1-n} \cdot \left[ 3 + a^2 - a\sqrt{3} \left( \frac{e_{i0} - e_{d0}}{e_{c0} - e_{d0}} \right)^\alpha \right]^{-1} \quad (\text{C.13})$$

The void ratios  $e_d$ ,  $e_c$  and  $e_i$  at densest, critical and loosest possible state decrease with increasing mean stress  $p$  after Bauer (1996) starting with zero stress ( $p = 0$ ):

$$\frac{e_i}{e_{i0}} = \frac{e_c}{e_{c0}} = \frac{e_d}{e_{d0}} = \exp \left[ - \left( \frac{3p}{h_s} \right)^n \right] \quad (\text{C.14})$$

## Determination of the hypoplastic constants

The hypoplastic constitutive equation includes eight material constants  $\varphi_c$ ,  $h_s$ ,  $n$ ,  $e_{d0}$ ,  $e_{c0}$ ,  $e_{i0}$ ,  $\alpha$  and  $\beta$  that are obtained by the following procedure proposed by Herle and Gudehus (1999):

- The critical friction angle  $\varphi_c$  is obtained from cone pluviation tests where it is equivalent to the inclination of the cone (Cornforth, 1973; Rowe, 1969).
- The granular hardness  $h_s$  and the compression exponent  $n$  describe the decrease of the void ratios  $e$ ,  $e_{d0}$ ,  $e_{c0}$  and  $e_{i0}$  with increasing mean stress  $p$  (Eq. C.14). The two parameters are obtained by oedometric compression tests on an initially loose sample ( $e_{c0} \leq e_0 \leq e_{i0}$ ) by fitting Eq. C.14 numerically into the measured curve  $e(p)$ .
- The limit void ratios at the stress free state ( $p = 0$ ) are estimated from  $e_{d0} \approx e_{min}$ ,  $e_{c0} \approx e_{max}$  and  $e_{i0} \approx 1.15e_{max}$ . Thereby the tests for minimum and maximum void ratios are conducted after DIN 18126:1996-11 (1996).
- The exponent  $\alpha$  controls the influence of the initial void ratio on the peak friction angle  $\varphi_p$  and is determined by triaxial compression tests with monotonic strain rate

( $D_1 = 0.1 \text{ mm/min}$ ).  $\alpha$  is calculated afterwards from the stress ratio  $K_P = T_1/T_3$  at the maximum of  $q(\varepsilon_1)$  and with their corresponding void ratios  $e$ ,  $e_d$  and  $e_c$  considering that the stress rate is vanishing at peak state ( $\dot{T}_1 = \dot{T}_2 = \dot{T}_3 = 0$ ):

$$\alpha = \frac{\ln \left[ 6 \frac{(2+K_p)^2 + a^2 K_p (K_p - 1 - \tan v_p)}{a(2+K_p)(5K_p - 2) \sqrt{4 + 2(1 + \tan v_p)^2}} \right]}{\ln(r_e)} \quad (\text{C.15})$$

with  $a$  from Eq. C.7, the stress dependent relative void ratio  $r_e$  (Eq. C.11) and

$$\tan v_p = 2 \frac{K_p - 4 + AK_p(5K_p - 2)}{(5K_p - 2)(1 + 2A)} - 1 \quad (\text{C.16})$$

$$A = \frac{a^2}{(2 + K_p)^2} \left[ 1 - \frac{K_p(4 - K_p)}{5K_p - 2} \right] \quad (\text{C.17})$$

- The exponent  $\beta$  affects an increase of the stress rate  $\dot{\mathbf{T}}$  with increasing density and is obtained from oedometric compression tests ( $D_2 = D_3 = 0$ ) on samples with different initial void ratios. For a specific mean stress  $p$  the corresponding void ratio  $e$  and the constrained modulus  $E_s = \Delta T_1 / \Delta \varepsilon_1$  are determined. By denoting the two different densities with  $\llbracket I$  and  $\llbracket II$ ,  $\beta$  is calculated from:

$$\beta = \frac{\ln \left[ \frac{E_{sII}(m_I - n_I d_{dI})}{E_{sI}(m_I I - n_I I d_{dII})} \right]}{\ln \left( \frac{e_I}{e_{II}} \right)} \quad \text{with} \quad (\text{C.18})$$

$$m = \frac{(1 + 2K_0)^2 + a^2}{1 + 2K_0^2} \quad \text{and} \quad (\text{C.19})$$

$$n = \frac{a(5 - 2K_0)(1 + 2K_0)}{3(1 + 2K_0^2)} \quad (\text{C.20})$$

after Wichtmann (2005b). The lateral earth pressure coefficient  $K_0 = T_3/T_1$  is estimated from the JAKY formula (Jaky, 1948)  $K_0 = 1 - \sin \varphi_p$ .